Climate change is increasing the severity of El Niño-driven fire weather across rapidly degrading peatlands and forests in Indonesia

Authors

Theodore Keeping, *Centre for Environmental Policy, Imperial College, London, UK*
Ben Clarke, *Centre for Environmental Policy, Imperial College, London, UK*
Mariam Zachariah, *Centre for Environmental Policy, Imperial College, London, UK*
Joyce Kimutai, *Centre for Environmental Policy, Imperial College, London, UK*
Arif Rahman, *School of Agriculture, Food and Ecosystem Sciences, The University of Melbourne, Melbourne, Australia; Indonesian Agency for Meteorology, Climatology and Geophysics (BMKG), Jakarta, Indonesia*
Pramudhian Firdaus, *School of Agriculture, Food and Ecosystem Sciences, The University of Melbourne, Melbourne, Australia; Indonesian Agency for Meteorology, Climatology and Geophysics (BMKG), Jakarta, Indonesia*
Guido van der Werf, *Meteorology and Air Quality Group, Wageningen University & Research, Wageningen, the Netherlands*
Izidine Pinto, *Royal Netherlands Meteorological Institute (KNMI), De Bilt, The Netherlands*
Andrew Dowdy, *University of Melbourne, Melbourne, Victoria, Australia*
Luke Harrington, *Te Aka Mātuatua School of Science, The University of Waikato, Hillcrest Road, Hamilton, 3216, New Zealand*
Maja Vahlberg, *Red Cross Red Crescent Climate Centre, The Hague, the Netherlands; Swedish Red Cross, Stockholm, Sweden (based in Ubmeje/Umeå, Sweden)*
Sneha Ganguly, *Red Cross Red Crescent Climate Centre, The Hague, The Netherlands (based in Germany)*
Nicole Lambrou, *California State Polytechnic University, Pomona, USA*
Roop Singh, *Red Cross Red Crescent Climate Centre, The Hague, The Netherlands (based in New Jersey, USA)*
Ramiz Khan, *Red Cross Red Crescent Climate Centre, The Hague, The Netherlands (based in Kolkata, India)*
Amber Agyemang, *Red Cross Red Crescent Climate Centre, The Hague, The Netherlands (based in Amsterdam, the Netherlands)*
Gerbrand Koren, *Copernicus Institute of Sustainable Development, Utrecht University, Utrecht, The Netherlands*
Cornelia Scholz, *Red Cross Red Crescent Climate Centre, The Hague, The Netherlands*
Friederike Otto, *Centre for Environmental Policy, Imperial College, London, UK*

Review authors

Sjoukje Philip, *Royal Netherlands Meteorological Institute (KNMI), De Bilt, The Netherlands*
Luis C. Rodriguez, *International Federation of the Red Cross and Red Crescent Societies (IFRC), Asia Pacific Regional Office (based in Kuala Lumpur, Malaysia)*
Laura D'Arcy, *World Wide Fund for Nature (WWF) UK, Woking, the UK*
Ruth Fuller, *World Wide Fund for Nature (WWF) UK, Woking, the UK*

Cite as Keeping, T. et al. (2026): Climate change is increasing the severity of El Niño-driven fire weather across rapidly degrading peatlands and forests in Indonesia (WWA Scientific Report No. 95). DOI: 10.25560/152615

Main findings

- The fires have burnt 1,9 million hectares of land, but impacts reach far beyond the locations of the fires themselves. Associated smoke affected 12.5 million people across Indonesia, Singapore, Malaysia, and Timor-Leste. and contributed to 400,000 cases of respiratory infections in Indonesia alone. Wildfires can cause severe and often delayed health impacts ranging from difficulty breathing to cardiac arrest. Compounding vulnerabilities (e.g. preexisting conditions, socioeconomics) and concurrent extreme heat events, as occurred this year, can increase the likelihood of negative health outcomes.
- The wildfires have also destroyed orangutan habitats, restricting access to food and forcing critically endangered orangutans into plantations and settlements, increasing human-wildlife conflict. In Java, fires damaged habitats of other threatened species such as the Sunda pangolin and Javan leopard.
- Deforestation, logging and agroforestry expansion have substantially reduced Indonesia's tropical and peat swamp forests, and are associated with fire use for land clearance, while peatland drainage increases fire susceptibility by drying carbon-rich peat. Between 1990 and 2010, peat swamp forest cover declined by approximately 45% in Borneo and 63% in Sumatra, with a further 1.4 million hectares of forest on peatlands lost across Indonesia between 2009 and 2019.
- All three regions analysed show a very similar response to ENSO, and while they are different with respect to vegetation, there are no Peatlands on Java, qualitatively the fire weather conditions are very similar. We therefore combine the three regions in the analysis below.
- Both rainforest and peat land fires are highly drought driven, and to assess these conditions we looked at the July to October rainfall totals that controlled fire season moisture supply. The other component of the seasonal drought is brought by warm, drying conditions. We assessed the main contribution of this through fire season temperatures. In addition, we also assess VPD7x, which characterises short-term hot-dry events that often lead to a fire starting. All three measures are influenced by ENSO and climate change, while the ENSO signal dominates in rainfall and is about the same size as the climate change signal in VPD7x, human-induced climate change is by far the biggest contributor to this year's seasonal temperatures.
- Precipitation in observation datasets showed a very strong relationship with ENSO, with the current El Niño estimated to have decreased the intensity of this year's seasonal rainfall by about 50%. Human caused climate change also shows an emergent decreasing effect on this year's rainfall of about a 15% reduction in rainfall.
- Climate models also represent the strong effect of El Niño, but do not show the climate change response that we see in observations.
- When assessing seasonal temperatures, we find broad agreement between observations and climate models. The assessment shows that climate change has driven a substantial increase in temperatures by several orders of magnitude in likelihood and about 1.6°C in intensity, while ENSO has had a smaller increasing effect, but consistent in observations and models, of about a factor 11 and 0.3°C in intensity. Thus, for temperatures we find a small influence of the current El Niño but a very large increase in the likelihood and intensity of 2026-like conditions attributable to human-induced climate change.
- Fire activity in vegetation responds strongly to short term hot-dry extremes. The 7-day maximum VPD return period estimates suggest that the conditions observed in

August–October 2026 are relatively common under similar ENSO conditions. Observations and climate models broadly agree, but models show overall slightly smaller trends. Combining both models and observations we find that these conditions have become approximately 3 times more likely due to human-induced warming, with VPD intensity increasing by around 0.4 kPa. The ongoing El Niño also increased the likelihood of these conditions by approximately 5 times, with VPD intensity increasing by around 0.6 kPa. These are conservative numbers as they also include models that do not represent the ENSO index well.

- The contribution of El Niño and climate change to increasing the severity of fire weather in Indonesia also means that these conditions are increasingly predictable, creating an opportunity for proactive risk reduction measures. Reducing landscape fire risk involves addressing the conditions that contribute to fire ignition and spread, particularly in drained peatlands and degraded forests. Relevant measures include peatland restoration and preservation and maintaining higher water tables (e.g., blocking canals, reducing drainage, etc.), protecting remaining forest areas, reducing deforestation and incentivising land-management practices that reduce reliance on burning. While these measures would already reduce smoke pollution, additional priorities could include strengthening air quality monitoring and public health warnings as well as measures to limit smoke exposure and protect vulnerable populations, particularly during severe haze episodes.

1 Introduction

From August-October 2026, high fire activity across western Indonesia occurred simultaneously to an unprecedentedly hot fire season, including multiple record-breaking dry heat extremes, and historically low seasonal rainfall. El Niño is very strongly associated with severe fire years over Indonesia, with the three strong El Niño events included in the observational fire record (1997, 2015 and 2026) all having shown anomalously high fire activity (Figure 1.1, GFED5). These fires also occur in the context of considerable land-use change, which strongly shapes the potential for fire. The degradation of pristine peatlands and forests can increase fire activity through drainage of peatlands (Salmayenti et al., 2025) and edge-drying effects in forests (Nikonovas et al., 2020), as well as increased ignition availability in a fragmented landscape (Harrison et al., 2025). Land-use change can also decrease the flammable area, and development means greater access of fire suppression resources into the landscape.

This creates a complex picture: land use change over the past three decades has led to a major shift in Indonesian fire regimes, with land use change altering flammability, landscape connectivity and ignition likelihood. Within this envelope, ignitions and weather (especially seasonal aridity) determine how severe a fire season is within that envelope. Finally, suppression and fire risk management can, to an extent, limit the size of specific fires and reduce impacts.

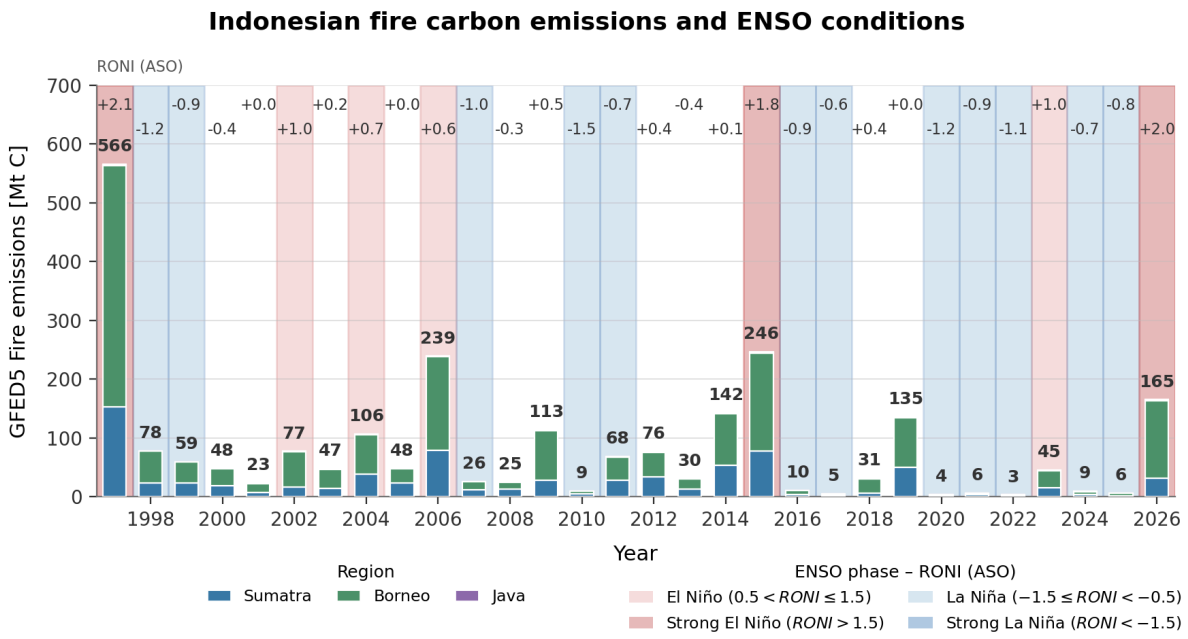


Figure 1.1: *GFED5 (Van der Werf et al., 2025; Chen et al., 2026) fire emissions for the three study regions (megatonnes carbon) overlaid with the August to October Relative Oceanic Niño Index (RONI ASO). Note that absolute and relative estimates of emissions for each year are subject to substantial uncertainty, due to detectability of small and smouldering fires, changes in sensor, and cloud cover. N.B. that 2026 only shows emissions for the January–October period.*

Record Breaking Fire Weather

In this report we use the term "fire weather" to describe weather conditions that are conducive to fire activity, which in the Indonesian case are the drivers of the establishment of seasonal-timescale drought events, and rapid drying events over shorter timescales. Figures 1.2-1.4 below give an overview of the weather conditions experienced over western Indonesia this year.

In southern lowland Borneo (N.B. regions justified in Section 1.2 below), defined below in Figure 1.2 and hereafter referred to as the Borneo region, fire season (August-October) temperatures were 0.2-1.8°C above the previous record value, depending on the observational dataset. In ERA5-Land and MSWX driving seasonal rainfall (July-October) and fire season 7-day Vapour Pressure Deficit (VPD, the evaporative demand from the atmosphere) extremes were also record breaking, but did not break records in the JRA-3Q reanalysis. Fire activity was most intense in Borneo (Figure 1.6), with especially high emissions observed in southern peatland regions.

In southeastern lowland Sumatra, defined in Figure 1.2 and hereafter referred to as the Sumatra region, seasonal temperatures were 0.5-2.2°C above the previous record value. There were record-breaking VPD extremes in ERA5-Land and MSWX, but again these were not seen in JRA-3Q, and no datasets showed a precipitation record.

In Java, fire season temperatures were only found to be record-breaking according to ERA5-Land – though were very high across datasets, and VPD extremes were not record-breaking in this region. Rainfall was very low in the July-September/October period across datasets, ERA5-Land and JRA-3Q

were –5 mm and +19 mm relative to the previous record Jul-Sept rainfall, with MSWX find a 1st July to 27th October period 30 mm wetter than the previous record.

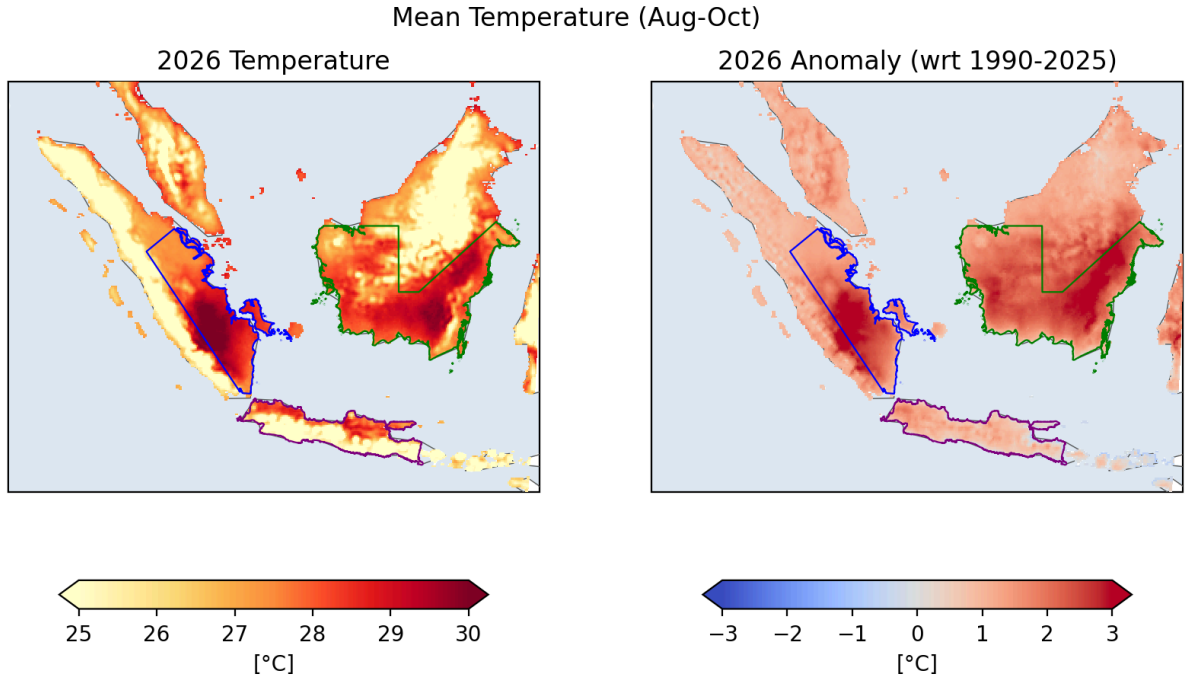


Figure 1.2: *2026 August to October average temperature over western Indonesia, with the Sumatra (blue), Borneo (green) and Java (purple) regions used in this study demarcated. Right panel: the anomaly in that temperature relative to 1990-2025.*

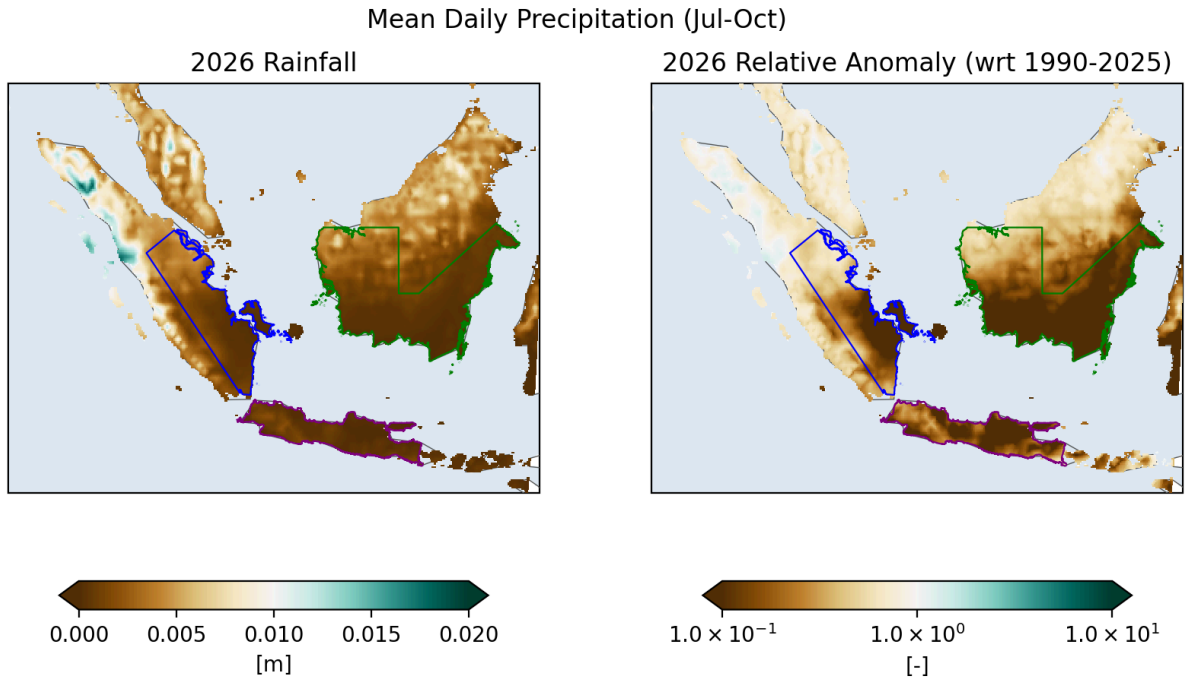


Figure 1.3: *Left panel: 2026 July to October average precipitation over western Indonesia, with the Sumatra (blue), Borneo (green) and Java (purple) regions used in this study demarcated. Right panel: the relative anomaly in that precipitation relative to 1990-2025.*

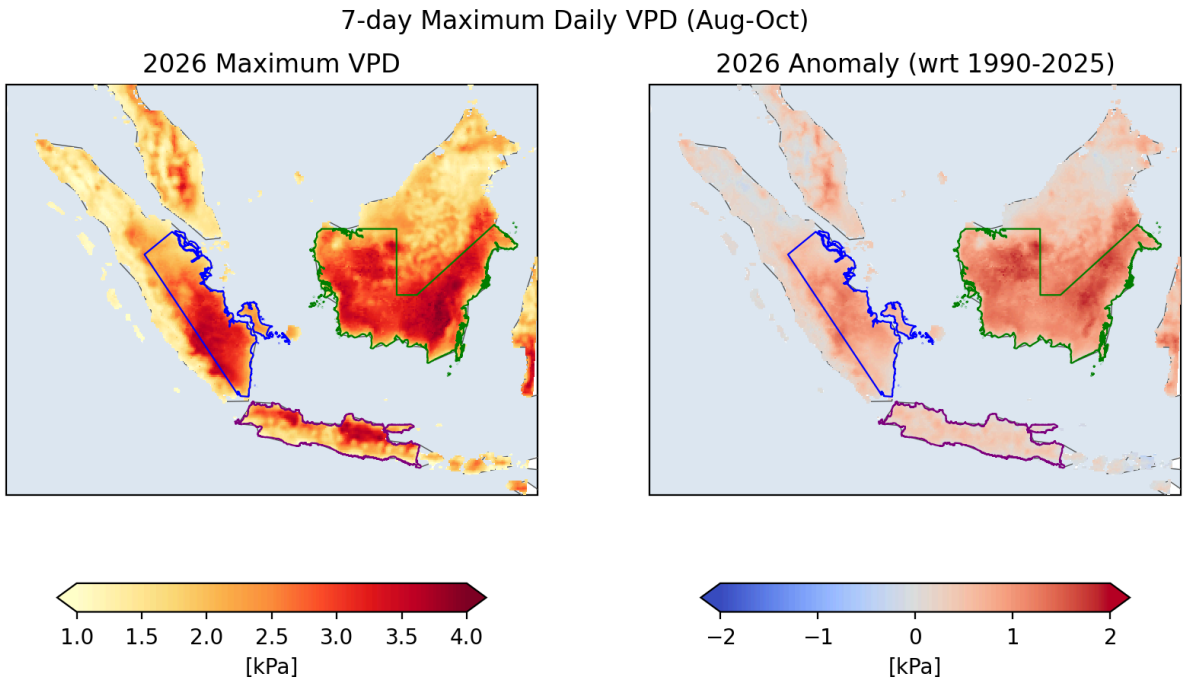


Figure 1.4: *Left panel: the most extreme 7-day period of daily maximum vapour pressure deficit (VPDX7x) in the August-October period in 2026, with the Sumatra (blue), Borneo (green) and Java (purple) regions used in this study demarcated. Right panel: the anomaly in 2026's VPDX7x relative to 1990-2025.*

Meteorology and Driving Synoptic and SST Conditions

Rainfall variability over Indonesia is strongly linked to El Niño Southern Oscillation (ENSO, Nur'Utami and Hayasaka, 2022, Alsepan and Minobe 2020). During El Niño, warmer-than-normal sea-surface water shifts toward the central and eastern equatorial Pacific. Convection, clouds, and rainfall move east with that warm pool, leaving Indonesia under drier, sinking air. El Niño generally reduces rainfall across much of Indonesia, most strongly during the dry season from June to November (Supari et al., 2018; Nur'utami & Hayasaka, 2022) – one of the strongest effects of ENSO globally (Figure 1.5). During this period drought conditions risk increases together with fire and haze risk (Supari et.al, 2018, Hendon, 2003, Sze et.al 2019).

This year, El Niño is very strong, having developed up to +2.0°C to date, according to the RONI index (NOAA, 2026a), and is projected to continue developing to over 2.5°C (NOAA, 2026b - accessed 9th November 2026). A weak, positive Indian Ocean Dipole mode developed late (about +0.4 °C from early September; BoM, 2026). Whilst IOD can have a strong effect on rainfall in this region (Kurniadi et al., 2021; Nur'utami & Hayasaka, 2022), the primary contribution is from the west tropical Indian Ocean, which only displayed weak cooling off Sumatra and Java, so in 2026 its direct contribution to rainfall deficits over Indonesia is uncertain and likely small. Even before the El Niño predictability barrier (Clarke, 2014) was passed, the Indonesian Meteorology Agency (BMKG) March outlook forecast a longer and drier dry season than normal over more than half of Indonesia (BMKG, 2026a). By September, many weather stations in 25 provinces had gone more than 60 days without rain, with BMKG predicted that most regions would not enter the wet season until November–December, later than normal (BMKG, 2026b).

Station observations (Figure A4.2) and radiosonde data (Figure A4.1) showed a meteorological environment that was highly suppressive of convection. Persistent southeasterly flow meant less moisture availability due to greater transport of air from the Australian continent, and a stable mid-troposphere meant less favourable conditions for convective cloud formations. Additionally, frequent early-morning low-level inversions also suppressed vertical mixing, and may have additionally exacerbated the smoke haze after fire events.

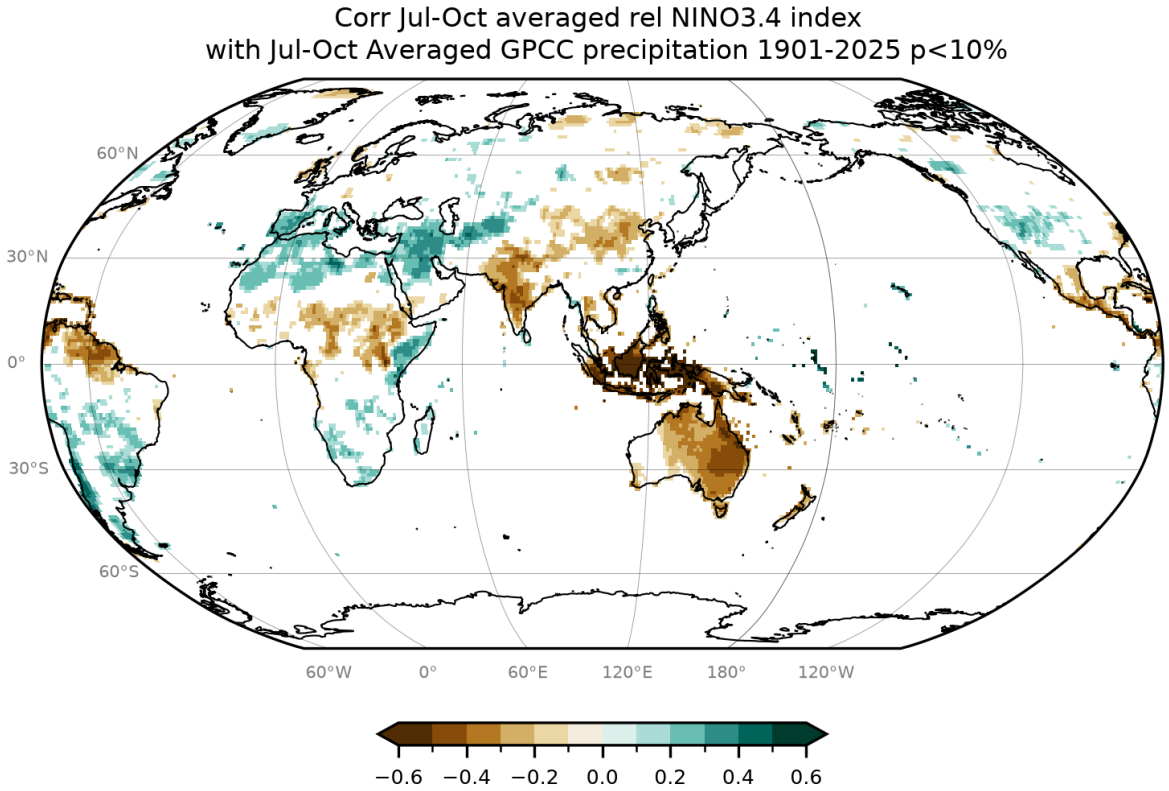


Figure 1.5: *ENSO-rainfall relationships for JASO, using data from GPCC. Green colours indicate that during El Niño there was, on average, more rain than normal, brown colours indicate less rainfall during El Niño. La Niña has the opposite effect in almost all locations. As a measure of the strength of the relationship, we used the correlation coefficient with the Relative Niño3.4 index (RONI).*

Land use change and fire in Indonesia

Fire in Indonesia happens in the context of major land use change that has occurred in recent decades. Fire frequency is much higher in tropical peatland areas compared to rainforest in Indonesia (Vetrita & Cochrane, 2020) – and since 1990 deforestation and the establishment of oil palm and pulpwood plantations has resulted in the draining of most intact peat swamp forest environments (Miettinen et al., 2016). This conversion is often accompanied by drainage – resulting in much more flammable peat and far greater instances of fire (Salmayenti et al., 2025).

Degraded, dryer peat with high flammability is cleared along with secondary forest to establish shrublands and agroforestry as part of the land use change process (Adrianto et al., 2020), and in dry

years – usually associated with El Niño – fires burn a much larger area due to intentional clearance and a drier environment (Field et al., 2016).

1.1 Impacts

The 2026 wildfires have destroyed forest vegetation and wildlife habitats, including those of critically endangered orangutans in Kalimantan, reducing forest availability and driving some orangutans into nearby agricultural areas and communities, where encounters with people become more likely (Antara, 2026). In Java, fires have burned vegetation in Bromo Tengger Semeru National Park, which is home to threatened species such as the Sunda pangolin and Javan leopard (Mongabay, 2026).

The fires have affected already drained and degraded peatlands in Sumatra and Kalimantan, which are important for water storage and regulation, and release carbon stored over thousands of years, further contributing to greenhouse gas emissions (Koarashi et al., 2026). In parts of Kalimantan, prolonged drought and historical peatland degradation has contributed to severe water shortages, with the Kapuas River falling to levels that left water muddy and unsafe for household consumption (AP, 2026). Low river levels have also disrupted fishing and river transport (The Jakarta Post, 2026). While the 2026 fires worsen the situation, these impacts are primarily associated with drought and longer-term land degradation.

In 2015, the most recent strong El Niño year, early estimates of mortality due to haze from the Indonesian fires was estimated to be over 10,000 due to short term mortality (Crippa et al., 2016) and on average the loss in life expectancy due to smoke exposure in Sumatra and Kalimantan is estimated to be about 1 year per inhabitant (Hein et al., 2022). PM2.5 (particulate matter from burning of diameter less than 2.5 µm) is one of the main causes of mortality and health impacts from fire smoke. For reference, the WMO advises a 15 µg/m^3 24-hour mean guideline for air quality, with levels of 288, 1103, and 61 were recorded in Singapore (CNA, 2026), Palembang, Indonesia (Tempo, 2026), and Jakarta (The Straights Times, 2026) respectively. Most severe air quality events over the fire season are mostly fire sourced. The aerosol had a fine mode fraction of about 0.95 (Figure A4.3), matching the smouldering peat smoke observed in 2012–2020 and in 2015 (Eck et al., 2019; Kusumaningtyas et al., 2022).

1.2 Event Definition

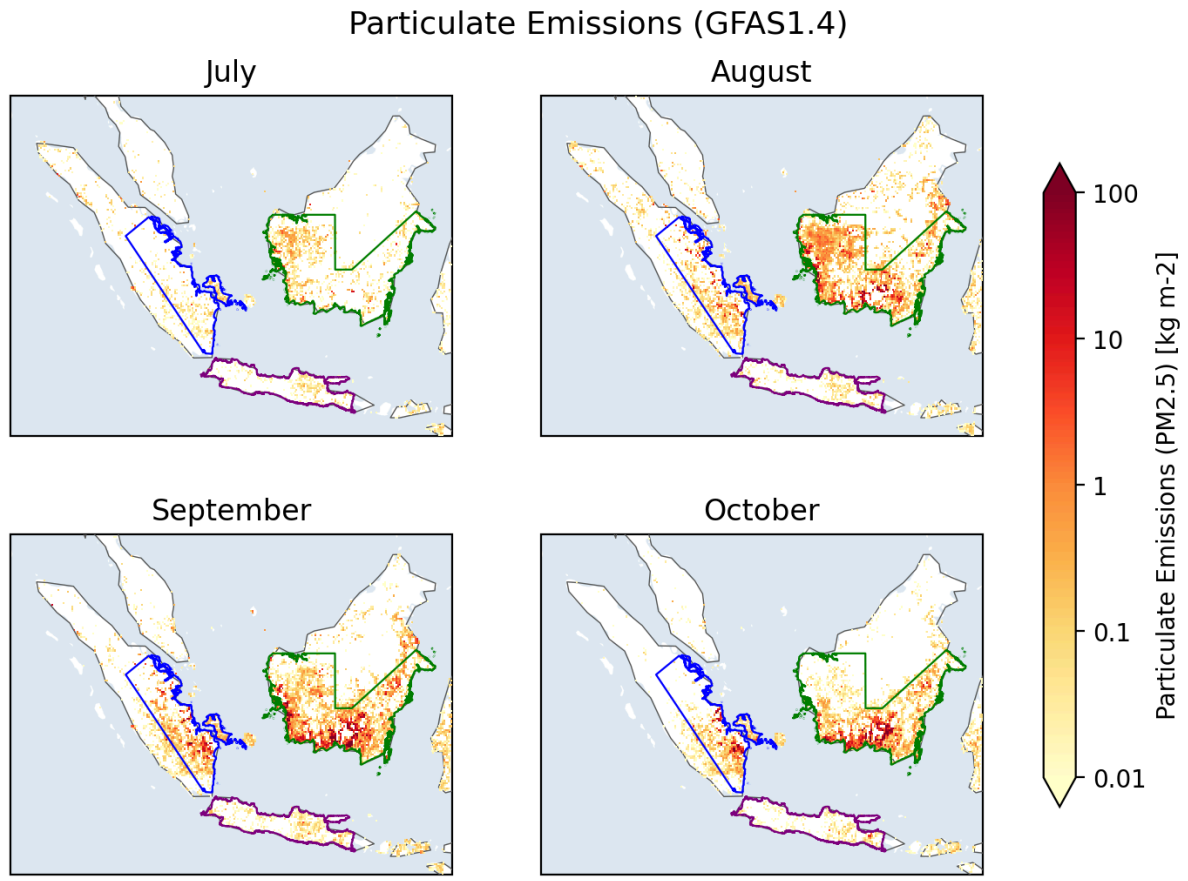


Figure 1.6: *Particulate matter emissions of size < 2.5 µm in diameter according to the GFAS1.4 remote sensing product from ECMWF, with the Sumatra (blue), Borneo (green) and Java (purple) regions used in this study demarcated. Note that these values are illustrative of the seasonal and spatial pattern of fire emissions, but are not reliable as absolute values – being tuned to GFED3.*

To capture the drivers of this fire season, we looked at the highest regions of fire activity, in the southeastern Sumatra lowlands (blue, Figure 1.6) and southern Borneo lowlands (green, Figure 1.6) where fire activity was highest, and avoiding less fire prone mountainous regions. We also assessed Java, which experienced similar weather, less fire activity, and unique ecological impacts. Observed trends in each of these regions were assessed for each variable – and given that weather anomalies and responses to climate change and El Niño were similar across regions these were aggregated into a combined western Indonesia region for the full analysis including climate models. For short, we use refer to this region as "Indonesia" in figures as a shorthand. Given monthly fire activity (Figure 1.6), we assumed an August-October fire season in this analysis.

Fire activity in Indonesia, especially in peatlands, is most meteorologically driven by drought. The primary contributor to this is seasonal precipitation, and to capture this effect we assessed changes in total July-October precipitation (pr-JASO) – allowing for one month of antecedent dry conditions before fire-season onset. Drought severity is also strongly influenced by seasonal temperatures, which mean higher rates of evapotranspiration, and this year was by far the hottest year on record. To assess this we looked at changes in mean temperatures in the August-October fire season (tas-ASO). Finally,

fire activity events are often peaks in vapour pressure deficit (VPD) (Figures A4.4-4.5) which has a strong effect on vegetation dryness, especially for leafy vegetation and finer fuels – which allows for the rapid spread and initial establishment of fires. To assess this component we looked at changes in the highest 7-day period of maximum daily VPD (VPDX7x) in the fire season (ASO).

In this report, we study the influence of anthropogenic climate change by comparing the likelihood and intensity of similar fire weather (with an El Niño as strong as in this year) at present with those in a 1.4°C cooler climate without human-caused warming (based on Forster et al., 2026). We also look at the change in fire weather due to the strength of this year's El Niño, comparing the likelihood and intensity with this year's El Niño compared to a neutral event in today's climate. We also extend this analysis into the future by assessing the influence of a further 1.4°C of global warming from present. This is in line with the latest Emissions Gap Report from the United Nations Environment Programme, which shows that the world is on track for at least 2.8°C temperature rise given currently implemented policies (UNEP, 2025).

To characterise the effect of ENSO we use the Relative Oceanic Niño Index (RONI) – which removes background changes in global ocean temperatures from the index and is superior to methods that don't assess the trend relative to all tropical SSTs (NOAA, 2026). We assessed the model performance of all twelve three-month accumulations of RONI as a covariate in the model, with the ASO (August-October) average concurrent to the fire season giving the greatest improvement in model likelihood – for available data.

2 Observed trends

In this section, we assess the historical trends in each event definition index (section 1.3) associated with both global mean surface temperature (GMST) and the RONI, averaged from August-October (RONI ASO). The latter is used to account for the influence of the El Niño - Southern Oscillation (ENSO), which is known to influence the occurrence rate and intensity of weather in this region at certain times of the year (section 1.1). Including this additional covariate in the statistical model (section A1.3) improved the fit for most regions, variables and datasets, according to the Akaike Information Criterion, than using GMST alone.

The methods used to analyse trends follow the standard WWA protocol using non-stationary extreme value theory, as described in Philip et al. 2020 and expanded upon in Otto et al., 2024. Specifically, the statistical distributions and assumptions for each index are shown in Table 2.1. See Appendix A1 for further details of data and methods.

Extremes index	**Datasets**	**Distribution**	**Nonstationarity assumption**
VPDX7x - 7-day maximum VPD during August-October	ERA5-Land, JRA-3Q, MSWX (hurs)	GEV (in logspace)	Shift
pr-JASO - total precipitation during July-October	ERA5-Land, JRA-3Q, MSWX,	Gaussian	Scale

	CPC		
TAS-ASO - mean temperature during August-October	ERA5-Land, JRA-3Q, MSWX, CPC	Gaussian	Shift

Table 2.1: *Summary of indices, datasets and statistical models used to estimate the influence of different covariates in these metrics.*

2.1 Borneo

2.1.1 VPD

For the 7-day maximum VPD, the return period estimates suggest that the conditions observed in August-October 2026 are now relatively common in the present climate given such ENSO conditions, with such accumulations expected approximately once every 2 years (Table 2.1.1). However, it is worthy of note that there is also a strong relationship between the index and ENSO, suggesting that in neutral conditions, such an event would still be between tens to thousands of times less likely.

The estimates of return period are consistent across the datasets with substantially overlapping 95% confidence intervals (Table 2.1.1), and we note that the observed magnitude is lower in the MSWX dataset due to the use of daily mean near-surface relative humidity (hurs) rather than the daily minimum (hursmin) in calculating the VPD. We further note that the choice of return period affects the estimated probability ratios but that the estimated changes in intensity are independent of the return period. The results for the change in characteristics of such extremes with human-caused climate change and with ENSO conditions in each of the observational datasets are also shown in Table 2.1.1, with both probability ratios for events of equivalent intensity, and changes in intensity of an event of equivalent likelihood.

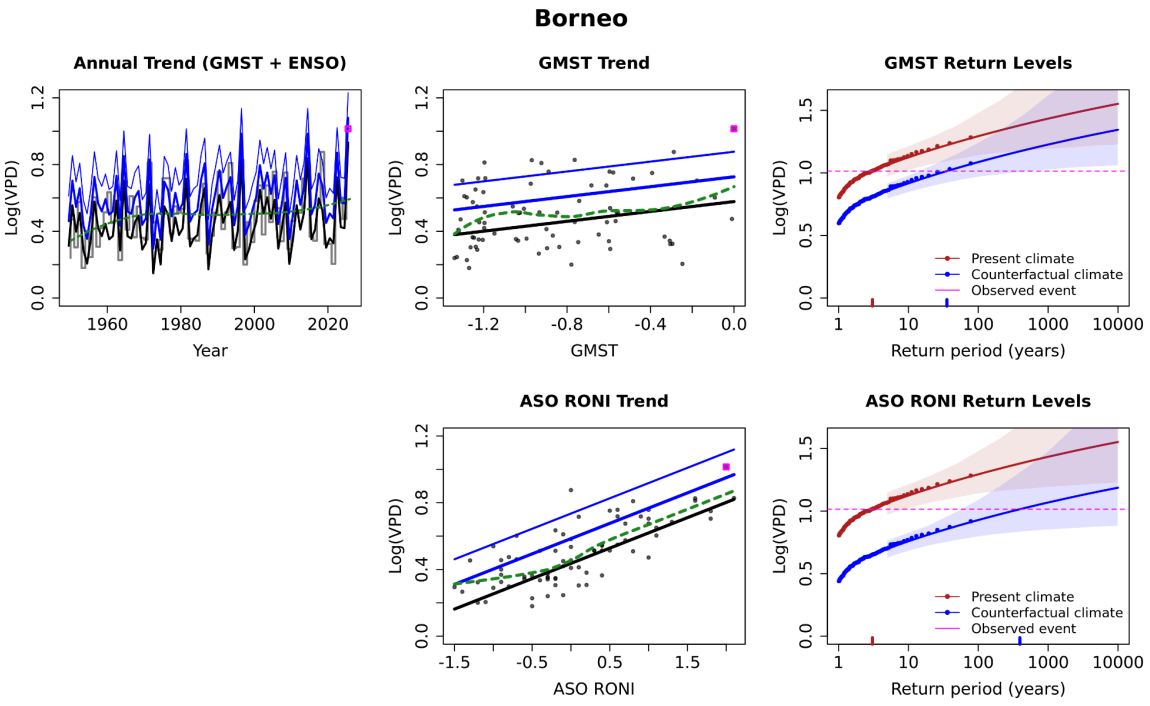


Figure 2.1.1: *Time series (left), fitted trends (middle) and return curves (right) for Log(VPDX7x) in Borneo for both GMST and RONI ASO using ERA5-Land data.* ***Left panel:*** *The loess smoothed trend is shown with the dashed green line, while the expected values and 1-in-6 and 1-in-40 years return period events each year from the fitted statistical model including GMST and August-October RONI as covariates are shown with the black, thick blue and thinner blue lines, respectively.* ***Middle panels:*** *Log(VPDX7x) in the study region against covariates GMST (upper) and RONI ASO (lower). The Loess smoothed trend is shown with the dashed green line, while the expected values and 1-in-6 and 1-in-40 years return period events each year from the fitted statistical model are shown with the black, thick blue and thinner blue lines, respectively.* ***Right panels:*** *Return curves for Log(VPDX7x) in the study region. The event magnitude is shown with the dashed pink line. The red line shows the best fit curve to the data scaled to the present climate and shaded areas show the 95% confidence interval obtained through bootstrapping. Upper: the blue curve shows the data scaled to the preindustrial climate for a model including both GMST and RONI ASO, assuming the ENSO value of 2026. Lower: the blue curve shows the data scaled to a neutral RONI ASO for a model including both GMST and RONI ASO, assuming the GMST value of 2026.*

While the annual time series of VPDX7x shows substantial variability, this is well captured by the statistical model (Figure 2.1.1), and the GEV again provides a good fit to the data. In this region, both higher GMST and RONI ASO are associated with increases in this index, matching the almost monotonically increasing loess smoothed trend in each case. The results suggest that compared to a neutral RONI ASO, the current El Niño resulted in a strong increase in the 7-day maximum VPD during the ASO season: by a factor that varies in magnitude from ~10s to ~1000s in PR and 0.65-0.84 kPa in intensity, with results from all datasets statistically significant at the 95% confidence level. Similarly, compared to a comparable El Niño year in a preindustrial climate, human-induced warming resulted in a strong increase, with different datasets again giving a wide range of estimates: ERA5-Land and JRA-3Q suggest increases by a factor of approximately 9-20 in PR and 0.51-0.57 kPa in intensity, while MSWX suggests that such conditions would have been around 200 times less likely and about 0.8 kPa less intense, comparable to the influence of El Niño. Results from all datasets are again statistically significant at the 95% confidence level.

Dataset	**VPDX7x**		**Change due to 1.4°C global warming (95% C.I.)**		**Change due to RONI ASO (95% C.I.)**	
	Event magnitude (kPa)	**Return period (yr)**	**Probability ratio**	**Change in magnitude (kPa)**	**Probability ratio**	**Change in magnitude (kPa)**
ERA5-Land	2.75	3.06 (1.59, 8.59) 2	**11.6 (4.05, 150)** **9.16 (3.75, 43.0)**	**0.513 (0.286, 0.689)**	**129 (21.1, inf)** **88.3 (22.4, inf)**	**0.840 (0.728, 0.940)**
JRA-3Q	2.92	1.13 (1.01, 1.44) 2	**5.58 (1.98, 18.5)** **19.8 (5.19, inf)**	**0.798 (0.436, 1.07)**	**5.93 (3.34, 178)** **21.7 (7.42, inf)**	**0.813 (0.661, 0.990)**

MSWX (Hurs)	1.90	1.99 (1.08, 8.40) 2	**205 (3.03, inf)** **210 (3.03, inf)**	**0.571 (0.216, 0.861)**	**2390 (18.7, inf)** **2510 (18.6, inf)**	**0.648 (0.533, 0.780)**

Table 2.1.1: *Observed event magnitude and return period of the 2026 VPDX7x in Borneo, as well as the probability ratio and change in magnitude for VPDX7x in Borneo due to both GMST and RONI ASO. Statistically significant trends at the 95% confidence level are highlighted in* ***bold*** *font.*

2.1.2 Precipitation

Four gridded datasets based on stations, satellites and analysis algorithms- CPC, ERA5-Land, JRA-3Q and MSWX, are used for characterising observed seasonal rainfall over the four study regions in this study. A non-stationary Gaussian distribution that scales with GMST and RONI ASO are fitted to July-October rainfall totals (pr-JASO) over the Borneo study region. The model is used to estimate changes in the likelihood (Probability Ratio; PR) and intensity of low-precipitation events between the present-day climate (2026 GMST and ENSO conditions) and two counterfactual scenarios: a climate 1.4°C cooler, representing pre-industrial conditions, and a climate with neutral ENSO conditions. Figure 2.1.2 shows the model fitted to the pr-JASO time series from ERA5-Land. Although the annual time series shows substantial interannual variability, this is well captured by the statistical model, with the Gaussian approximation providing a good fit to the data. In this region, both higher GMST and RONI ASO are associated with decreases in low pr-JASO events, matching the almost monotonically decreasing loess smoothed trend for both covariates.

Table 2.1.2 summarises the results from fitting the statistical models to the four datasets. For seasonal precipitation totals during July-October (pr-JASO) over Borneo, the return period estimates suggest that the anomalously low precipitation during July-October 2026 range from ~5-8600 in the present climate characterised by today's global warming levels and El Niño conditions (Table 2.1.2). This wide range in the return periods is at least in part due to the differences in the resolutions, the underlying algorithms (eg: satellites, stations, reanalysis) and the length of these datasets, in addition to the high year-to-year variability in rainfall over tropical islands, which affects how this year's low precipitation event is as compared to previous drier-than-normal seasons in these datasets. Consequently, it is difficult to reconcile the contribution from GMST increase in the likelihood and magnitude of low precipitation events over this study region. ERA5-Land and JRA-3Q suggest an approximate tripling in the likelihood of low precipitation such as this one, with a ~16% decrease in the seasonal rainfall totals in today's climate as compared a low precipitation event of similar rarity in a 1.4°C cooler climate, all estimates statistically significant at the 95% confidence level. MSWX also show similar drying tendency in low JASO rainfall totals over Borneo in a warming climate- although not statistically significant. CPC on the other hand shows a decreasing trend, suggesting that JASO droughts are becoming milder as compared to a 1.4°C cooler climate, although again with uncertainties encompassing no change, although this may be in part due to the coarser resolution of CPC, which is often a problem for island nations with heterogeneous landscapes (e.g., WWA Philippines Floods, 2024; WWA Southeast Asia storms, 2025). However, despite these differences in the datasets themselves and in the direction of change, all datasets demonstrate a strong relationship between pr-JASO and ENSO, indicating that as compared to neutral ENSO conditions, 2026 El Niño conditions make rainfall deficient seasons such as this one more likely. The best estimated Probability

Ratio (PR) ranges from 30-200, suggesting that low precipitation events such as the 2026 event would have been virtually impossible under neutral ENSO conditions, and around 50% wetter.

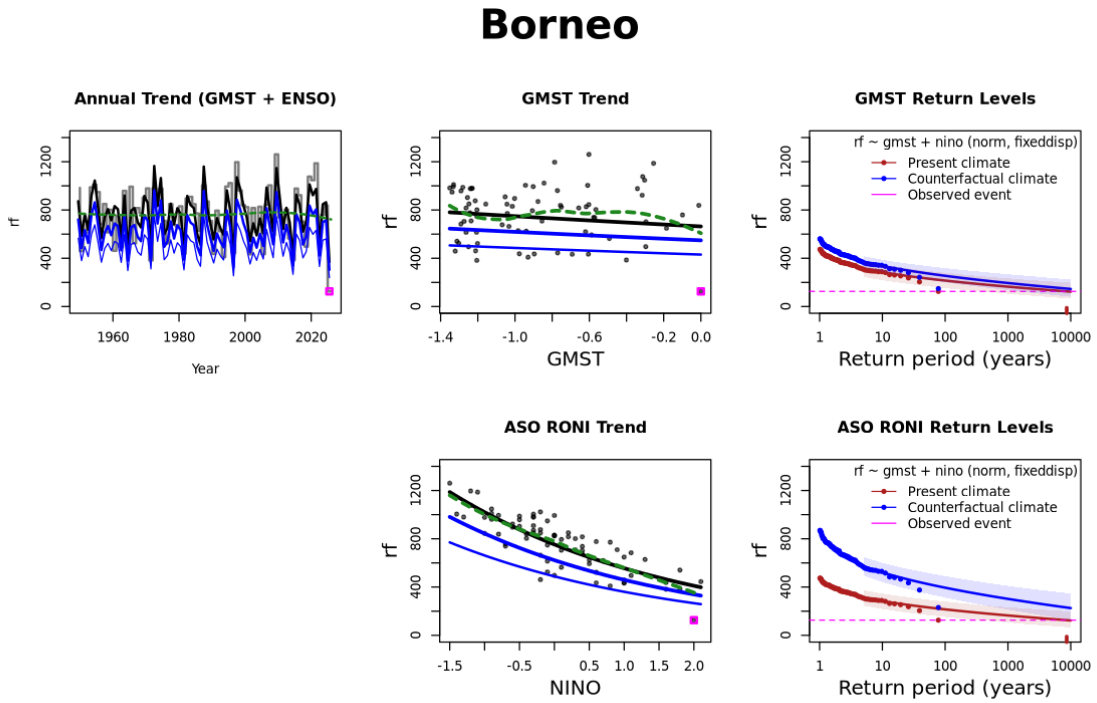


Figure 2.1.2: *Time series (left), fitted trends (middle) and return curves (right) for pr-JASO in Borneo for both GMST and RONI ASO using ERA5-Land data.* ***Left panel:*** *The loess smoothed trend is shown with the dashed green line, while the expected values and 1-in-6 and 1-in-40 years return period events each year from the fitted statistical model including GMST and August-October RONI as covariates are shown with the black, thick blue and thinner blue lines, respectively.* ***Middle panels:*** *pr-JASO in the study region against covariates GMST (upper) and RONI ASO (lower). The Loess smoothed trend is shown with the dashed green line, while the expected values and 1-in-6 and 1-in-40 years return period low precipitation events each year from the fitted statistical model are shown with the black, thick blue and thinner blue lines, respectively.* ***Right panels:*** *Return curves for low extremes of pr-JASO in the study region. The event magnitude is shown with the dashed pink line. The red line shows the best fit curve to the data scaled to the present climate and shaded areas show the 95% confidence interval obtained through bootstrapping. Upper: the blue curve shows the data scaled to the preindustrial climate for a model including both GMST and RONI ASO, assuming the ENSO value of 2026. Lower: the blue curve shows the data scaled to a neutral RONI ASO for a model including both GMST and RONI ASO, assuming the GMST value of 2026.*

Dataset	**pr-JASO**		**Change due to 1.4°C global warming (95% C.I.)**		**Change due to RONI ASO (95% C.I.)**	
	Event magnitude (mm)	**Return period (yr)**	**Probability ratio**	**Change in magnitude (%)**	**Probability ratio**	**Change in magnitude (%)**
CPC	212	14.1 (3.15, 143)	0.487 (0.053, 3.10)	13.5 (-18.1, 54.1)	**85.8 (12.2, 2889)**	**-54.9 (-63.0, -46.0)**
ERA5-Lan	125	8627 (366,	**3.30 (1.21,**	**-15.5 (-28.8,**	**42.2 (17.2,**	**-45.5 (-51.5,**

d		3148515)	**14.5)**	**-2.49)**	**360)**	**-40.2)**
JRA-3Q	261	4.96 (2.36, 15.2)	**2.88 (1.13, 7.99)**	**-18.7 (-31.4, -2.11)**	**34.2 (14.2, 148)**	**-49.1 (-54.9, -42.2)**
MSWX	170	478 (25.6, 164090)	5.20 (0.582, 152)	-16.6 (-37.7, 5.41)	**219 (58.4, 13197)**	**-48.1 (-56.2, -42.1)**

Table 2.1.2: *Observed event magnitude and return period of the 2026 pr-JASO in Borneo, as well as the probability ratio and change in magnitude for pr-JASO in Borneo due to both GMST and RONI ASO. Statistically significant trends at the 95% confidence level are highlighted in* ***bold*** *font.*

2.1.3 Temperature

For Borneo, the return period of estimates of mean August–October seasonal temperatures suggest that the temperatures observed in 2026 range from relatively common to rare in the present climate under the current ENSO conditions. Estimates range from 1 to 167 years across the four datasets (Table 2.1.3). JRA-3Q and CPC indicate relatively common events, with return periods of 1–2 years, while MSWX suggests a return period of nearly 6 years. ERA5-Land, however, indicates a substantially rarer event, with an estimated return period of approximately 167 years.

The observed event magnitude ranges from 27.65°C in JRA-3Q to 29.35°C in MSWX. Table 2.1.3 shows the estimated changes in probability of occurrence and intensity due to human-induced climate change and ENSO. Despite differences in magnitude and return period, results show a strong and consistent influence of anthropogenic warming on seasonal temperatures over Borneo. Compared with a pre-industrial climate, human-induced warming has substantially increased the likelihood of experiencing temperatures as high as those observed in 2026. All four datasets indicate infinite best-estimate probability ratios, indicating that temperatures of this magnitude would have been extremely unlikely in the absence of anthropogenic warming. The corresponding increases in temperature intensity range from approximately 1.54°C in ERA5-Land to 2.07°C in JRA-3Q, with all four datasets showing statistically significant increases at the 95% confidence level.

ENSO also shows a strong and consistent influence on seasonal temperatures over Borneo. Compared with neutral ENSO conditions, the prevailing ENSO conditions increased the likelihood of the observed temperatures by a factor of 2 in CPC, 15 in JRA-3Q, 782 in MSWX and more than 3 million in ERA5-Land. The corresponding increases in temperature intensity range from approximately 0.17°C in CPC to 0.84°C in ERA5-Land. All four datasets indicate statistically significant increases in both likelihood and temperature intensity. Overall, the results suggest that human-induced warming has substantially increased seasonal temperatures over Borneo, while the prevailing ENSO conditions further amplified the likelihood and intensity of the 2026 ASO heat.

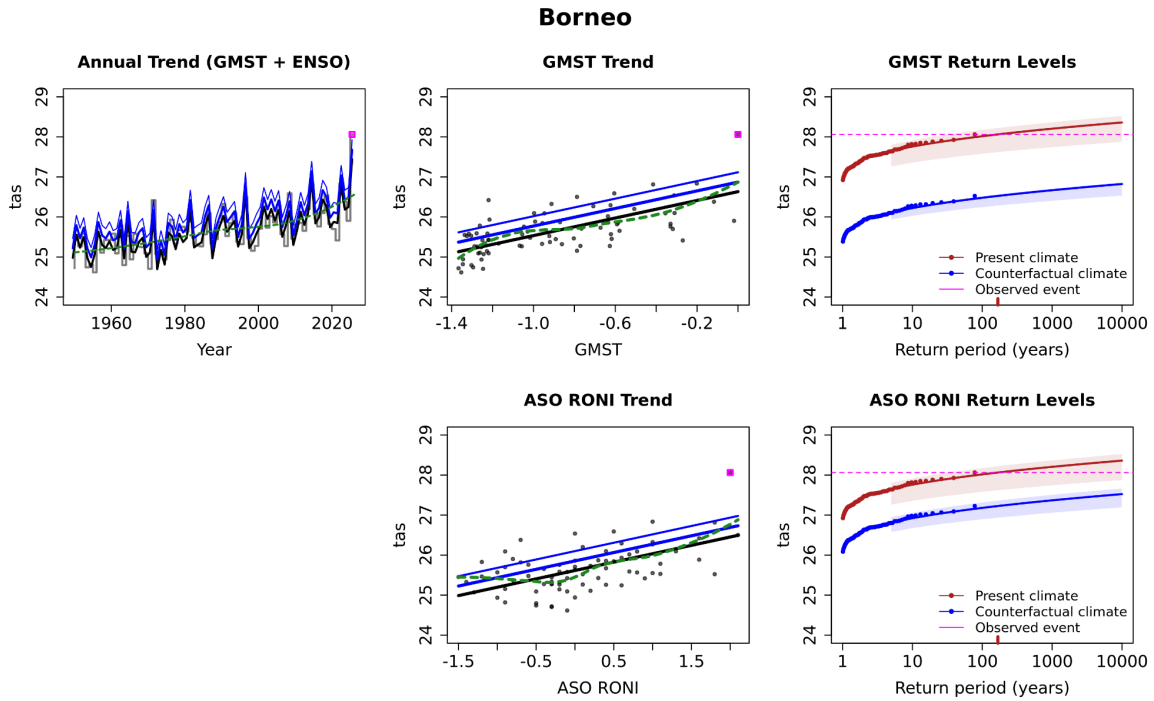


Figure 2.1.3: *Time series (left), fitted trends (middle) and return curves (right) for tas-ASO in Borneo for both GMST and RONI ASO using ERA5-Land data.* ***Left panel:*** *The loess smoothed trend is shown with the dashed green line, while the expected values and 1-in-6 and 1-in-40 years return period events each year from the fitted statistical model including GMST and August-October RONI as covariates are shown with the black, thick blue and thinner blue lines, respectively.* ***Middle panels:*** *tas-ASO in the study region against covariates GMST (upper) and RONI ASO (lower). The Loess smoothed trend is shown with the dashed green line, while the expected values and 1-in-6 and 1-in-40 years return period ASO temperature events each year from the fitted statistical model are shown with the black, thick blue and thinner blue lines, respectively.* ***Right panels:*** *Return curves for low extremes of tas-ASO in the study region. The event magnitude is shown with the dashed pink line. The red line shows the best fit curve to the data scaled to the present climate and shaded areas show the 95% confidence interval obtained through bootstrapping. Upper: the blue curve shows the data scaled to the preindustrial climate for a model including both GMST and RONI ASO, assuming the ENSO value of 2026. Lower: the blue curve shows the data scaled to a neutral RONI ASO for a model including both GMST and RONI ASO, assuming the GMST value of 2026.*

Dataset	**ASO tas**		**Change due to 1.4°C global warming (95% C.I.)**		**Change due to RONI ASO (95% C.I.)**	
	Event magnitude	**Return period (yr)**	**Probability ratio**	**Change in magnitude**	**Probability ratio**	**Change in magnitude**
ERA5-Land	28.06	167.47 (15.60,51227.24)	inf	**1.54 (1.25,1.78)**	**3313176.77 (170327.56,inf)**	0.84 (0.68,0.99)
JRA-3Q	27.65	1.28 (1.05,1.74)	inf	**2.07 (1.90,2.27)**	**15.27 (5.68,68.10)**	0.52 (0.43,0.62)
MSWX	29.35	5.72	inf	**1.73**	**781.61**	0.55

		(2.05,114.31)		**(1.38,2.08)**	**(122.94,642 20.46)**	(0.41,0.68)
CPC	28.33	1.85 (1.13,5.11)	inf	**2.00 (1.66,2.41)**	**2.09 (1.12,4.97)**	0.17 (0.03, 0.32)

Table 2.1.3: *Observed event magnitude and return period of the 2026 mean August-October seasonal temperature (ASO tas) in Borneo , as well as the probability ratio and change in magnitude for ASO tas in Borneo due to both GMST and RONI ASO. Statistically significant trends at the 95% confidence level are highlighted in* ***bold*** *font.*

2.2 Sumatra

2.2.1 VPD

For the 7-day maximum VPD, the return period estimates suggest that the conditions observed in August-October 2026 are now relatively common in the present climate given such ENSO conditions, with such accumulations expected approximately twice every 3 years (Table 2.2.1). However, it is worthy of note that there is also a strong relationship between the index and ENSO, suggesting that in neutral conditions, such an event would still be between 6-11 times less likely, or a ~9-16 year event.

The estimates of return period are consistent across the datasets with substantially overlapping 95% confidence intervals (Table 2.2.1), and we note that the observed magnitude is lower in the MSWX dataset due to the use of daily mean near-surface relative humidity (hurs) rather than the daily minimum (hursmin) in calculating the VPD. The results for the change in characteristics of such extremes with human-caused climate change and with ENSO conditions in each of the observational datasets are also shown in Table 2.2.1, with both probability ratios for events of equivalent intensity, and changes in intensity of an event of equivalent likelihood.

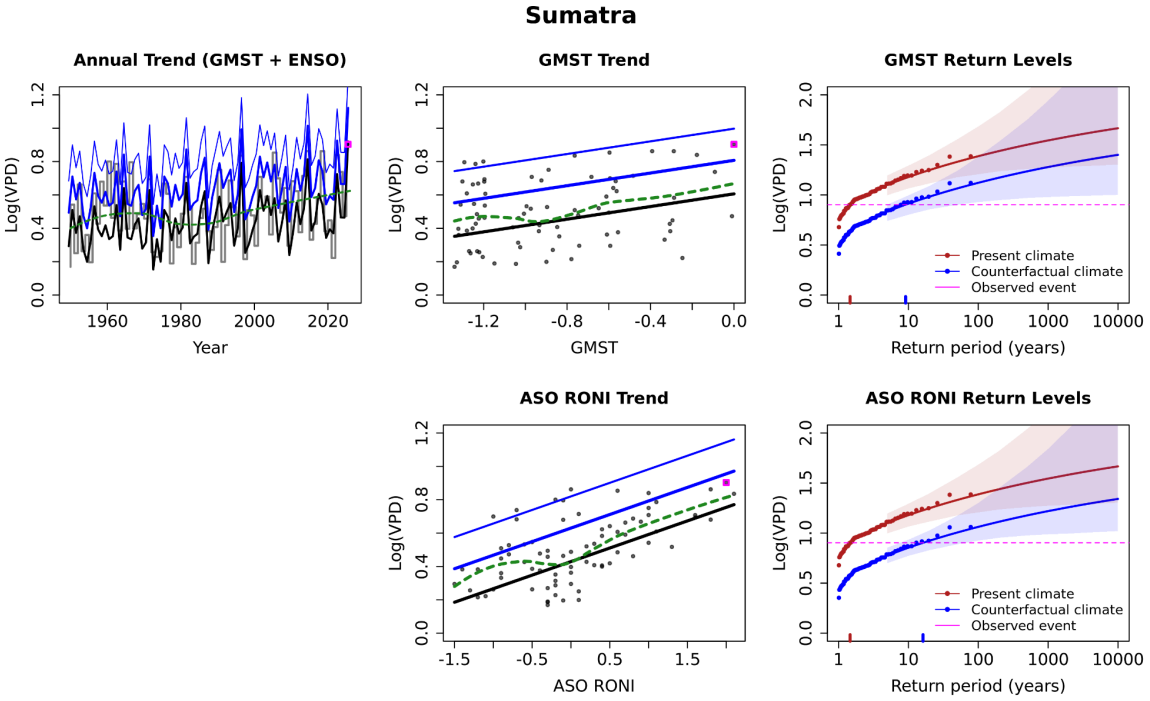


Figure 2.2.1: *Time series (left), fitted trends (middle) and return curves (right) for Log(VPDX7x) in Sumatra for both GMST and RONI ASO using ERA5-Land data (all panels as in Figure 2.1.1 but for VPDX7x in Sumatra).*

While the annual time series of VPDX7x shows substantial variability, this is well captured by the statistical model (Fig. 2.2.1). Both higher GMST and RONI ASO are associated with increases in this index, matching the almost monotonically increasing loess smoothed trend in each case. Further, the return curves of the fitted GEV provide a good fit to the data. The results suggest that compared to a neutral RONI ASO, the current El Niño resulted in a strong increase in the 7-day maximum VPD during the ASO season: by a factor of approximately 6-11 in PR and 0.41-0.69 kPa in intensity, with results from all datasets statistically significant at the 95% confidence level. Similarly, compared to a comparable El Niño year in a preindustrial climate, human-induced warming resulted in a strong increase: ERA5-Land and JRA-3Q suggest increases by a factor of approximately 6-10 in PR and 0.50-0.58 kPa in intensity, while MSWX suggests that such conditions would have been virtually impossible without this warming and about 0.83 kPa less intense. Results from all datasets are again statistically significant at the 95% confidence level.

Dataset	**VPDX7x**		**Change due to 1.4°C global warming (95% C.I.)**		**Change due to RONI ASO (95% C.I.)**	
	Event magnitude (kPa)	**Return period (yr)**	**Probability ratio**	**Change in magnitude (kPa)**	**Probability ratio**	**Change in magnitude (kPa)**
ERA5-Land	2.47	1.47 (1.07, 2.44) 1.5	**6.22 (2.91, 29.1)** **6.41 (2.96, 32.2)**	**0.576 (0.342, 0.785)**	**11.1 (5.84, 33.5)** **11.4 (6.10, 36.6)**	**0.685 (0.540, 0.817)**
JRA-3Q	2.49	1.15 (1.01, 1.50) 1.5	**7.03 (3.07, 17.0)** **10.2 (4.20, 33.6)**	**0.495 (0.318, 0.628)**	**4.30 (2.87, 7.78)** **6.04 (3.70, 13.3)**	**0.410 (0.321, 0.505)**
MSWX (Hurs)	1.77	1.29 (1.01, 2.22) 1.5	**inf (45.2, inf)** **inf (53.7, inf)**	**0.829 (0.604, 1.02)**	**4.86 (1.81, 123)** **7.18 (2.35, inf)**	**0.417 (0.226, 0.563)**

Table 2.2.1: *Observed event magnitude and return period of the 2026 VPDX7x in Sumatra, as well as the probability ratio and change in magnitude for VPDX7x in Sumatra due to both GMST and RONI ASO. Statistically significant trends at the 95% confidence level are highlighted in* ***bold*** *font.*

2.2.2 Precipitation

Figure 2.2.2 shows the non-stationary Gaussian model that scales with GMST and RONI ASO fitted to the pr-JASO time series from ERA5-Land for the Sumatra study region. Table 2.2.2 summarises the results from fitting the statistical models to all four datasets (CPC, ERA5-Land, JRA-3Q and

MSWX). The return period estimates suggest that the anomalously low precipitation during July-October 2026 range from 1 (in CPC) to 30 years (in ERA5-Land) in the present climate characterised by today's global warming levels and El Niño conditions (Table 2.2.2). This wide range in the return periods is at least in part due to the differences in the resolutions, the underlying algorithms (eg: satellites, stations, reanalysis) and the length of these datasets, in addition to the high year-to-year variability in rainfall over tropical islands, which affects how this year's low precipitation event is as compared to previous drier-than-normal seasons in these datasets. For example, the 2026 event magnitude is much higher in CPC (~600mm), as compared to the other three datasets that registered rainfall totals of ~180-340mm for this event. CPC also seemingly suggests that the rainfall deficient JASO seasons are becoming less likely, or wetter (but only by ~3% and with large uncertainty), while ERA5-Land and JRA-3Q suggest ~7-13% drying although again, with uncertainty ranges encompassing no change. MSWX is the exception here, with the 1.4°C warming seemingly making low precipitation events such as this one about 50 times more likely and 43% drier, but this is one dataset, and without further validation with ground-based data, this remains a standalone result. However, despite these differences all datasets demonstrate a strong relationship between pr-JASO and ENSO, indicating that as compared to neutral ENSO conditions, 2026 El Niño conditions make rainfall deficient seasons such as this one more likely. Once again, due to the wide range in the Probability Ratio estimates between the datasets, it is difficult to quantify the expected return period of such events had it been neutral ENSO conditions. As explained in Section 2.1.1, while the choice of return period affects the estimated probability ratios, the estimated changes in intensity are independent of the return period. All datasets suggest a solid ~35-45% decrease in pr-JASO due to the 2026 El Niño, as compared to neutral conditions, with results from all datasets statistically significant at the 95% confidence level.

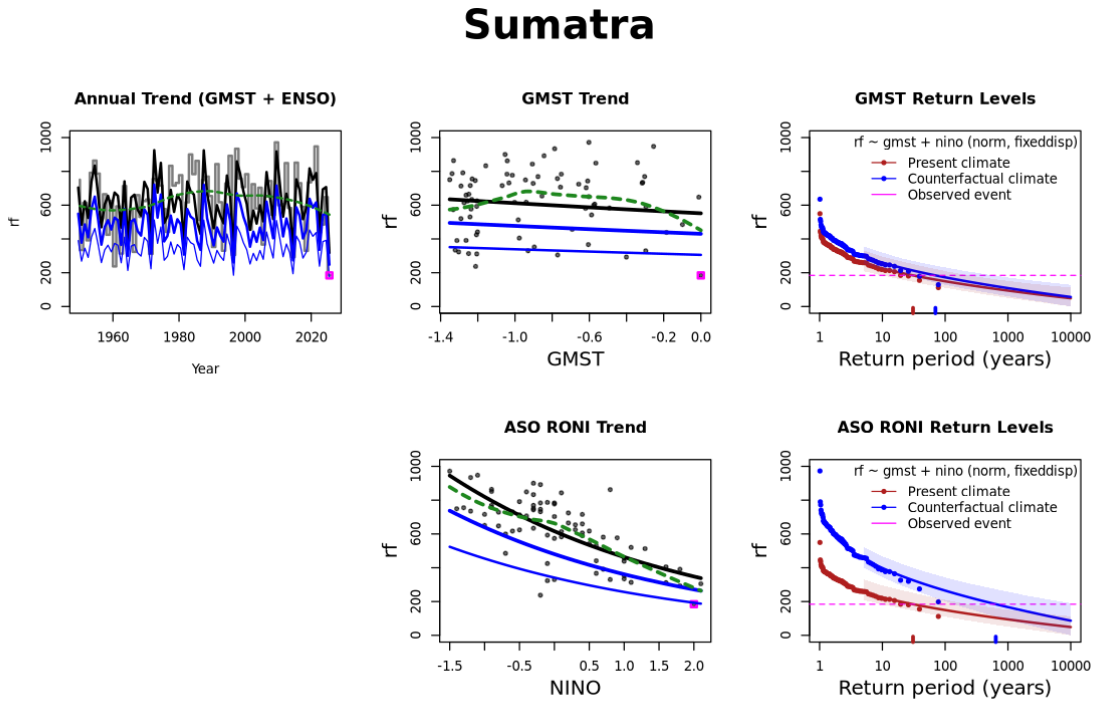


Figure 2.2.2: *Time series (left), fitted trends (middle) and return curves (right) for low precipitation events based on pr-JASO in Sumatra for both GMST and RONI ASO using ERA5-Land data (all panels as in Figure 2.1.2 but for pr-JASO in Sumatra).*

Dataset	pr-JASO		Change due to 1.4°C global warming (95% C.I.)		Change due to RONI ASO (95% C.I.)	
	Event magnitude (mm)	Return period (yr)	Probability ratio	Change in magnitude (%)	Probability ratio	Change in magnitude (%)
CPC	601	1.02 (1.00, 1.18)	0.994 (0.887, 1.07)	3.48 (-36.3, 47.9)	**1.70 (1.08, 2.50)**	**-35.5 (-56.2, -21.5)**
ERA5-Land	184	30.8 (9.39, 257)	2.27 (0.775, 7.80)	-13.5 (-27.3, 4.99)	**20.8 (6.12, 134)**	**-43.5 (-50.5, -33.8)**
JRA-3Q	345	3.64 (1.92, 10.4)	1.38 (0.671, 2.90)	-7.25 (-21.4, 9.33)	**19.8 (8.80, 68.7)**	**-47.2 (-54.2, -38.6)**
MSWX	212	4.06 (1.90, 31.9)	**54.8 (6.42, 732)**	**-43.6 (-55.9, -21.5)**	**82.0 (18.0, 1310)**	**-46.6 (-52.3, -37.2)**

Table 2.2.2: *Observed event magnitude and return period of the 2026 pr-JASO in Sumatra, as well as the probability ratio and change in magnitude for pr-JASO in Sumatra due to both GMST and RONI ASO. Statistically significant trends at the 95% confidence level are highlighted in* ***bold*** *font.*

2.2.3 Temperature

For the mean August–October (ASO) seasonal temperature over Sumatra, the return period estimates indicate that the temperatures observed in 2026 are very rare in the present climate under the prevailing ENSO conditions across three datasets (Table 2.2.3). The observed event magnitude ranges from 28.13°C in JRA-3Q to 29.4°C in CPC, reflecting minor differences in the representation of temperature across the datasets. The estimated changes in the intensity and probability of occurrence due to human-induced climate change and ENSO are presented in Table 2.2.3, expressed as probability ratios and changes in temperature intensity for such events.

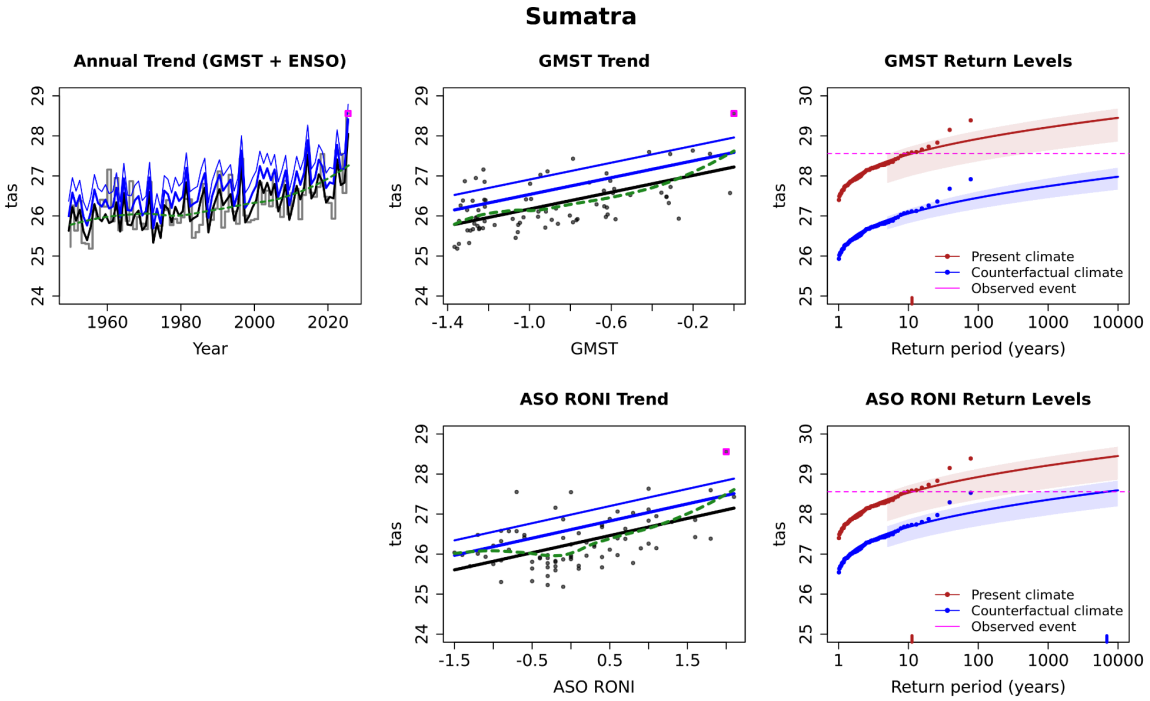


Figure 2.2.3: *Time series (left), fitted trends (middle) and return period curves (right) for August-October mean temperatures (tas ASO) in Sumatra due both GMST and RONI ASO using ERA5-Land data (all panels as in Figure 2.1.3 but for tas-ASO in Sumatra).*

The results also indicate a relationship between seasonal temperature and ENSO, suggesting that under neutral ENSO conditions, temperatures of this magnitude would have been less likely. Although the annual time series of mean ASO temperature exhibits interannual variability, the analysis indicates a strong relationship with GMST and ENSO conditions. Compared with neutral ENSO conditions, the 2026 El Niño increased the likelihood of experiencing temperatures as high as those observed this year by a factor of 12 in CPC, 74 in MSWX, 261 in JRA-3Q and more than 600 in ERA5-Land. The corresponding increases in temperature intensity range from 0.41°C to 0.86°C, with all three datasets indicating statistically significant changes at the 95% confidence level. Similarly human-induced warming has substantially increased the likelihood and intensity of high seasonal temperatures. All three datasets yield large (tending to infinite) best-estimate probability ratios, indicating that temperatures of this magnitude would have been extremely unlikely in the absence of anthropogenic warming. The estimated increases in temperature intensity range from approximately 1.41°C to 2.08°C, with all three datasets showing statistically significant changes at the 95% confidence level

Dataset	**ASO tas**		**Change due to 1.4°C global warming (95% C.I.)**		**Change due to RONI ASO (95% C.I.)**	
	Event magnitude	**Return period (yr)**	**Probability ratio**	**Change in magnitude**	**Probability ratio**	**Change in magnitude**
ERA5-Land	28.56	11.25 (4.25, 171.20)	1.2e+6 (6719.43, 8.7e+10)	1.47 (1.06, 1.78)	615.42 (86.03, 4.7e+4)	0.86 (0.67, 1.03)
JRA-3Q	28.13	18.02 (1.78, 493.42)	3.8e+15 (1.4e+12,1.4e+23)	1.46 (1.26, 1.66)	261.41 (42.01, 7643.27)	0.41 (0.27, 0.55)
MSWX	29.34	3.94 (1.63, 3797)	7.4e+15 (9.9e+10, 2.2e+20)	2.05 (1.6, 2.5)	74.15 (13.99, 2779.33)	0.55 (0.37, 0.72)
CPC	29.4	18.67 (4.60, 1529.51)	9.03e+24 (2.3e+18,2.7e+47)	2.08 (1.69, 2.43)	12.44 (1.44, 819.94)	0.23 (0.04, 0.43)

Table 2.2.3: *Observed event magnitude and return period of the 2026 mean August-October seasonal temperature (ASO tas) in Sumatra, as well as the probability ratio and change in magnitude for ASO tas in Sumatra due to both GMST and RONI ASO. Statistically significant trends at the 95% confidence level are highlighted in* ***bold*** *font.*

2.3 Java

2.3.1 VPD

For the 7-day maximum VPD, the return period estimates suggest that the conditions observed in August-October 2026 are now relatively common in the present climate given such ENSO conditions, with such accumulations expected approximately twice every 3 years (Table 2.3.1). However, it is worthy of note that there is also a strong relationship between the index and ENSO, suggesting that in neutral conditions, such an event would still be between 4-9 times less likely, or a ~6-14 year event.

The estimates of return period are consistent across the datasets with substantially overlapping 95% confidence intervals (Table 2.3.1), and we note that the observed magnitude is lower in the MSWX dataset due to the use of daily mean near-surface relative humidity (hurs) rather than the daily minimum (hursmin) in calculating the VPD. The results for the change in characteristics of such extremes with human-caused climate change and with ENSO conditions in each of the observational datasets are also shown in Table 2.3.1, with both probability ratios for events of equivalent intensity, and changes in intensity of an event of equivalent likelihood.

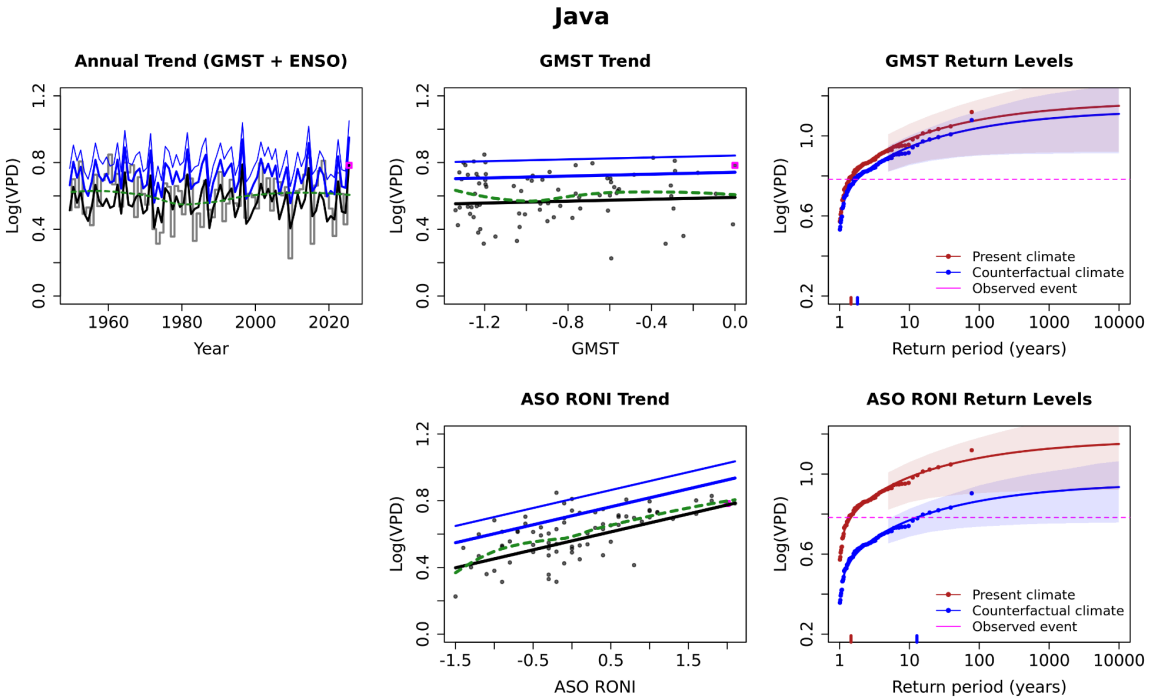


Figure 2.3.1: *Time series (left), fitted trends (middle) and return curves (right) for Log(VPDX7x) in Java for both GMST and RONI ASO using ERA5-Land data (all panels as in Figure 2.1.1 but for VPDX7x in Java).*

While the annual time series of VPDX7x shows substantial variability, this is well captured by the statistical model (Fig. 2.4) and, as with the models for Sumatra, the return curves of the fitted GEV provide a good fit to the data. As described above, higher RONI ASO is associated with increases in this index, matching the almost monotonically increasing loess smoothed trend. The results suggest that compared to a neutral RONI ASO, the current El Niño resulted in a strong increase in the 7-day maximum VPD during the ASO season: by a factor of approximately 4-9 in PR and 0.14-0.52 in

intensity, with results from all datasets statistically significant at the 95% confidence level. However, there appears to be only a very weak connection with GMST, if any. Compared to a comparable El Niño year in a preindustrial climate, human-induced warming resulted in a very small increase: ERA5-Land and JRA-3Q suggest increases by a factor of approximately 1.2-1.5 in PR and 0.09-0.17 kPa in intensity, while MSWX suggests a slight decrease or no change, with none of the results significant at the 95% level.

Dataset	**VPDX7x**		**Change due to 1.4°C global warming (95% C.I.)**		**Change due to RONI ASO (95% C.I.)**	
	Event magnitude (kPa)	**Return period (yr)**	**Probability ratio**	**Change in magnitude (kPa)**	**Probability ratio**	**Change in magnitude (kPa)**
ERA5-Land	2.19	1.46 (1.13, 3.08) 1.5	1.24 (0.559, 2.15) 1.25 (0.544, 2.24)	0.086 (-0.161, 0.284)	**8.76** **(4.34, inf)** **9.49** **(4.57, inf)**	**0.423** **(0.280, 0.524)**
JRA-3Q	2.80	1.15 (1.01, 1.60) 1.5	1.23 (0.859, 2.09) 1.48 (0.746, 4.37)	0.172 (-0.125, 0.503)	**3.56** **(1.70, 10.0)** **7.82** **(2.98, inf)**	**0.521** **(0.364, 0.671)**
MSWX (Hurs)	1.11	1.17 (1.00, 1.73) 1.5	0.936 (0.641, 1.38) 0.860 (0.340, 2.01)	-0.0401 (-0.234, 0.155)	**1.96** **(1.19, 4.99)** **3.89** **(1.52, inf)**	**0.137** **(0.0731, 0.220)**

Table 2.3.1: *Observed event magnitude and return period of the 2026 VPDX7x in Java, as well as the probability ratio and change in magnitude for VPDX7x in Java due to both GMST and RONI ASO. Statistically significant trends at the 95% confidence level are highlighted in* ***bold*** *font.*

2.3.2 Precipitation

Figure 2.3.2 shows the non-stationary Gaussian model that scales with GMST and RONI ASO fitted to the pr-JASO time series from ERA5-Land for the Java study region. Table 2.3.2 summarises the results from fitting the statistical models to all four datasets (CPC, ERA5-Land, JRA-3Q and MSWX). Contrary to the other two study regions (Borneo and Sumatra), there is good agreement between the datasets in the estimates in the rarity, as well as the change in likelihood and the intensity. The event has a return period of 2 to 7 years in today's climate characterised by 1.4°C warming above pre-industrial levels and ENSO conditions characterised by 2026 RONI ASO. Together, the datasets suggest that low precipitation events such as the 2026 event in the Java study region has been made ~2-6 times more likely and ~50-60% drier due to the 1.4°C warming between pre-industrial climate and the present day, and ~3-16 times more likely and ~70-80% drier under strong El Niño conditions as characterised by the 2026 RONI ASO, as compared to neutral ENSO conditions. While the contribution of ENSO to low precipitation magnitudes is consistent with the findings for the other study regions, the statistically robust 40–60% reduction in precipitation totals associated with GMST

increases appears to be relatively unique to Java. However, given the high interannual variability, we refrain from putting emphasis on these estimates, and simply conclude that both increasing GMST and El Niño conditions contribute to lower pr-JASO totals over Java.

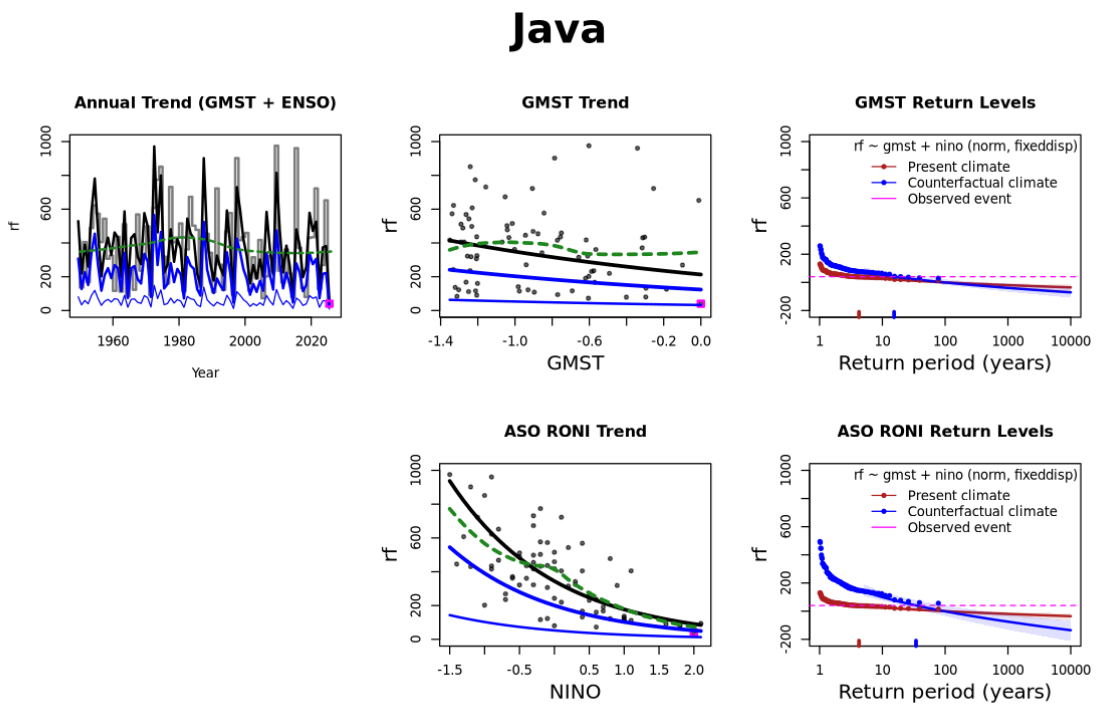


Figure 2.3.2: *Time series (left), fitted trends (middle) and return curves (right) for low precipitation events based on pr-JASO in Java for both GMST and RONI ASO using ERA5-Land data (all panels as in Figure 2.1.2 but for pr-JASO in Java).*

Dataset	**pr-JASO**		**Change due to 1.4°C global warming (95% C.I.)**		**Change due to RONI ASO (95% C.I.)**	
	Event magnitude (mm)	**Return period (yr)**	**Probability ratio**	**Change in magnitude (%)**	**Probability ratio**	**Change in magnitude (%)**
CPC	12.2	7.35 (2.66, 26.5)	**2.32 (1.02, 8.56)**	**-62.3 (-84.0, -3.33)**	**3.03 (1.38, 12.3)**	**-79.8 (-87.5, -60.3)**
ERA5-Land	40.4	4.24 (2.07, 12.0)	**3.62 (1.55, 9.89)**	**-49.8 (-66.1, -24.3)**	**8.10 (3.17, 25.9)**	**-73.7 (-80.1, -62.8)**
JRA-3Q	27.3	2.34 (1.30, 5.47)	**3.10 (1.59, 6.96)**	**-58.6 (-74.9, -31.6)**	**5.14 (2.57, 14.5)**	**-77.6 (-85.9, -65.1)**
MSWX	61.1	1.42 (1.06, 4.34)	**6.46 (1.57, 31.5)**	**-60.4 (-78.2, -19.5)**	**16.0 (5.89, 73.9)**	**-76.5 (-80.6, -67.5)**

Table 2.3.2: *Observed event magnitude and return period of the 2026 pr-JASO in Java, as well as the probability ratio and change in magnitude for pr-JASO in Java due to both GMST and RONI ASO. Statistically significant trends at the 95% confidence level are highlighted in* ***bold*** *font.*

2.3.3 Temperature

In Java, the return period estimates suggest that the temperatures observed in 2026 are relatively common in the present GMST conditions and under the prevailing ENSO conditions. The estimated return periods range from 2 to 4 years across the four datasets (Table 2.3.3), with overlapping 95% confidence intervals.

The estimated changes due to human-induced climate change and ENSO are presented in Table 2.3.3, expressed as probability ratios and changes in temperature intensity. Results indicate a strong and consistent influence of anthropogenic warming on ASO temperatures over Java. Compared with a pre-industrial climate, under comparable ENSO conditions, human-induced warming has significantly increased the likelihood of experiencing temperatures as high as those observed in 2026. The estimated probability ratios range from 930 in JRA-3Q to above 73,000 in ERA5-Land, with MSWX indicating an increase by a factor of approx. 4,250 and CPC showing an infinite probability ratio. The corresponding increases in temperature intensity range from 0.81°C to 1.80°C, with all four datasets showing statistically significant changes at the 95% confidence level.

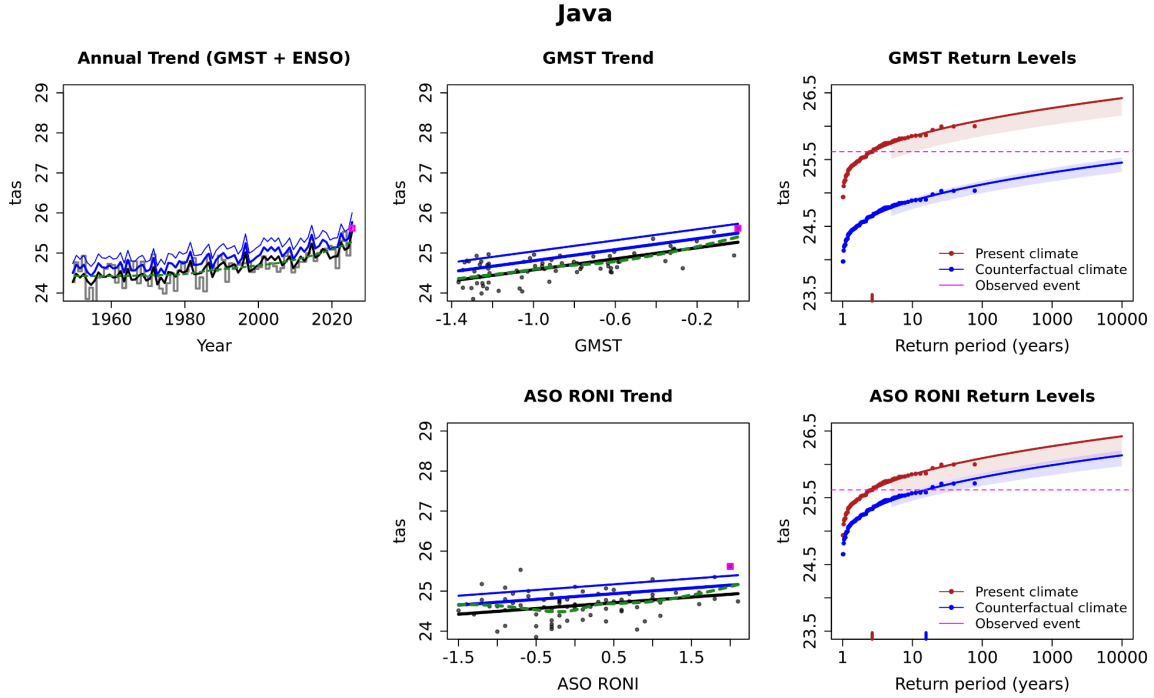


Figure 2.3.3: *Time series (left), fitted trends (middle) and return period curves (right) for August-October mean temperatures (tas ASO) in Java due both GMST and RONI ASO using ERA5-Land data (all panels as in Figure 2.1.3 but for tas-ASO in Java).*

The results also suggest that ENSO influences seasonal temperatures over Java, although the magnitude and direction of this influence vary across the datasets. ERA5-Land suggests that the prevailing El Niño conditions increased the likelihood of the event by a factor of 5.9 and increased its intensity by 0.28°C, with both changes statistically significant. JRA-3Q indicates a smaller increase in likelihood and intensity, although neither estimate is statistically significant. MSWX and CPC, however, suggest that ENSO conditions reduced the likelihood of the event, with probability ratios of

0.59 and 0.50, respectively. The corresponding changes in temperature intensity are both −0.20°C, although only the MSWX estimate is statistically significant. Overall, these results show that that human-induced warming has substantially increased ASO temperatures over Java, while the influence of El Niño is less robust, with differences in both the magnitude and direction of the estimated response across datasets

Dataset	**ASO tas**		**Change due to 1.4°C global warming (95% C.I.)**		**Change due to RONI ASO (95% C.I.)**	
	Event magnitude	**Return period (yr)**	**Probability ratio**	**Change in magnitude**	**Probability ratio**	**Change in magnitude**
ERA5-Land	25.62	2.66 (1.58,7,44)	**73806.22 (4979.15,12053264.21)**	0.97 (0.75,1.16)	**5.90 (2.69,19.94)**	0.28 (0.16,0.40)
JRA-3Q	26.27	2.56 (1.47,8.46)	**929.93 (143.07,16109.08)**	0.81 (0.57,1.03)	1.65 (0.88,3.68)	0.12 (-0.02,0.26)
MSWX	25.69	2.27 (1.29,10.99)	**4250.72 (135.16,1544804.92)**	0.84 (0.53,1.13)	0.59 (0.16,0.92)	-0.20 (-0.37,-0.05)
CPC	27.34	4.02 (1.80,40.43)	**inf**	1.80 (1.37,2,17)	0.50 (0.10,0.99)	-0.20 (-0.39,0.01)

Table 2.3.3: *Observed event magnitude and return period of the 2026 mean August-October seasonal temperature (ASO tas) in Java, as well as the probability ratio and change in magnitude for ASO tas in Java due to both GMST and RONI ASO. Statistically significant trends at the 95% confidence level are highlighted in* ***bold*** *font.*

2.4 Western Indonesia

2.4.1 VPD

For the 7-day maximum VPD, the return period estimates suggest that the conditions observed in August-October 2026 are now relatively common in the present climate given such ENSO conditions, with such accumulations expected approximately twice every 3 years (Table 2.4.1). However, it is worthy of note that there is also a strong relationship between the index and ENSO, suggesting that in neutral conditions, such an event would still be between 15-39 times less likely, or a ~20-60 year event.

The estimates of return period are consistent across the datasets with substantially overlapping 95% confidence intervals (Table 2.4.1), and we note that the observed magnitude is lower in the MSWX dataset due to the use of daily mean near-surface relative humidity (hurs) rather than the daily minimum (hursmin) in calculating the VPD. The results for the change in characteristics of such extremes with human-caused climate change and with ENSO conditions in each of the observational

datasets are also shown in Table 2.4.1, with both probability ratios for events of equivalent intensity, and changes in intensity of an event of equivalent likelihood.

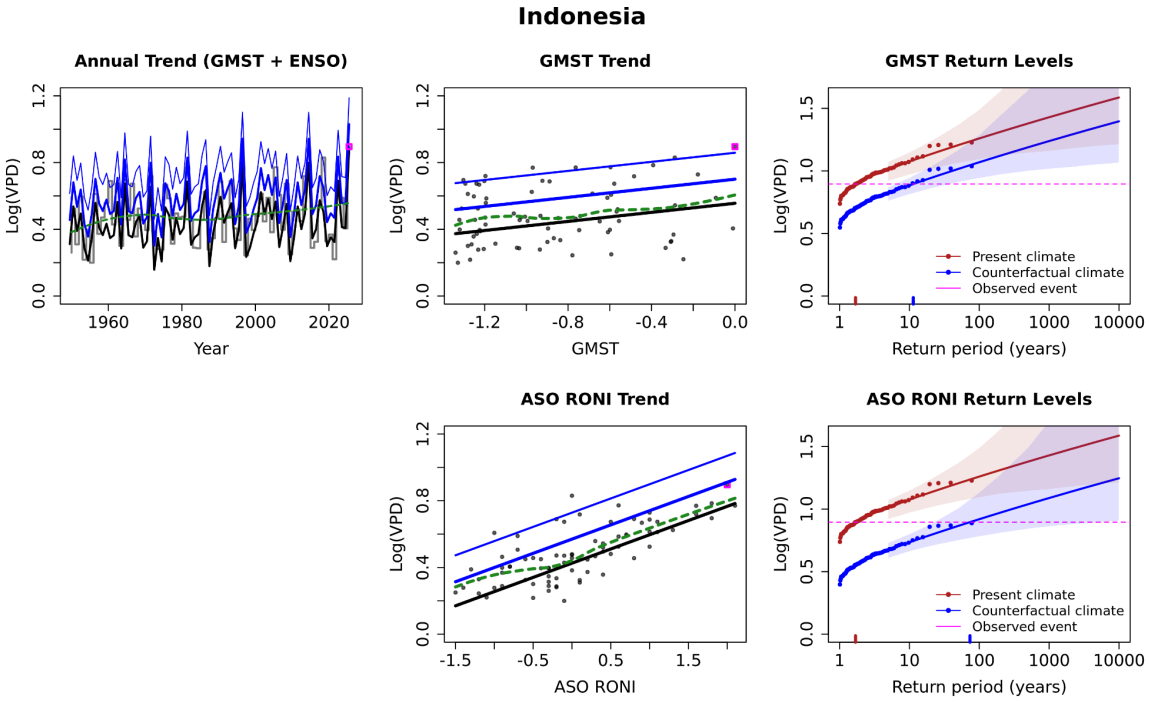


Figure 2.4.1: *Time series (left), fitted trends (middle) and return curves (right) for Log(VPDX7x) in western Indonesia for both GMST and RONI ASO using ERA5-Land data (all panels as in Figure 2.1.1 but for VPDX7x in western Indonesia).*

While the annual time series of VPDX7x shows substantial variability, this is well captured by the statistical model (Fig. 2.4.1), and the GEV again provides a good fit to the data. In this region, both higher GMST and RONI ASO are again associated with increases in this index, matching the almost monotonically increasing loess smoothed trend in each case. The results suggest that compared to a neutral RONI ASO, the current El Niño resulted in a strong increase in the 7-day maximum VPD during the ASO season: by a factor of 15-39 in PR and 0.49-0.71 kPa in intensity, with results from all datasets statistically significant at the 95% confidence level. Similarly, compared to a comparable El Niño year in a preindustrial climate, human-induced warming resulted in a strong increase, with different datasets again giving a wide range of estimates: ERA5-Land and JRA-3Q suggest increases by a factor of approximately 6-13 in PR and 0.42-0.59 kPa in intensity, while MSWX suggests that such conditions would have been around 40 times less likely, though with a similar change in intensity. Results from all datasets are again statistically significant at the 95% confidence level.

Dataset	**VPDX7x**		**Change due to 1.4°C global warming (95% C.I.)**		**Change due to RONI ASO (95% C.I.)**	
	Event magnitude (kPa)	**Return period (yr)**	**Probability ratio**	**Change in magnitude (kPa)**	**Probability ratio**	**Change in magnitude (kPa)**
ERA5-Land	2.45	1.69 (1.21, 3.71)	**6.72 (3.03, 20.2)**	**0.424 (0.229, 0.572)**	**43.5 (15.3, 1720)**	**0.708 (0.598,**

						0.789)
JRA-3Q	2.68	1.09 (1.01, 1.29)	**5.94 (2.70, 19.0)**	**0.592 (0.398, 0.772)**	**6.40 (3.53, 23.4)**	**0.605 (0.494, 0.720)**
MSWX (Hurs)	1.65	1.43 (1.03, 2.60)	**40.8 (9.68, inf)**	**0.506 (0.338, 0.690)**	**34.2 (11.3, inf)**	**0.488 (0.372, 0.559)**

Table 2.4.1: *Observed event magnitude and return period of the 2026 VPDX7x in western Indonesia, as well as the probability ratio and change in magnitude for VPDX7x in western Indonesia due to both GMST and RONI ASO. Statistically significant trends at the 95% confidence level are highlighted in* ***bold*** *font.*

2.4.2 Precipitation

Figure 2.4.2 shows the non-stationary Gaussian model that scales with GMST and RONI ASO fitted to the pr-JASO time series from ERA5-Land for the western Indonesia study region that comprises Borneo, Sumatra and Java study regions. Table 2.4.2 summarises the results from fitting the statistical models to all four datasets (CPC, ERA5-Land, JRA-3Q and MSWX). With the exception of CPC, the other datasets suggest that JASO season is becoming drier, with the likelihood of seeing low pr-JASO such as the event under study increasing 4 to 20 times, and 18 to 30% drier as compared to a low precipitation event of similar rarity in a 1.4°C climate. Once again, all datasets agree on the contribution of ENSO characterised by RONI ASO- although the PRs show a wide range in the best estimates (~50 to 290; lower bound >15%), the values qualitatively suggest that the 2026 low precipitation event during July to October over the wider western Indonesia study region would have been virtually impossible under neutral ENSO conditions and would have been ~50% wetter.

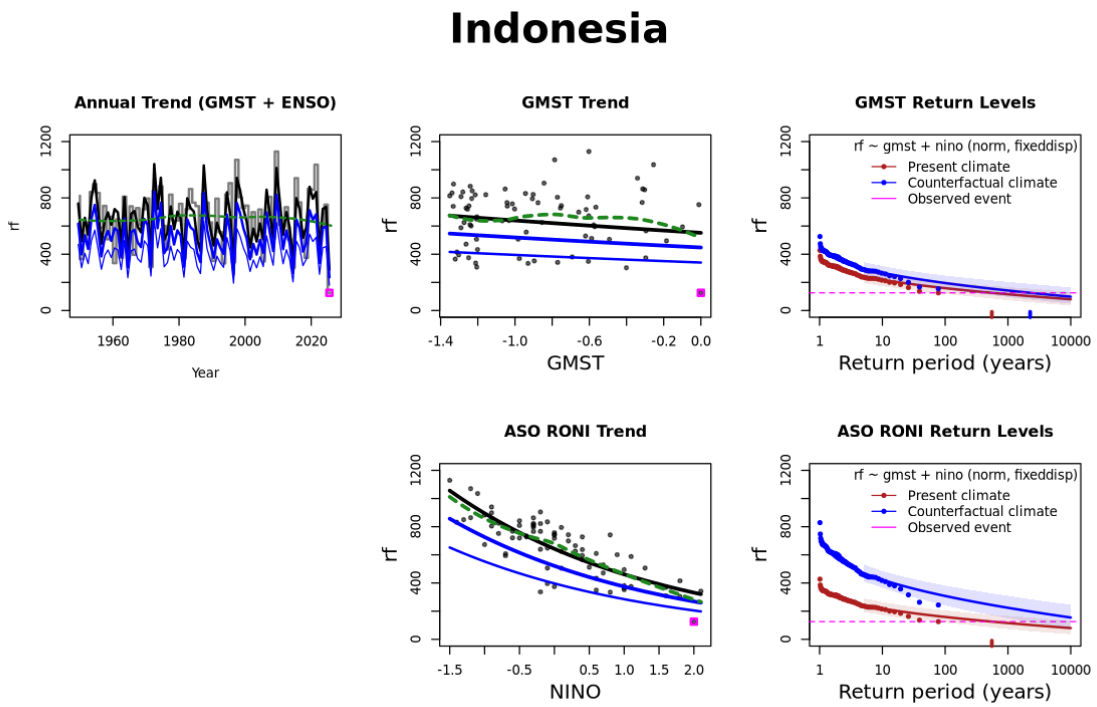


Figure 2.4.2: *Time series (left), fitted trends (middle) and return curves (right) for low precipitation events based on pr-JASO in western Indonesia for both GMST and RONI ASO using ERA5-Land data (all panels as in Figure 2.1.2 but for pr-JASO in western Indonesia).*

Dataset	**pr-JASO**		**Change due to 1.4°C global warming (95% C.I.)**		**Change due to RONI ASO (95% C.I.)**	
	Event magnitude (mm)	**Return period (yr)**	**Probability ratio**	**Change in magnitude (%)**	**Probability ratio**	**Change in magnitude (%)**
CPC	276	1.60 (1.05, 3.69)	0.909 (0.435, 2.10)	3.55 (-21.8, 36.9)	**54.9 (15.3, 825)**	**-54.0 (-60.6, -46.0)**
ERA5-Land	126	554 (67.5, 24479)	**4.07 (1.46, 17.7)**	**-18.7 (-31.3, -5.70)**	**53.1 (18.1, 498)**	**-48.4 (-54.4, -42.2)**
JRA-3Q	240	3.87 (1.99, 11.0)	**2.77 (1.17, 6.95)**	**-18.3 (-31.2, -2.96)**	**45.7 (18.3, 212)**	**-51.4 (-56.8, -45.0)**
MSWX	161	36.2 (5.65, 1149)	**20.9 (2.49, 379)**	**-30.9 (-47.5, -9.25)**	**293 (64.4, 10098)**	**-51.5 (-57.7, -44.7)**

Table 2.4.2: *Observed event magnitude and return period of the 2026 pr-JASO in western Indonesia, as well as the probability ratio and change in magnitude for pr-JASO in western Indonesia due to both GMST and RONI ASO. Statistically significant trends at the 95% confidence level are highlighted in* ***bold*** *font.*

The absence of a consistent trend with GMST across the sub-study regions and the wider western Indonesia region does not necessarily indicate an absence of climate change signal. Rather, the high year-to-year variability may mask the emergence of a detectable long-term trend associated with

GMST increases. Given the role of the exceptional dry conditions also contributing to the widespread and impactful wildfires in the region, we extend the attribution analysis to include climate model simulations as well, to investigate the contributions from human-induced climate change and ENSO conditions in the likelihood and magnitude of low precipitation seasons in western Indonesia. For this analysis, we use an approximate return period of 20 years for the 2026 pr-JASO event over western Indonesia to define the event in climate model simulations. Given the large differences between datasets and the associated uncertainties in estimating the rarity of the event (2–554 years), we consider 20 years a reasonable working estimate for defining the event in the climate model attribution analysis.

2.4.3 Temperature

Across the wider western Indonesian region, estimates of the return period of the mean August–October (ASO) seasonal temperatures observed in 2026 suggest that such conditions are relatively common in the present climate under the prevailing ENSO conditions. JRA-3Q, MSWX and CPC indicate return periods of approximately 2–5 years, while ERA5-Land suggests a considerably rarer event, with an estimated return period of approximately 46 years (Table 2.4.3). Despite these differences in the best estimates, the 95% confidence intervals overlap substantially, reflecting considerable uncertainty in the estimated rarity of the event. For the climate model analysis, we adopt a 20-year return period to assess changes in the intensity and likelihood of extreme seasonal temperatures across the wider *western* Indonesian region.

The observed event magnitude ranges from 27.53°C in JRA-3Q to 28.67°C in MSWX, broadly consistent with the ASO mean temperatures observed across the individual subregions. Table 2.4.3 presents the estimated changes in the intensity and likelihood of such temperatures due to human-induced climate change and ENSO. The results indicate a strong and consistent influence of anthropogenic warming on seasonal temperatures across western Indonesia. All four observational datasets show infinite best-estimate probability ratios, suggesting that temperatures of this magnitude would have been extremely unlikely in a pre-industrial climate, under comparable ENSO conditions. The corresponding increases in temperature intensity range from approximately 1.41°C in ERA5-Land to 1.99°C in CPC, with all four datasets indicating statistically significant increases at 95% CL.

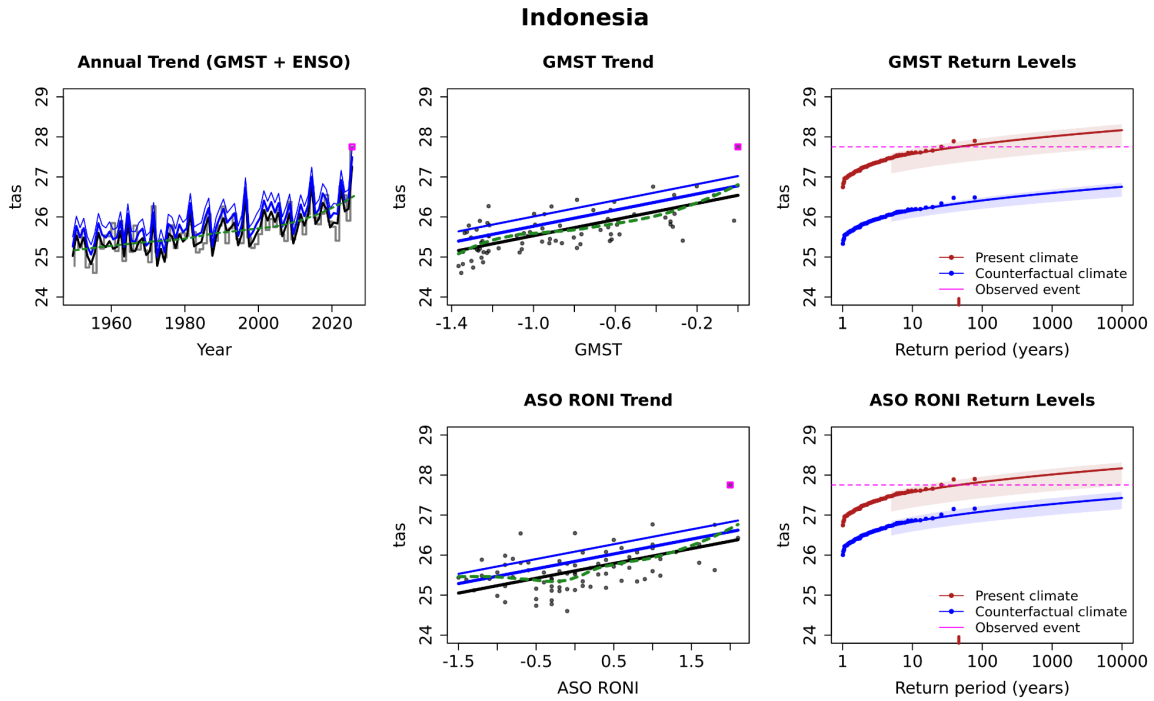


Figure 2.4.3: *Time series (left), fitted trends (middle) and return period curves (right) for August-October mean temperatures (tas ASO) in western Indonesia due both GMST and RONI ASO using ERA5-Land data (all panels as in Figure 2.1.3 but for tas-ASO in western Indonesia).*

ENSO also contributed to elevated ASO temperatures across western Indonesia, although the magnitude and statistical significance of its influence vary among datasets. Compared with neutral ENSO conditions, the prevailing ENSO conditions increased the likelihood of temperatures as high as those observed in 2026 by a factor of approx. 59 in JRA-3Q, 122 in MSWX and more than 96,000 in ERA5-Land. The corresponding increases in temperature intensity range from 0.41°C to 0.74°C, with all three datasets indicating statistically significant changes at the 95% confidence level. CPC, however, suggests a substantially weaker ENSO influence, with a probability ratio of 2.59 (95% CI: 0.90–12.81) and an increase in temperature intensity of 0.12°C (95% CI: −0.01–0.25°C). Neither estimate is statistically significant at the 95% cl.

Dataset	**ASO tas**		**Change due to 1.4°C global warming (95% C.I.)**		**Change due to RONI ASO (95% C.I.)**	
	Event magnitude	**Return period (yr)**	**Probability ratio**	**Change in magnitude**	**Probability ratio**	**Change in magnitude**
ERA5-Land	27.75	46.25 (9.04,3034.40)	inf	**1.41 (1.15,1.63)**	**96661.44 (6107.76,32605801.09)**	0.74 (0.59,0.88)
JRA-3Q	27.53	2.17 (1.39,5.19)	inf	**1.67 (1.51,1.82)**	**59.11 (15.97,588.30)**	0.41 (0.32,0.51)
MSWX	28.67	4.97 (1.95,94.02)	inf	**1.65 (1.33,1.97)**	**122.11 (28.34,3637.17)**	0.41 (0.29,0.54)

CPC	28.43	3.98 (1.73,40.84)	inf	**1.99 (1,68,2.30)**	**2.59 (0.90,12.81)**	0.12 (-0.01,0.25)

Table 2.4.3: *Observed event magnitude and return period of the 2026 mean August-October seasonal temperature (ASO tas) in western Indonesia, as well as the probability ratio and change in magnitude for ASO tas in western Indonesia due to both GMST and RONI ASO. Statistically significant trends at the 95% confidence level are highlighted in* ***bold*** *font.*

2.5 Summary of observed trends

In this section we studied changes in three variables that influence conditions conducive to fires - the 7-day maximum VPD during August-October, the July-October accumulated precipitation, and the August-October mean temperature. This analysis was undertaken for three subregions of western Indonesia - Borneo, Java and Sumatra - and the wider western Indonesia study region combining all three. The qualitative results are summarised in Table 2.5.1.

Across all regions, the influence of global warming on seasonal temperature is extremely strong. While estimates of the return period of the seasonal temperatures in current conditions varied between regions, historical trends suggest that such temperatures would have been virtually impossible without global warming of 1.4°C in all regions. And, equivalently, that this warming has increased the seasonal temperatures at a rate of roughly 1-1.5x the mean global warming rate in all regions except Java, which has warmed more slowly. This, and the narrow confidence interval on temperature trends, is consistent with the fact that the Maritime Continent is expected to see the highest signal-to-noise ratio of any highly populated region of the world at all global warming levels (Harrington, 2021). The influence of RONI ASO on the seasonal temperatures varied between regions. In the Borneo, Sumatra and aggregated regions, the RONI ASO made such temperatures more likely and hotter but at a rate much lower than global warming. In Java, the qualitative role of the RONI ASO varied between datasets, showing no clear signal.

Findings vary more between regions for VPDX7x and seasonal precipitation. In the Borneo and Sumatra regions, we found that the observed VPDX7x is not an unexpected event given present levels of warming and the RONI ASO conditions, and that both of these drivers made the event substantially more likely and intense by a broadly comparable amount. For seasonal precipitation, while the balance of evidence suggests that global warming decreased the accumulations in these two regions, the effect was challenging to quantify. Meanwhile, the role of the RONI ASO was strong and statistically significant across all datasets and suggested that these conditions approximately halved the seasonal accumulations. In Java, there was no clear role for climate change in the high VPD event, though RONI ASO significantly increased its likelihood and intensity. However, both drivers played a substantial role in the seasonal precipitation, with global warming reducing the totals by approximately 50-60% and RONI ASO by 70-80%.

Finally, in the wider western Indonesia region, both climate change and the RONI ASO played significant roles in the likelihood and intensity of such a high VPDX7x event and a low accumulation of seasonal precipitation. For VPD, the trends suggest that climate change and the RONI ASO made such an event about 0.5 kPa and 0.6 kPa more intense, respectively. Meanwhile, for seasonal

precipitation, RONI ASO played the dominant role, reducing the seasonal totals by approximately 50%, with climate change contributing around a 16% decrease on average across the datasets.

Region	Event index	Role of GMST	Role of RONI	Dominant driver
Borneo	High VPDX7x	Increase	Increase	Comparable
	Low seasonal precipitation	Increase	Increase	El Niño
	High seasonal temperature	Increase	Increase	GMST
Sumatra	High VPDX7x	Increase	Increase	Comparable
	Low seasonal precipitation	Increase	Increase	El Niño
	High seasonal temperature	Increase	Increase	GMST
Java	High VPDX7x	Unclear	Increase	El Niño
	Low seasonal precipitation	Increase	Increase	Comparable
	High seasonal temperature	Increase	Unclear	GMST
Western Indonesia	High VPDX7x	Increase	Increase	Comparable
	Low seasonal precipitation	Increase	Increase	El Niño
	High seasonal temperature	Increase	Increase	GMST

Table 2.5.1: *Summary of qualitative influences of GMST and RONI ASO upon each variable in each region studied in this section. This table covers observed relationships, with the dominant driver designated as 'comparable' when both drivers had the same order of magnitude.*

3 Attribution of trends

3.1 Evaluation of climate models

For each variable, the climate models used are evaluated against the observations in their ability to capture:

1. Seasonal cycles: For this, we qualitatively compare the seasonal cycles based on model outputs against observations-based cycles. We discard the models that exhibit ill-defined peaks in their seasonal cycles. For example, we discard the model if the rainy season onset/termination varies significantly from the observations.

2. Spatial patterns: Models that do not match the observations in terms of the large-scale mean patterns of each variable (VPD, precipitation and temperature) during the season of study are excluded. For all variables, we also discard models with a resolution that is too coarse to capture the islands studied, requiring at least four grid cells for each of the major island regions after applying the region mask.

3. Parameters of the fitted statistical models. We discard the model if the model and observation parameter uncertainty ranges do not overlap, with the specific parameters used depending on the statistical distribution used. For the seasonal precipitation, we compare the dispersion of the fitted gaussian and the correlation between the variable and the RONI ASO, for temperature we compare the sigma parameter of the fitted gaussian and the RONI ASO correlation, and for VPD we compare the sigma and shape parameters of the fitted GEV, and additionally explore the sensitivity of the results to evaluating the RONI ASO correlation (see Tables A2.1.1 & A2.1.2).

The models are labelled as ‘good’,’reasonable’, or ’bad’ based on their performances in terms of the three criteria discussed above. A model is given an overall rating of ‘good’ if it is rated ‘good’ for all three characteristics. If there is at least one ‘reasonable’, then its overall rating will be ‘reasonable’ and ‘bad’ if there is at least one ‘bad’. Tables of the model evaluation results can be found in Appendix A2.

For VPDX7x, 30 CMIP6 models were evaluated including some with both hurs and hursmin data available. Of these, one was ranked ‘good’ across all three assessment criteria, while 5 others received an overall ‘reasonable’ ranking. Of the six CORDEX models, one achieved a ‘good’ ranking across all criteria and one received a ‘reasonable’ ranking. We therefore used all available good and reasonable models in the synthesis, and further provided synthesis results for the additional evaluation step including RONI ASO correlation described above, which limited the total number of models to 4, which affected the exact quantification but not the qualitative results.

For precipitation (pr-JASO), 41 CMIP6 models were evaluated. Of these, five were ranked ‘good’ across all three assessment criteria, while 24 received an overall ‘reasonable’ ranking. Among the latter, seven models were ranked ‘good’ in two of the three criteria. None of the eight CORDEX models achieved a ‘good’ ranking across all criteria, while three received an overall ‘reasonable’ ranking. For the final synthesis (Section 3.2.2), we selected the five CMIP6 models that ranked ‘good’

across all criteria and the three CORDEX models that ranked ‘reasonable’. We also tested the sensitivity of the results to include the seven additional CMIP6 models that were ranked ‘good’ in two of the three criteria. This inclusion did not affect the results (not shown), and therefore, they are excluded from the final synthesis.

For the August–October (ASO) mean temperature (tas-ASO) analysis, 30 CMIP6 and 7 CORDEX models were evaluated. In addition to the three evaluation criteria described above, models were assessed for their ability to reproduce the observed correlation between tas-ASO and the ASO RONI. Only models classified as ‘good’ or ‘reasonable’ were retained for the attribution analysis. Of the 30 CMIP6 models, 6 were rated ‘good’ and 11 ‘reasonable’, while 2 of the 7 CORDEX models were rated ‘good’ and 4 ‘reasonable’. Consequently, a total of 23 models (17 CMIP6 and 6 CORDEX) were included in the final synthesis to assess changes in tas-ASO.

3.2 Synthesis of results

For the event definitions described above we evaluate the influence of anthropogenic climate change and RONI ASO on the events by calculating the probability ratio as well as the change in intensity using observations and climate models. Models which do not pass the evaluation described above are excluded from the analysis. The aim is to synthesise results from models that pass the evaluation along with the observations-based products, to give an overarching attribution statement. Tables of the results of this model fitting can be found in Appendix A3.

Figures 3.1-3.6 show the changes in probability and intensity for the observations (blue) and models (red). Before combining them into a synthesised assessment, first, a representation error is added (in quadrature) to the observations, to account for the difference between observations-based datasets that cannot be explained by natural variability. This is shown in these figures as white boxes around the light blue bars. The dark blue bar shows the average over the observation-based products. Next, [a term to account for intermodel spread is added (in quadrature) to the natural variability of the models. This is shown in the figures as white boxes around the light red bars. The dark red bar shows the model average, consisting of a weighted mean using the (uncorrelated) uncertainties due to natural variability plus the term representing intermodel spread (i.e., the inverse square of the white bars).

Observation-based products and models are combined into a single result in two ways. Firstly, we neglect common model uncertainties beyond the intermodel spread that is depicted by the model average, and compute the weighted average of models (dark red bar) and observations (dark blue bar): this is indicated by the magenta bar. As, due to common model uncertainties, model uncertainty can be larger than the intermodel spread, secondly, we also show the more conservative estimate of an unweighted, direct average of observations (dark blue bar) and models (dark red bar) contributing 50% each, indicated by the white box around the magenta bar in the synthesis figures. Here we communicate findings based on the weighted synthesis since we do not have any reason, such as based on model fidelity, to use the more conservative estimate.

3.2.1 VPD

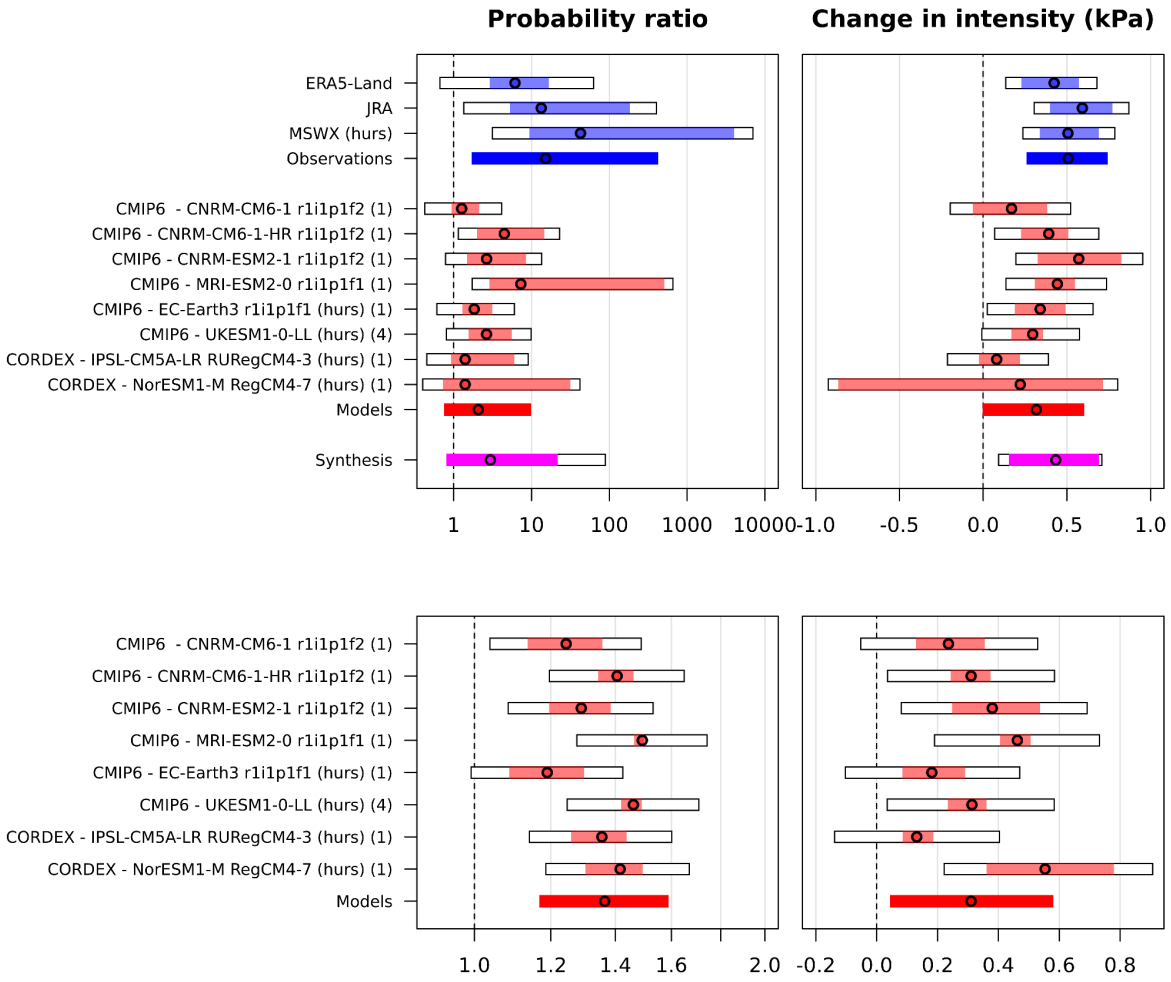


Figure 3.1: *Synthesised changes for the 1.5-year August-October 7-day maximum VPD event in the study region due to GMST. Probability ratio (left) and changes in intensity (right) are shown for a historical period comparing the past 1.4°C cooler climate with the present (top row) and for a future period, based on model projections only, comparing the present and a 2.8 °C warmed climate (bottom row).*

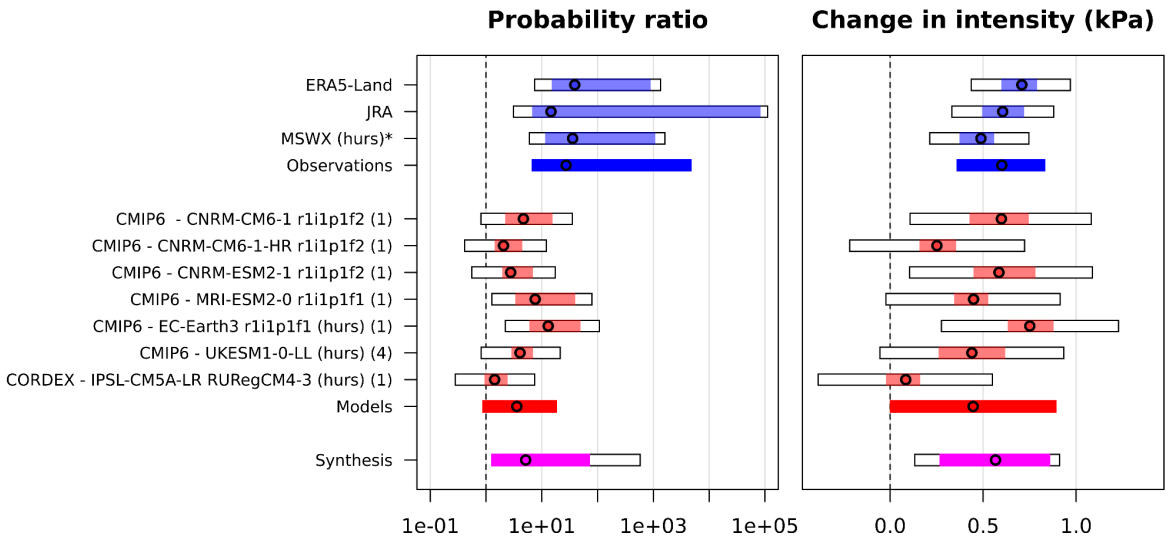


Figure 3.2: *Synthesised changes for a 1.5-year August-October 7-day maximum VPD event in the study region due to ENSO. PR (left) and change in intensity (right) are shown for the current vs neutral RONI ASO states.*

The return period of the maximum 7-day VPD in all regions was very low, with such totals expected around twice every 3 years in the present climate. Observation-based datasets suggested that over the historical record, such events as observed in 2026 have become substantially more likely and intense as the world has warmed in the wider western Indonesia study regions, and all subregions except Java. The influence of the rising El Niño during August-October was also very strong in all regions. Overall, for western Indonesia, the observations suggest that 2026-like events have become about 15 (1.7 to 420) times as likely and, equivalently, such 2-in-3 year events have become about 0.51 kPa (0.26 to 0.75 kPa) more intense as the world has warmed. The historical observations also suggested a very strong connection with the concurrent ENSO conditions, with an increase in likelihood of a factor of 27 (6.5 to 4800) and in intensity around 0.6 kPa (0.36 to 0.83 kPa).

Climate models that passed the evaluation steps (section 3.1) were then analysed in the same way based on the equivalent 1.5 year return period event, as determined from observations. In order to maximise the available data, we tested whether using hurs or hursmin to calculate the 7-day maximum VPD during ASO had a significant effect using models with both variables available, and found that the results were broadly similar (see section A2.1, Fig. A2.1.1). Therefore, we used hurs for models without hursmin available, with the relevant models indicated in Figs 3.1 & 3.2.

Observations and climate models broadly agreed that both climate change from the preindustrial period to present and the rising El Niño has driven changes in likelihood and intensity of similar extremes, though the climate models give consistently lower estimates than observations for these effects. Synthesising both data sources, we find that such conditions have become significantly more likely at around a factor of 3 (0.8 to 22) and with a change in VPD intensity of 0.43 kPa (0.16 to 0.69 kPa). In a world that warms by a further 1.4°C, models project a further intensification of such extreme conditions by a factor of 1.4 (1.2 to 1.6) in likelihood, or equivalently 0.3 kPa (0.04 to 0.58 kPa) in intensity. We also find that the ongoing El Niño also made such conditions significantly more likely at around a factor of 5.1 (1.2 to 73) and with a change in VPD intensity of 0.57 kPa (0.27 to

0.86 kPa). When removing models with a lower than expected correlation with the RONI ASO index, we find comparable but slightly larger results for both covariates (for the past change for GMST), with best estimates for the influence of GMST on likelihood of ~3.7 and RONI ASO of ~8.0.

Data	**Influence of GMST increase of 1.4°C**			**Influence of El Niño**	
	Time period	**Probability ratio (95% CI)**	**Intensity change (kPa) (95% CI)**	**Probability ratio (95% CI)**	**Intensity change (kPa) (95% CI)**
Observations	**Preindustrial - present**	**15.2 (1.70, 423)**	**0.508 (0.259, 0.745)**	**27.3 (6.53, 4830)**	**0.600 (0.357, 0.834)**
Models		2.07 (0.751, 9.87)	0.317 (-0.00305, 0.605)	3.57 (0.854, 18.7)	0.446 (-0.00242, 0.895)
Synthesis		2.96 (0.802, 21.8)	**0.433 (0.155, 0.691)**	**5.14 (1.23, 73.0)**	**0.566 (0.266, 0.861)**
Models	**Present - future**	**1.36 (1.17, 1.59)**	**0.310 (0.0436, 0.580)**		

Table 3.1: *Summary of results for VPDX7x, presented in Figs 3.1 & 3.2: changes due to GMST include past-present changes and present-future changes for the RONI ASO state of 2026, changes due to RONI ASO include El Niño versus neutral in the present climate. Statistically significant changes are highlighted in* ***bold*** *font.*

3.2.2 Precipitation

The four observed datasets used in the study have been consistent in capturing the high year-to-year variability associated with ENSO; and therefore, it is not surprising that these observations that use different algorithms for data assimilation (stations, satellites, reanalysis) and spanning different times (starting at 1950 vs. starting at 1979) do not agree on long-term trends, in part due to the gmst trends (if any) not emerging above the natural variability, and the difference in the resolutions interfering with the relative extremity of the low seasonal precipitation this year vs. previous years. Despite these differences, with exception of the short-length, coarse resolution CPC dataset, the other datasets indicate that low JASO rainfall over western Indonesia are becoming more likely in today's climate as compared to pre-industrial climate (Figure 3.3), and drier, as compared to a 1-in-20 year event in the past. Overall, the observations indicate drying, with a fourfold increase in the likelihood of low seasonal JASO rainfall relative to the pre-industrial climate, along with a ~17% reduction in the rainfall amount, for a 1-in-20-year event in today's climate. The five 'good' CMIP6 models and three 'reasonable' CORDEX models that were chosen for the attribution analysis are even less able to reflect the observed trends, with only one CMIP6 model and two CORDEX models showing 8-12% drying in the best estimates and the rest of the models close to no change, and all models encompassing no change. Synthesising the observations and the climate models, the results suggest no change. This is also the case under a future warmer world that is 2.8C above pre-industrial climate, with the synthesised estimates showing no change.

For ENSO, on the other hand the observations and the climate models are in agreement, confirming that this year's El Niño conditions have substantially contributed to the drought. The synthesised results indicate that this year's El Niño (characterised by 2026 ASO RONI in this study) has contributed to ~50% reduction (statistically significant at 95% confidence levels) in the seasonal (JASO) precipitation amount, as compared to neutral ENSO conditions.

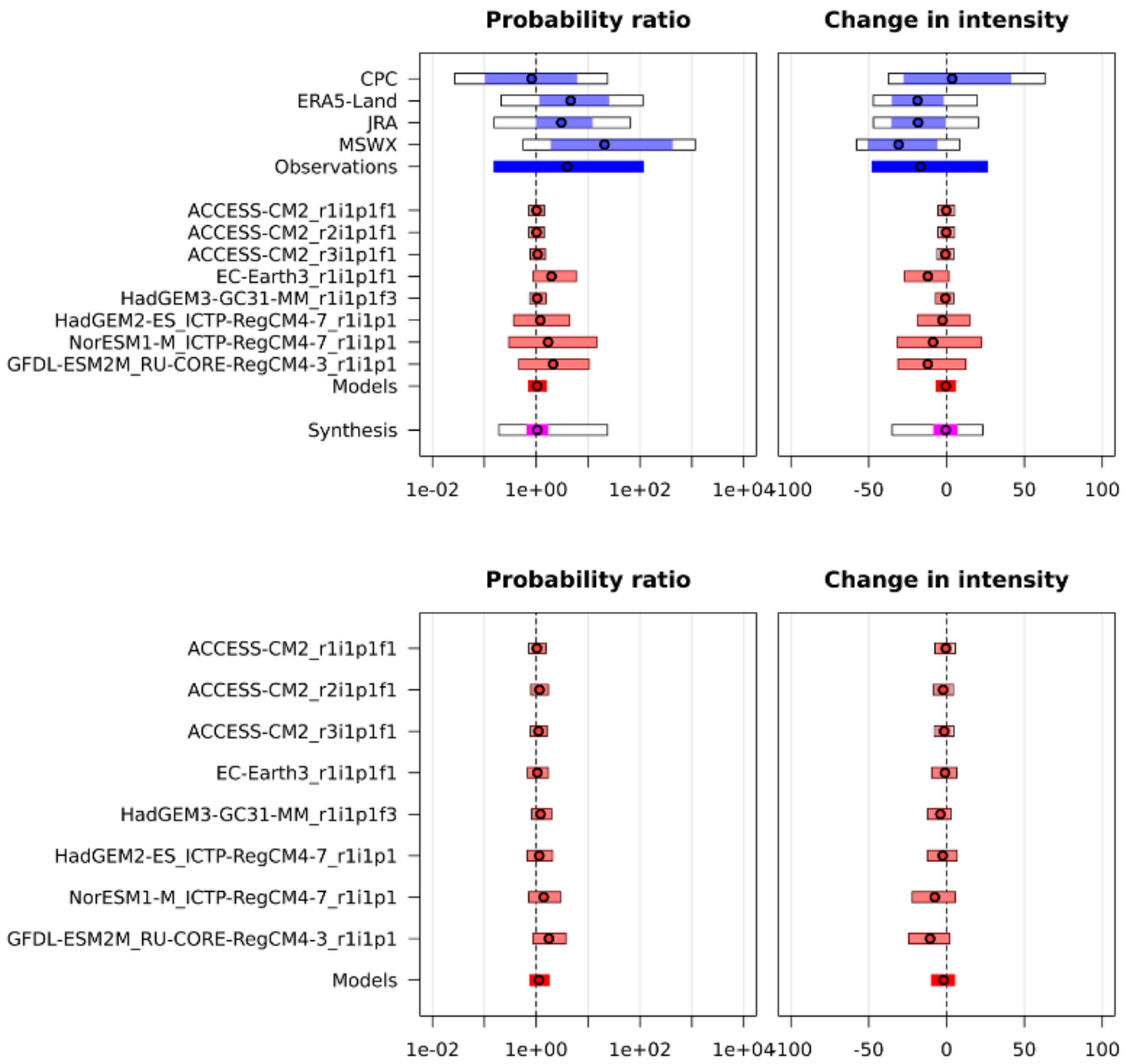


Figure 3.3: *Synthesised changes for the 20-year July-October seasonal low precipitation event in the study region due to GMST. Probability ratio (left) and changes in intensity in % (right) are shown for a historical period comparing the past 1.4°C cooler climate with the present (top row) and for a future period, based on model projections only, comparing the present and a 2.8 °C warmed climate (bottom row).*

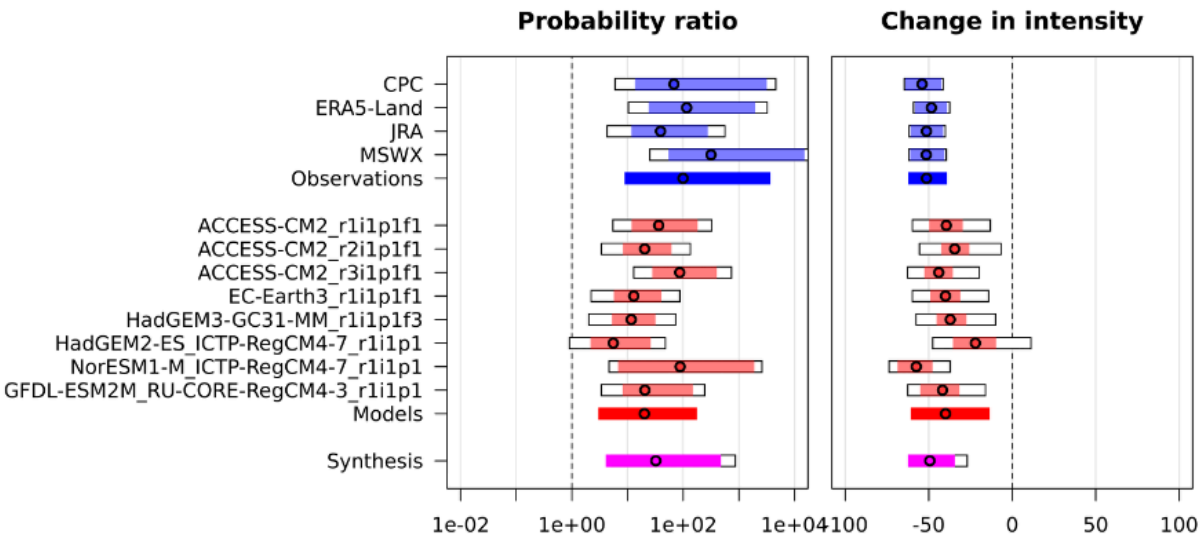


Figure 3.4: *Synthesised changes for a 20-year July-October low precipitation event in the study region due to ENSO. PR (left) and change in intensity in % (right) are shown for the current vs neutral RONI ASO states.*

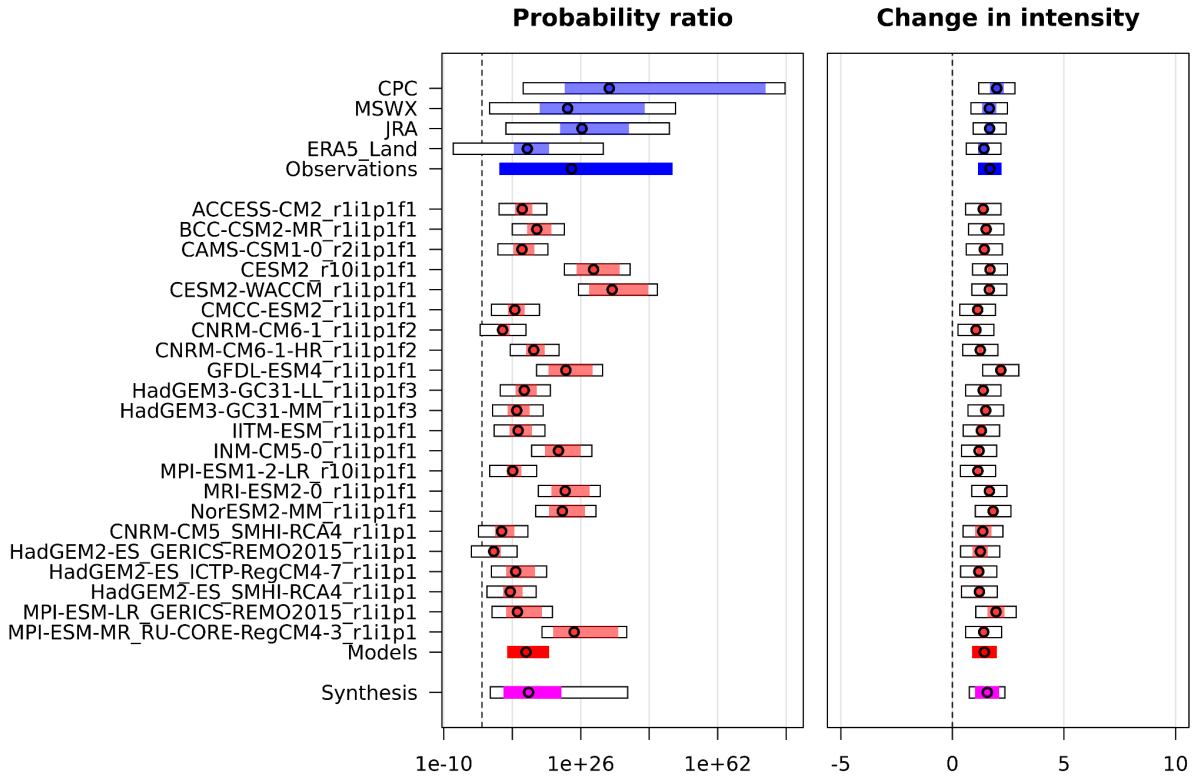
Data	**Influence of GMST increase of 1.4°C**			**Influence of El Niño**	
	Time period	**Probability ratio (95% CI)**	**Intensity change (95% CI)**	**Probability ratio (95% CI)**	**Intensity change (95% CI)**
Observations	**Preindustrial - present**	3.92 (0.19, 91.86)	-16.96 (-44.35, 22.70)	**99.40 (11.48, 2831.93)**	**-51.36 (-58.56, -42.99)**
Models		1.04 (0.90, 1.23)	-0.60 (-3.48, 2.12)	**20.09 (3.86, 136.81)**	**-39.96 (-56.89, -17.14)**
Synthesis		1.04 (0.85, 1.32)	-0.70 (-4.67, 3.22)	**32.23 (5.25, 366.30)**	**-49.35 (-58.72, -38.08)**
Models	**Present - future**	1.12 (0.94, 1.39)	-2.00 (-6.38, 1.73)		

Table 3.2: *Summary of results for July-October low precipitation event presented in Figs 3.3 & 3.4: changes due to GMST include past-present changes and present-future changes for the RONI ASO state of 2026, changes due to RONI ASO include El Niño versus neutral in the present climate. Statistically significant changes are highlighted in* ***bold*** *font.*

3.2.3 Temperature

For seasonal (ASO) mean temperature, the observations and climate models are found to be consistent, and in line with the expectation due to global warming. The PR from observations, climate models and from combining observations and models, all tend to infinity, indicating that seasonal temperatures with a 20-year return period in today's climate would have been virtually impossible in the pre-industrial climate; in other words climate change has made 2026 seasonal temperatures

virtually certain, and about 1.6C hotter as compared to 1-in-20-year ASO seasonal temperatures in the pre-industrial climate. This trend is projected to continue if global warming levels continue to increase, with another 1.4 time increase in likelihood and an additional 1.4C increase in the seasonal temperatures of a 1-in-20 year rarity in a future warmer world that is 2.8C warmer than pre-industrial levels, as compared to today's climate. Comparison between the current ENSO levels (characterised by RONI ASO) in the observations and models suggest that the current ENSo levels have made this season warmer as compared to seasonal temperatures of similar rarity under neutral conditions. The synthesised results from combining the observations with the climate models suggest a 11-time increase in the likelihood and ~0.3C increase in the magnitude of ASO seasonal temperature in the region due to 2026 ENSO conditions, as compared to neutral ENSO conditions, albeit with uncertainty ranges encompassing no change (Table 3.3).



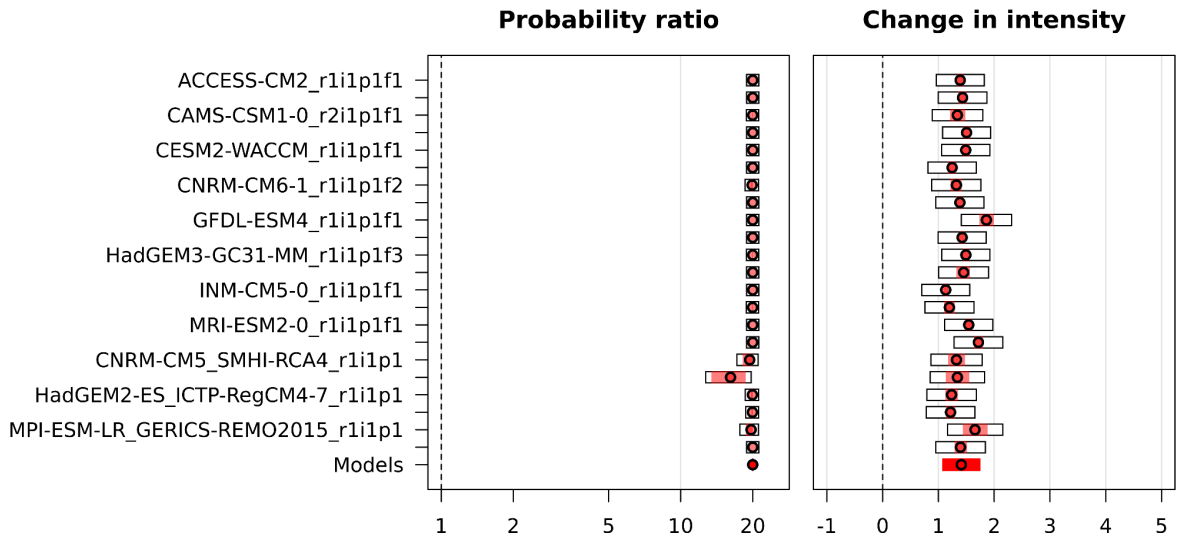


Figure 3.5: *Synthesised changes for the 20-year August-October (ASO) mean seasonal temperature in the western Indonesian study region due to GMST. Probability ratio (left) and changes in intensity (right) are shown for a historical period comparing the past 1.4°C cooler climate with the present (top row) and for a future period, based on model projections only, comparing the present and a 2.8 °C warmed climate (bottom row)*

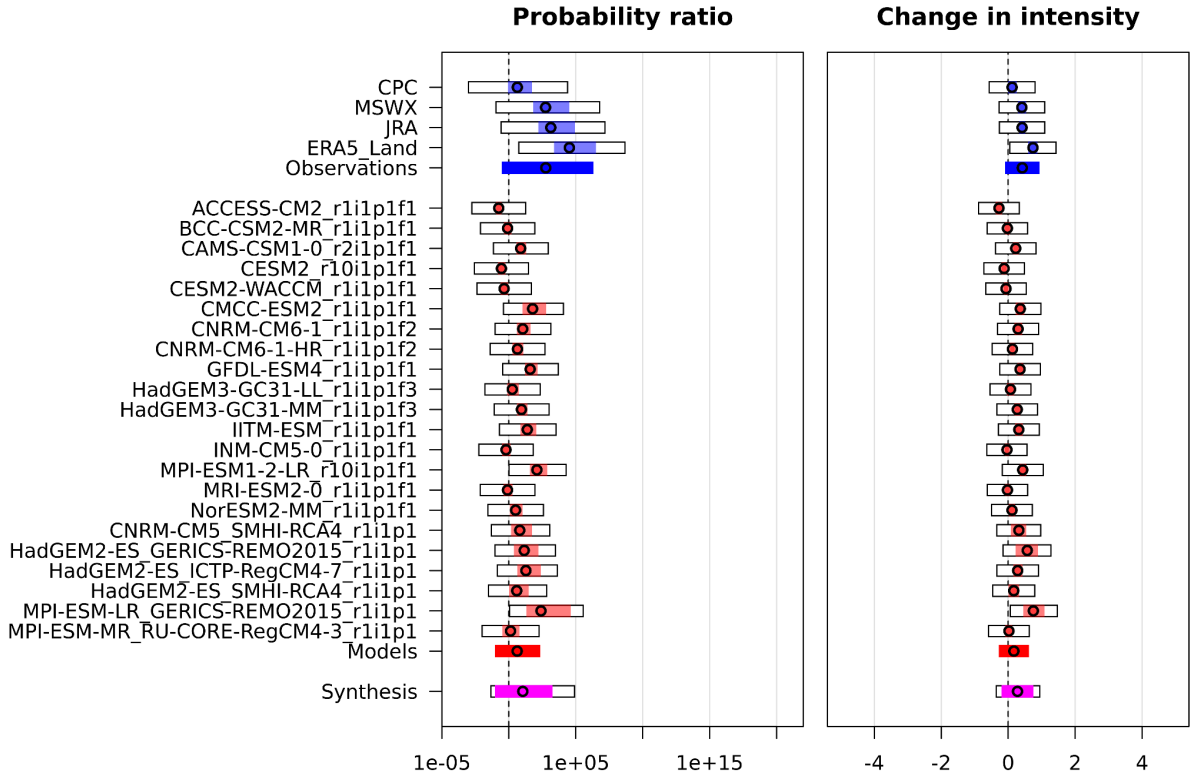


Figure 3.6: *Synthesised changes for a 20-year August-October (ASO) mean temperature in the study region due to ENSO. PR (left) and change in intensity (right) are shown for the current vs neutral RONI ASO states.*

Data	Influence of GMST increase of 1.4°C			Influence of El Niño	
	Time period	Probability ratio (95% CI)	Intensity change (95% CI)	Probability ratio (95% CI)	Intensity change (95% CI)
Observations	**Preindustrial - present**	**inf (4.0 × 10^4, inf)**	**1.68 (1.15,2.21)**	576.53 (0.30,21e+6)	0.42 (-0.09, 0.93)
Models		**inf (inf, inf)**	**1.43 (0.88,1.99)**	4.23 (0.09, 228.01)	0.17 (-0.28, 0.62)
Synthesis		**inf (4.8 × 10^5, inf)**	**1.56 (1.02,2.10)**	11.09 (0.09, 1817.27)	0.28 (-0.20, 0.76)
Models	**Present - future**	**event becomes near certain**	**1.41 (1.07,1.75)**		

Table 3.3: *Summary of results for Aug-Oct average temperature presented in Figs 3.5 & 3.6: changes due to GMST include past-present changes and present-future changes for the ENSO ASO state of 2026, changes due to ENSO ASO include El Niño versus neutral in the present climate. Statistically significant changes are highlighted in* ***bold*** *font*

3.3 Conclusions hazard

In this analysis, we assess the influence of climate change as well as ENSO on the likelihood and magnitude of the key meteorological drivers of forest and peatland fires in western Indonesia. We focus on three variables: (i) low seasonal rainfall during July–October, representing (lack of) moisture availability during the fire season, (ii) mean seasonal temperature during the peak fire season during August–October, to capture the warm conditions that contribute to the drying and, (iii) the maximum 7-day mean vapour pressure deficit (VPD) during August-October season, which captures episodes of high atmospheric drying demand that rapidly dry vegetation, making conditions more conducive to fire ignition and spread.

Seasonal rainfall in the study region is subject to high year-to-year variability, primarily due to ENSO. Our analysis finds that JASO rainfall in western Indonesia is strongly associated with ENSO, with seasonal rainfall tending to be more during the negative phase of ENSO (La Nina) and approaching drought conditions as ENSO phase becomes positive (El Niño). Consequently, the long-term trends associated with global warming (if any) are not emergent over natural variability in one of the observed datasets and most of the climate models. The observations suggest an overall 15% reduction in JASO rainfall amounts associated with a 1-in-20 year event in today's climate as compared to a 1.4°C cooler pre-industrial climate. However, the synthesised results from combining observations with the climate models do not reflect this increase with best estimates close to no change and uncertainties encompassing no change. For ENSO, the observations and climate models are consistent, although the models suggest a slightly more modest decrease in 1-in-20 year JASO precipitation events under the 2026 prevailing El Niño conditions as compared to neutral conditions. The synthesised results suggest a 50% decrease in the JASO seasonal rainfall amounts is attributable to 2026 El Niño as compared to neutral conditions.

For seasonal (ASO) mean temperature, the observations and climate model simulations show consistent results, in line with the expected response to anthropogenic global warming. The probability ratios (PRs) estimated from observations, climate models, and their synthesis all tend

towards infinity (with estimated numbers very high by several orders of magnitude), human-induced climate change has made such temperatures virtually certain in today's climate, and about 1.5°C hotter. However, ENSO has a less pronounced effect on seasonal temperatures, with synthesised estimates from observations and climate models suggesting an 11-time increase in the likelihood of such temperatures along with a 0.3°C increase in the intensity.

For VPD7x, both observations and climate models agree that both human-induced climate change and the 2026 El Niño have increased the likelihood and the magnitude of high VPD7x extremes, although climate models show smaller changes than observations. Synthesising observations and climate models, climate change is found to have made such conditions as observed this year around 3 times more likely and more intense by 0.43kPa. The ongoing El Niño also increased the likelihood of these conditions by approximately 5 times, with VPD intensity increasing by around 0.57 kPa.

4 Vulnerability and exposure

At the time of writing, Indonesia is experiencing a severe and prolonged fire season in 2026, with activity increasing from July and continuing into November. In Indonesia the peak fire season typically lasts around 14 weeks, starting from early August. In 2026 there have been 21,132 Visible Infrared Imaging Radiometer Suite (VIIRS) fire alerts reported so far in Indonesia (considering only high confidence alerts). This total is high compared to the total for previous years going back to 2012.

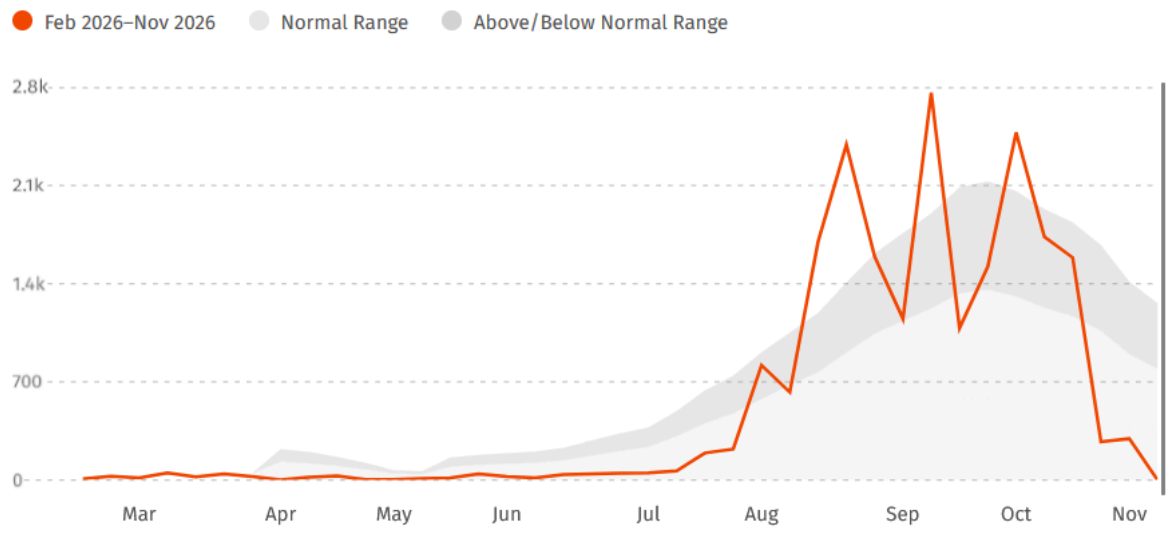


Figure 4.1: *Detection of VIIRS fire alerts in 2026 in Indonesia (orange line) compared to historic fire data since 2012. There have been 21,132 VIIRS fire alerts reported so far in Indonesia (considering only high confidence alerts). Source: Global NatureWatch 2026.*

Fires are concentrated across Sumatra and Kalimantan (Indonesian Borneo), particularly South Sumatra and Central and West Kalimantan, while parts of Java and Papua, notably South Papua, are also experiencing extensive burning (BBC, 2026).

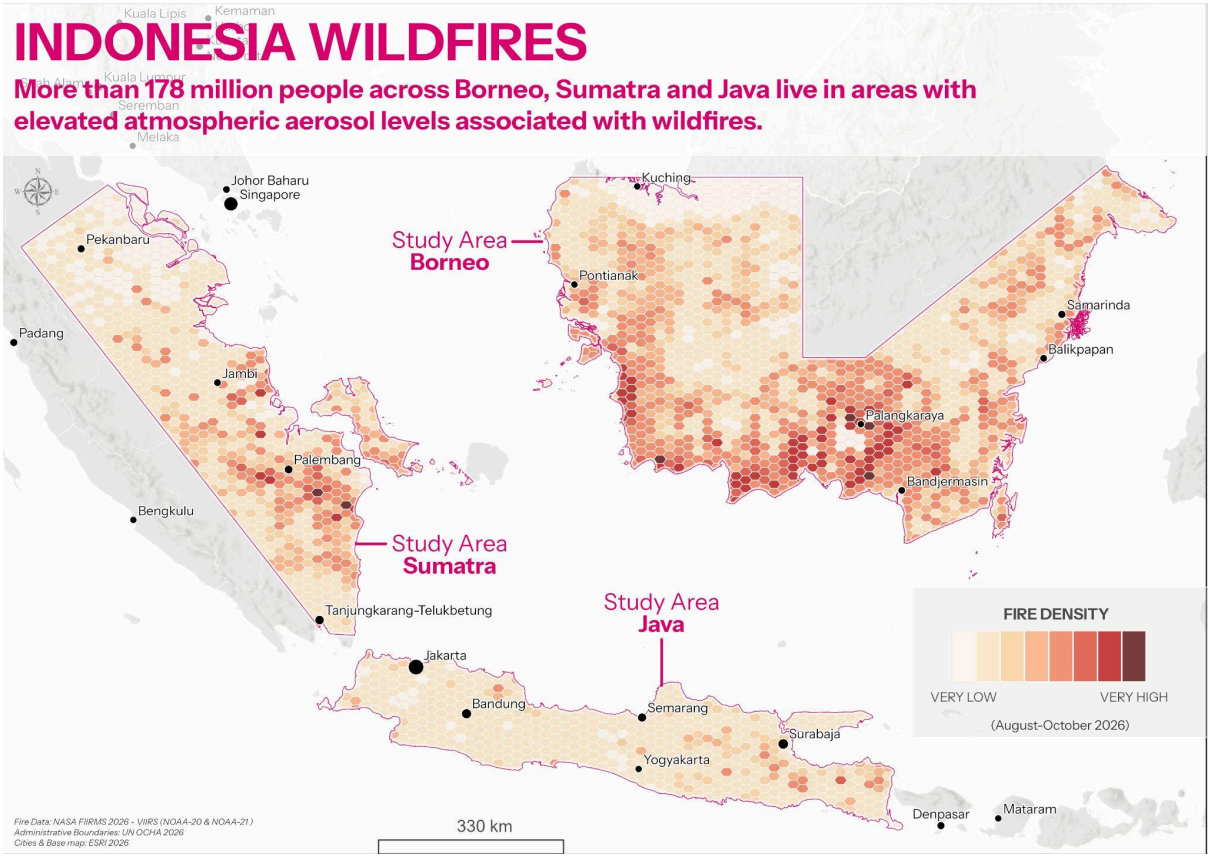


Figure 4.2: *Spatial density of active fire detections across Indonesia (01/08/2026 - 31/10/2026), based on medium- and high-confidence VIIRS observations from NOAA-20 and NOAA-21, with potential duplicates removed. The highest concentrations occurred in central and southern Kalimantan, central and eastern Sumatra, and eastern Java. Source: Climate Centre 2026.*

By September 2026, approximately 1,9 million hectares had burned nationwide, making 2026 one of Indonesia's worst fire seasons since 2015 (Nusantaras Atlas, 2026) – when one of the country's worst fire seasons on record burnt 2,6 million hectares and exposed 43 million people to hazardous smoke, killing 19 while half a million people suffered respiratory illnesses (NASA, 2015; World Bank, 2016).

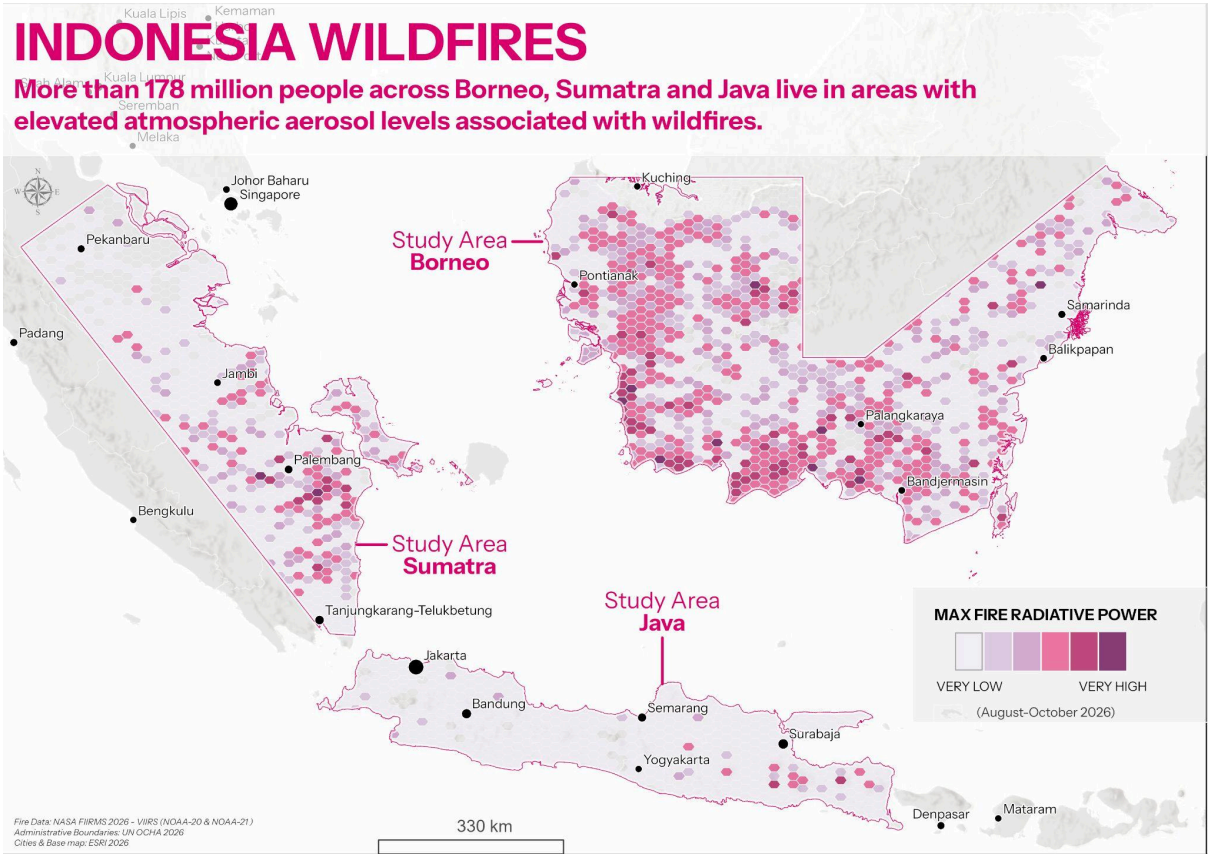


Figure 4.3: *Maximum Fire Radiative Power (FRP) across Indonesia 01/08/2026 - 31/10/2026), based on medium- and high-confidence VIIRS observations from NOAA-20 and NOAA-21, with potential duplicates removed. FRP measures the rate of energy radiated by fires (MW). The map shows the highest recorded FRP per grid cell, highlighting the strongest observed fire activity, which does not necessarily coincide with areas of highest fire density. Source: Climate Centre 2026.*

In 2026, fires have been affecting peatlands particularly persistently, while widespread smoke has substantially reduced air quality and visibility, causing a public health emergency (MDMC, 2026). The Ministry of Health Republic of Indonesia reported a cumulative total of over 400,000 respiratory infections associated with the fires, with an estimated 12.5 million people exposed to haze across Indonesia, Malaysia, Singapore, and Timor-Leste (Antara, 2026; BBC, 2026; The Straits Times, 2026).

Research from Indonesia shows that peatland fires can have ecological consequences lasting years to decades. In Central Kalimantan, burned forests experienced substantial losses of canopy cover, tree density and biodiversity, with limited structural recovery after 12 years (Harrison et al., 2023). Repeated fires further hinder vegetation recovery, favoring shrubs and ferns over forest regeneration (Setiawan et al., 2025). Fires and haze have also been linked to prolonged food scarcity and behavioral changes among Bornean orangutans (Ashbury et al., 2022). The destruction of forest has widely impacted the orangutan populations by threatening their natural habitats, restricting their movement and limiting access to food and other resources. The increasing fires had also forced the critically endangered apes to flee into agricultural plantations and human settlements increasing human-wildlife conflict risks. In response, the Indonesian authorities rescued 46 orangutans from the fire affected areas in August and September (BBC, 2026; Lotulung, 2026). Other associated

socio-economic impacts for communities from the fires also include compromised water quality, disrupting commercially important fish populations, which declined sharply within three months after major fires (Harrison et al., 2023). Critically, peatland fires release carbon stored for thousands of years and trigger continued CO2 emissions through peat decomposition, contributing to global warming long after the fires have been extinguished (Koarashi et al., 2026).

The severity of a disaster depends not only on the hazard itself, but also on who and what is exposed, underlying vulnerabilities, and the capacity to prepare for and respond to its impacts. In light of this, the following chapter explores the environmental, socioeconomic and institutional factors that play a role in the spread of the 2026 fires and their impacts, including land use practices, population exposure, fire risk management, and public health protection.

4.1 Landscape, land use, and fuel availability

Deforestation and logging in tropical forests and agricultural expansion have increased fuel availability and reduced humid tropical forest cover in Indonesia (Nikonovas et al., 2020). Draining of peatlands, e.g. in Borneo (Shiraishi et al., 2023) and Sumatra (Agustiyara et al., 2026) to convert to agricultural land, further increases fire susceptibility by exposing carbon-rich peat to drying and combustion. Such drained peatlands are highly susceptible to fire, exposing carbon-rich peat to prolonged underground combustion (Horton et al., 2021). Salmayenti et al. (2025) found that drained peatland had a 13 times larger annual mean density of fire hotspots compared to undrained peatlands. The resulting peat fires can release substantial amounts of stored carbon into the atmosphere, with Indonesia's 2026 wildfire emitting an estimated 195.67 million tonnes of carbon by early November, contributing significantly to global wildfire emissions (SCMP, 2026).

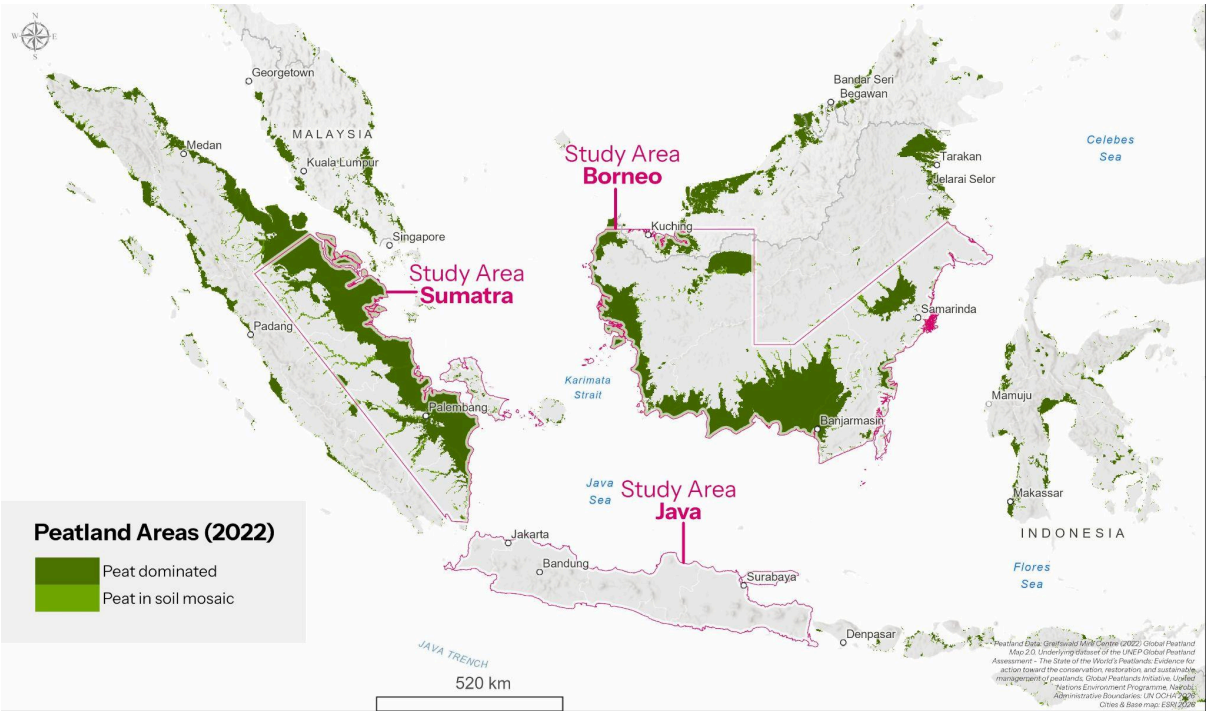


Figure 4.4: *Peatland Areas (2022): This map shows the distribution of natural peatland areas (Peat dominated & Peat in soil mosaic) across Indonesia. Comparing peatland areas with the active fire*

areas of 2026 shows a strong spatial overlay especially in southern Borneo and eastern Sumatra. Peatland data was derived from the Global Peatland Map. Source: Climate Centre 2026.

In the past decades there has been a substantial decline in the peat swamp forests, driven primarily by plantation and smallholder agriculture (mainly for oil palm and industrial forestry) as well as logging. For Borneo, the spatial extent was estimated to be 4.9 million hectares in 1990, dropping to 3.6 million in 2000 and 2.7 million in 2010 as reported by the United Nations Environment Programme (2022) based on the work by Miettinen et al. (2012). An even larger reduction of peat swamp forest area is reported for Sumatra from 4.9 (1990), to 3.1 (2000) and 1.8 million ha (2010) in the same assessment report (UNEP, 2022).

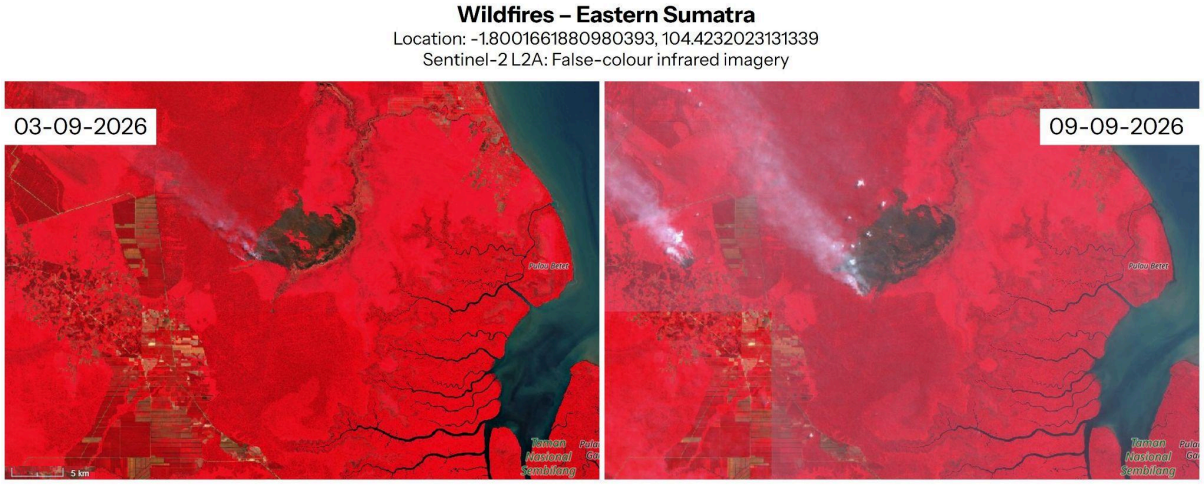


Figure 4.5: *False-color infrared satellite imagery showing wildfire impacts in eastern Sumatra, six days apart. Healthy vegetation appears red, burned areas dark brown or black, and smoke white. The images show fire spreading south and west, as well as the emergence of a second fire to the west. Source: Copernicus 2026.*

More recent data on land-use change is available from Lestari et al. (2023), who estimate that Indonesia had a total forest cover in peatlands of 6.5 million ha in 2009, from which 1.4 million ha was deforested a decade later, reducing the remaining forest cover to 5.1 million ha in 2019. Since then, forest and peatland in Kalimantan and Sumatra have mainly been converted to oil palm, pulpwood plantations, and mining, with Kalimantan alone reportedly losing 129,896 hectares in 2024 (Mongabay, 2025).

4.2 Agricultural practices and socioeconomic drivers of ignition

Fires in Indonesian lowland forests are primarily human-ignited, and droughts or prolonged dry weather create conditions for fire to spread (Balboni et al., 2025; Ramdani et al., 2026; Widayati et al., 2026). The fire originates mainly from local slash-and-burn farming for rice cultivation; however, the burned land is eventually turned into smallholder oil palm plantations (Ramdani et al., 2026). The Indonesian Forum for the Environment (WALHI) found that 74% of Kalimantan's January-July, 2026 hotspots (25,524 of 34,262 hectares) fell within oil palm, mining, and forestry permits (detik Kalimantan, 2026). Communities set fires to manage land, but plantations and drained peat leave

drier, more flammable ground, along with drought conditions that can lead fires to spread out of control (Salmayenti et al., 2025).

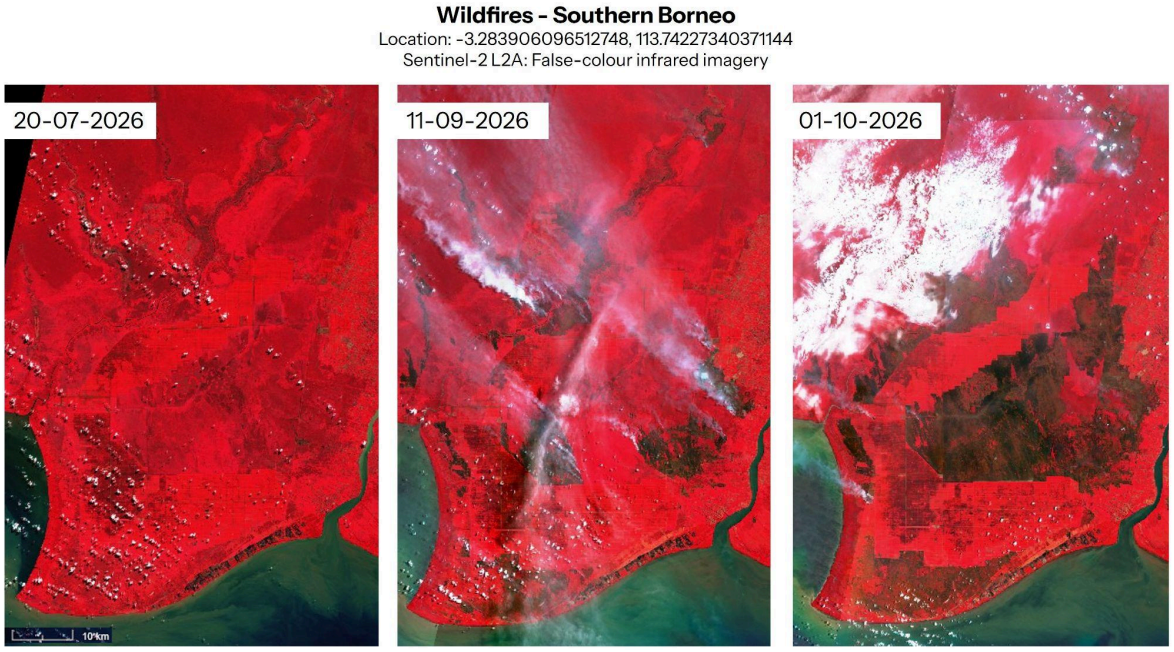


Figure 4.6: *False-color infrared satellite imagery showing wildfire impacts in southern Borneo before, during, and after the fires. Health vegetation appears red, burned areas in dark brown or black, and either clouds or smoke in white. The images show undamaged vegetation before the fire season, multiple ongoing fires in September, and the extent of fire damage by October. Source: Copernicus 2026.*

Farmers follow this practice because it is cheap, as mechanical land clearing costs around US$300–450 per hectare in West Kalimantan (Ramdani et al., 2026; Widayati et al., 2026). Although this has not been independently verified during the 2026 season, government officials suspect some fires were set deliberately because land in West Kalimantan was already being prepared for oil palm cultivation (The Straits Times, 2026). In parts of the region, oil palm cultivation has reduced poverty and boosted local government revenue, public spending and the provision of public goods, but also contributed to greater deforestation, forest fires, certain health issues and conflict showcasing the tradeoffs of the practice (Edwards, 2026). Stakeholders in Ketapang have pointed out that zero-burning practices will be possible if farmers are incentivised and have access to suitable alternatives (Widayati et al., 2026). Burning is also linked to cultural practices and laws. The Dayak Ma'anyan indigenous people of central Kalimantan see it as connecting humans, plants, animals, ancestors, seasons, fire, and the land, beyond the livelihood source. Law 32/2009 allows households to burn up to 2 ha for local varieties within firebreaks (Katadata, 2026), but this was suspended in September amid the extreme El Niño period (INP, 2026a).

The key actors liable for fires under their permits are predominantly concession holders, smallholders, and communities (Wicaksono and Nafu, 2026; Ramdani et al., 2026). However, research by Purnomo et al. (2017) from Riau Province in Sumatra highlights the involvement of wider networks of actors who benefit economically from burning, including farmer group organizers who facilitate land clearing and exert influence through patronage networks. Weak property rights propel firms to use fire

more often when the risk is spread across state forest rather than a neighbour's concession, accounting for 28% of fires for this cause (Balboni et al., 2025). The zoning systems are also very unclear. In one Ketapang landscape, 75% of the protected peat domes are zoned for cultivation (Widayati et al., 2026). In Merauke food estate zones overlap with Indigenous Papuan customary land (EPN, 2026). There are also international drivers at play with Western consumption patterns having an influence on Indonesia's land use. However, a ban on high deforestation palm oil in the EU would have reduced the deforestation rate by just 1.6%, as 52% of the trade would have gone to other buyers. Hence, coordination with the major consumer markets and support for better forest governance in Indonesia are key (Busch et al., 2022).

4.3 Population exposure and health

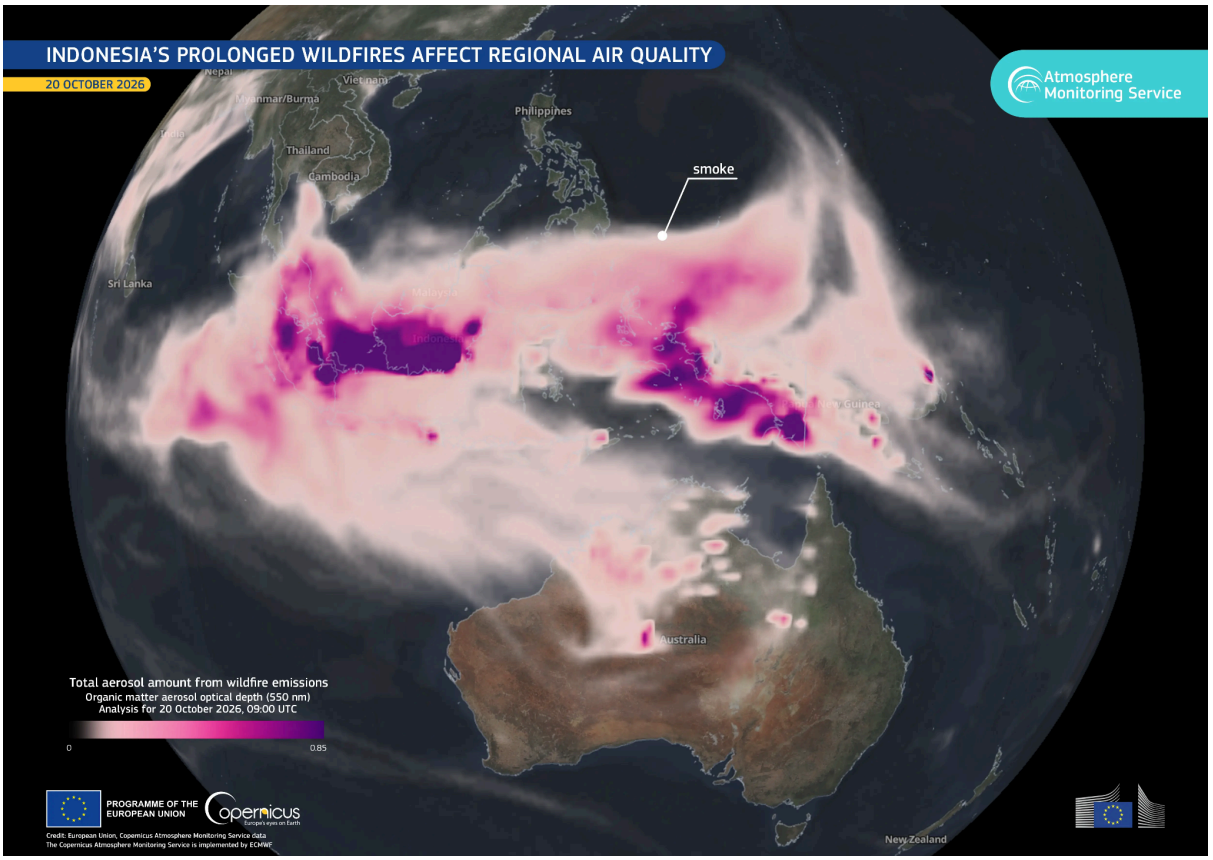


Figure 4.7: *smoke transport from wildfires across the Maritime Continent on 20th October 2026. The left region corresponds to the areas considered in this study. Source: Copernicus (2026).*

Indonesia is experiencing its most severe fire and haze seasons in over a decade, with widespread deterioration in air quality, although smoke pollution has generally remained below the extreme levels recorded during the 2015 crisis. The impacts of the 2026 wildfires have extended well beyond the areas directly affected by the flames, generating significant transboundary consequences. Smoke and harmful pollutants released from burning forests, swamps and peatlands have travelled national borders resulting in haze, containing fine particulate matter and carbon monoxide to neighbouring countries like Singapore, Malaysia and Philippines (Figure 4.1) resulting in severe public health concerns (BBC, 2026).

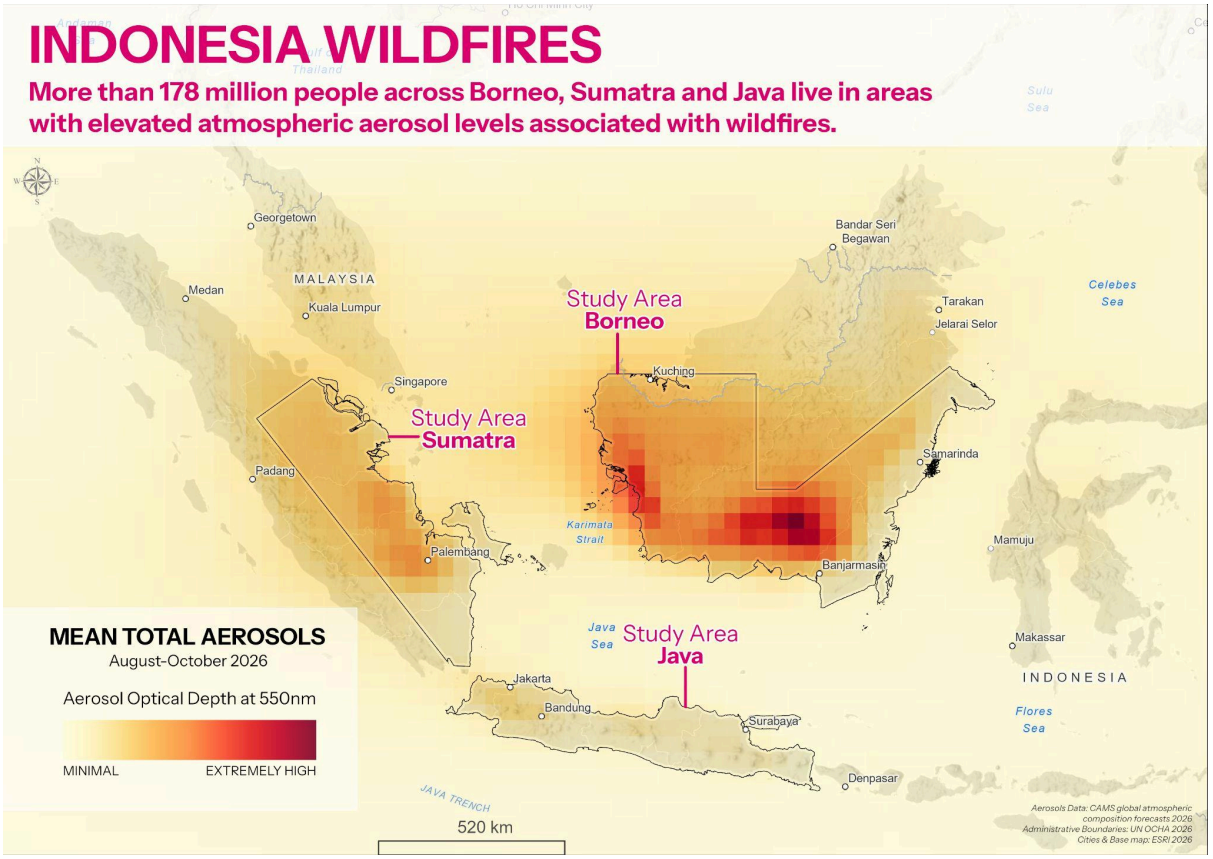


Figure 4.8: *Mean Aerosol Optical Depth (AOD) across Indonesia (01/08/2026 - 31/10/2026), based on Copernicus Atmosphere Monitoring Service (CAMS) data at 550nm. The highest mean aerosol levels were concentrated in southern and western Borneo, eastern Sumatra and western Java, which also recorded the highest levels globally during this period. Source: Climate Centre 2026.*

Indonesia's air pollution index recorded exceptionally high readings in parts of Borneo and Sumatra with levels exceeding 1,000, far surpassing the threshold of 300 at which air quality is classified as hazardous (Good Air, 2026). Singapore recorded a one-hour PM2.5 concentration of 288 micrograms per cubic metre in the western part of the island in October, pushing air quality into the National Environment Agency's "very high" pollution category (CNA, 2026). Similarly, on 8-9 October, severe haze briefly made Kuala Lumpur the world's most polluted major city, with local AQI readings reaching 203, prompting widespread school closures across several Malaysian states (AQ Air, 2026).

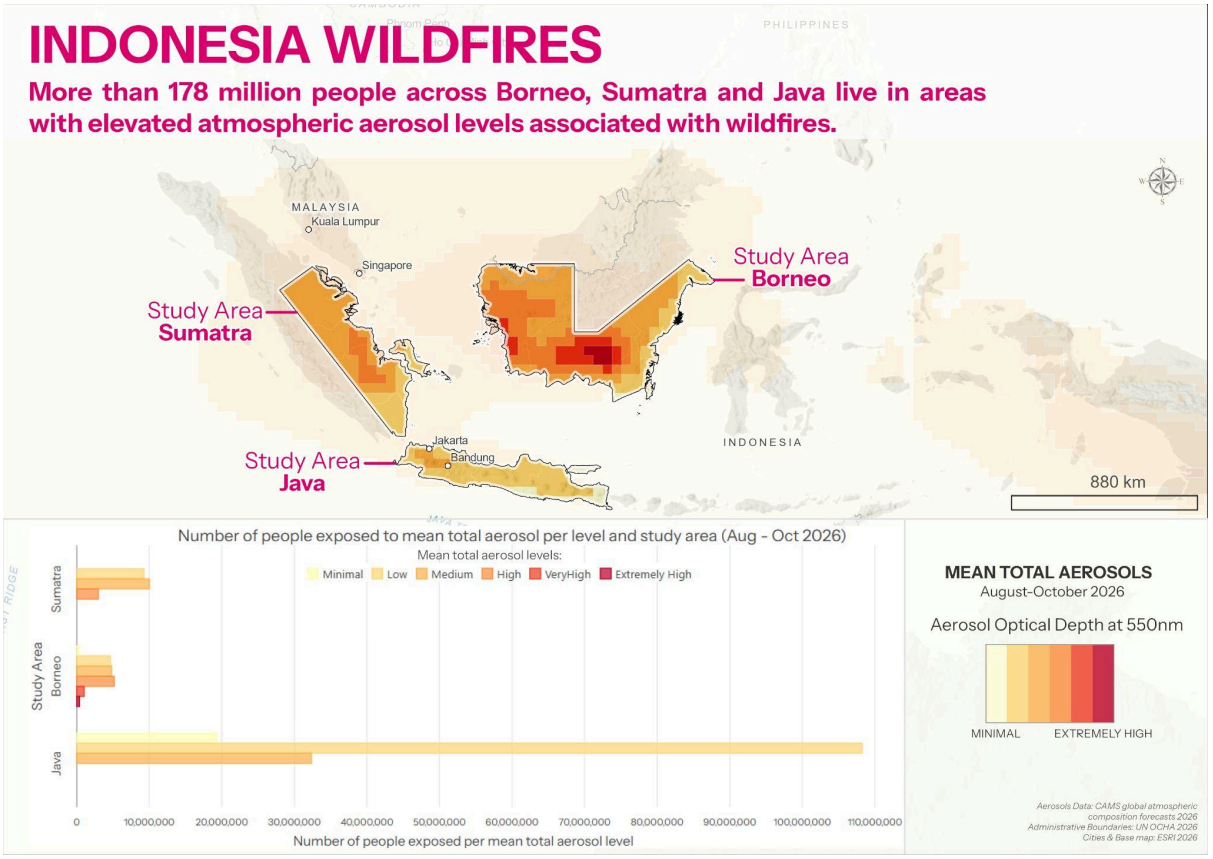


Figure 4.9: *Estimated population exposure to atmospheric aerosols (01/08/2026 - 31/10/2026), based on mean AOD from CAMPS and 2026 WorldPop population data. An estimated total 178,963,787 people live in assessed areas with elevated aerosol levels (≥0.5 AOD).*

Exposure to wildfire smoke can aggravate existing health conditions, while sustained exposure could contribute to development of new respiratory health impacts like exacerbation or onset of asthma, chronic obstructive pulmonary disease (COPD), bronchitis and pneumonia with pronounced impact on vulnerable groups like individuals with pre-existing respiratory or cardiovascular conditions, middle aged or older adults, pregnant women and developing foetuses (Rizzo & Rizzo, 2024). Beyond these respiratory complications, long lasting consequences like increased strain on fragile healthcare systems, disruptive access to health services and psychological trauma could further compound the vulnerabilities of affected populations (Ye et al., 2026).

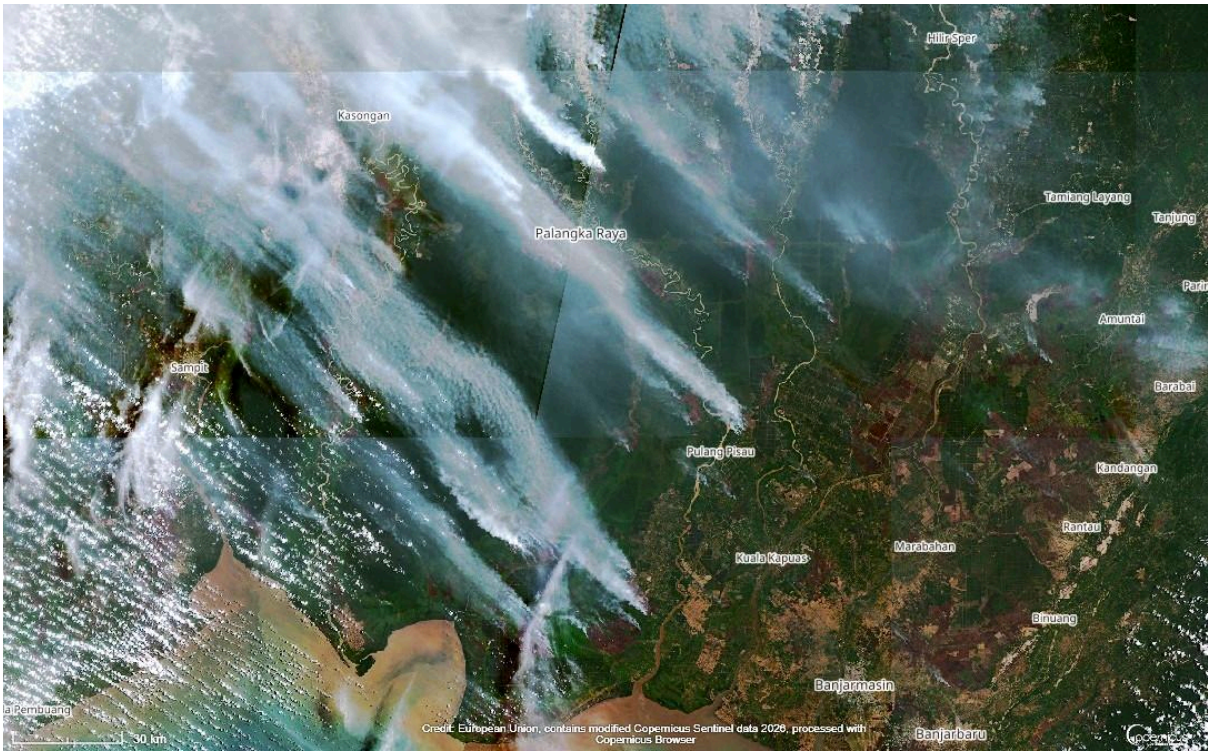


Figure 4.10: *Satellite imagery of active fires and smoke plumes in southern Borneo: This satellite imagery (Sentinel 2 L2A - Highlight Optimized Natural Color) was captured on 11-09-2026, showing multiple large active fire in agricultural areas west of Banjarmasin in southern Borneo. Large smoke plumes are visible, extending to north-west and exposing people living in those areas to high levels of atmospheric aerosols. Imagery Source: Copernicus 2026.*

In mid-October, Indonesia's Health Ministry had recorded more than 330,000 cases of people suffering from chronic coughs and acute respiratory infections, with more than 62,000 affected were infants and toddlers under the age of five (BBC, 2026). Children are particularly susceptible to the harmful effects of wildfire smoke because their lungs are still developing and their narrower airways make them more prone to inflammation and obstruction from mucus and inhaled particles (WHO, 2026). They also breathe more rapidly than adults, meaning they inhale a greater volume of air relative to their body weight and, consequently, may absorb higher concentrations of pollutants. Their frequent engagement in outdoor activities and still-developing immune systems further increase their exposure and vulnerability (WHO, 2026). Prolonged or repeated exposure to wildfire smoke can interfere with normal lung development, impair respiratory function and increase the risk of developing chronic respiratory conditions later in life (Antara, 2026). The conditions are further aggravated by the haze and smoke from peat fires that contain a complex mixture of pollutants and microparticles that can penetrate deep into the lungs and even the bloodstream, causing inflammation, chronic lung diseases and increased risk of premature deaths (Antara, 2026).

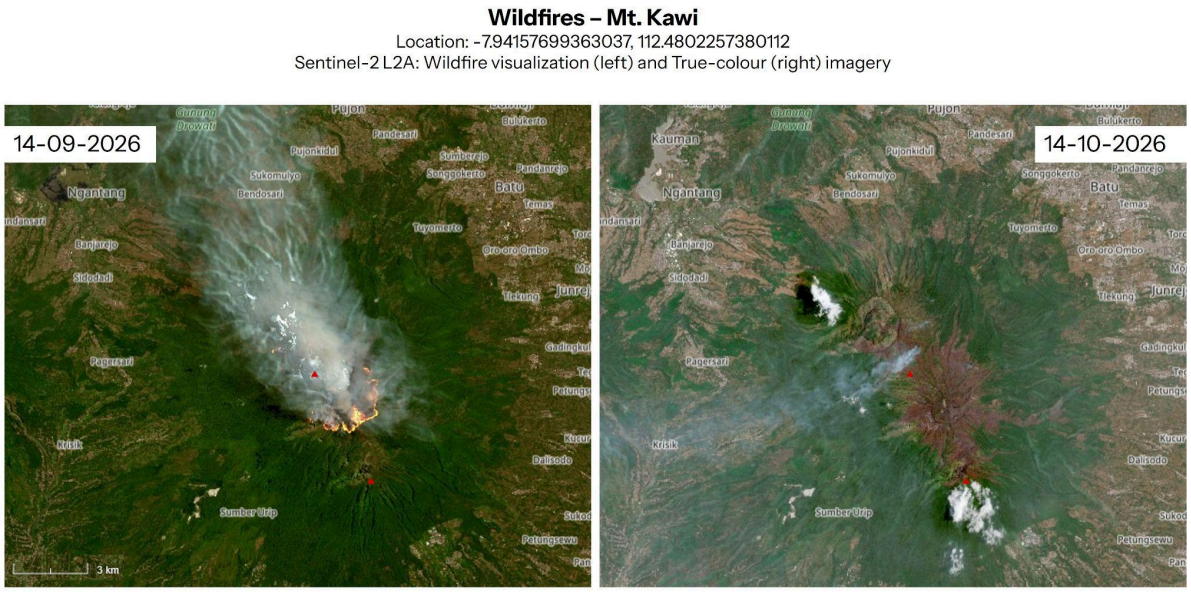


Figure 4.11: *Satellite imagery of active fires and smoke plume at Mount Kawi in eastern Java: The imagery on the left (wildfire visualization) was captured on 14. September 2026 and shows a large active wildfire in the nature area of Mount Kawi in eastern Java. The large smoke plume extends to populated areas in the surrounding. The right imagery (True-colour) was captured in 14. October 2026 and shows large burnt areas which used to be covered in healthy vegetation before the wild fire. Imagery Source: Copernicus 2026.*

Along with children, older adults and pregnant women are particularly vulnerable as longer exposure to harmful pollutants can increase risks of severe illnesses and aggravate existing conditions. Furthermore, a study by CREA (2026) found that air pollution related deaths in Indonesia surged 42% from August to September 2026, primarily driven by forest and land fires which led to 3,560 deaths in September. With over 58 million people exposed to “hazardous” air, the study further pointed out that an average of 34.5 million people in Indonesia breathed polluted air every day in September, up by nearly 60% from August 2026 (CREA, 2026). These cascading and compounding impacts have been further exacerbating pre-existing vulnerabilities, contributing to increased morbidity and mortality among at-risk populations, particularly those with limited resources and lower adaptive capacity. For example, between 1 July and 22 October, an analysis by Carbon Spur estimates that the transboundary haze has contributed to about 1,700 premature deaths across Malaysia (Malay Mail, 2026).

4.3.1 Health system response

Schools transitioned to remote modality where ISPU passed 200, and by early September approximately 1.4 million students from six provinces were attending school from home (Reuters, 2026a), while authorities and Save the Children distributed thousands of masks and issued advisories to limit exposure (MoE, 2026; Save the Children, 2026; ANTARA, 2026). The Ombudsman reported variations in mask distribution and educational responses across affected areas, with some local governments introducing remote learning while others maintained in-person schooling, particularly outside provincial and district capitals (Kompas, 2026). Further, about 2 million students across Malaysia have been affected by school closures (The Business Times, 2026).

By 22 October, authorities had mobilized over 1,600 primary healthcare centres, 360 referral hospitals, and 491 oxygen facilities across Riau, Jambi, South Sumatra, and South, West and Central Kalimantan (RRI, 2026). By late October, daily reported ARI had dropped from approximately 10,000-15,000 in early September to about 3,000 cases per day (ANTARA, 2026). Meanwhile, the Ombudsman reported that dedicated healthcare arrangements for smoke-affected patients and proactive outreach to vulnerable groups were not consistently implemented, while specific health response measures were documented in Jambi, Maluku, North Maluku, and West Kalimantan (Kompas, 2026). Further, the Ombudsman highlighted that some local disaster responses depended heavily on central government intervention, potentially delaying response efforts and complicating coordination (Kompas, 2026).

The health-related labor force grew to thousands of health workers who distributed millions of masks and managed oxygen rooms in community health centers as the number of respiratory infections passed 300,000 (RRI, 2026). Smoke and haze were especially difficult to address. During wildfire and toxic haze events, households employ positive coping strategies such as using indoor air purifiers, wearing face masks, staying indoors, and forming community volunteer fire brigades , while negative coping strategies include using open fire for household waste management and relying on inadequate cloth coverings (CREA, 2026). In a 2023 study, in rural Central Kalimantan, indoor PM 2.5 was found to mirror outdoor levels almost exactly, given the housing stock could not keep smoke out (Graham et al., 2024). In the 2026 fires, the largest evacuation effort was driven by the threat of the fire itself, not of smoke, despite the prevalence of smoke and its potential to infiltrate housing. This evacuation was precipitated by 305 homes burning, and involved about 500 people moving to a school and mosque in South Bangka (Reuters, 2026b). Both Malaysia and Timor-Leste closed their schools, while Singapore restarted haze subsidies to support outpatient haze-related medical treatment, last used in 2015 (AFP, 2026a, 2026b; Mothership, 2026). In Malaysia, the National Disaster Management Agency (NADMA), in collaboration with state civil defense actors, distributed more than 2 million masks to low-income households, essential staff and outdoor workers (Straits Times, 2026).

4.4 Wildfire governance and prevention

The Presidential Instruction No. 3 of 2020 established the current national strategy for forestry and land fire management in Indonesia, focusing on prevention, cross-agency coordination and law enforcement, and post-fire land restoration (UNEP, 2020). These instructions, amongst other frameworks, form the legal backbone of the Forest and Land Fire Management Coordination Desk, the intra institutional coordination body for fire management (RFMRC-SEA, 2025). The Desk operates under the Coordinating Ministry of Political and Security Affairs which guides high-level national policy direction. The Desk works on an ad-hoc basis and was reactivated in June 2026 to address the threat of the El Niño phenomenon after it was disbanded at the end of the 2025 dry season (Antara, 2026).

The National Disaster Mitigation Agency (BNPB) serves as the operational coordinator within the Desk during fire emergencies and is responsible for field deployment, coordinating ground combat units, managing emergency communication and weather intervention initiatives such as cloud seeding to trigger artificial rainfall (Nurhidaya & Djalante, 2017; RFMRC-SEA, 2025). It also acts as the

coordinator between the Indonesian military, national police and regional disaster mitigation agencies. The Ministry of Forestry is mandated with the technical management of forest ecosystems and sets environmental and regulatory policies (Sitanggang et al., 2022; Syaufina et al. 2024). In addition, it operates the Manggala Agni, Indonesia's forest and land fire brigade. Moreover, the Meteorology, Climatology and Geophysics Agency is responsible for weather forecasting, early warning systems and risk hotspot detection. Historically, weak coordination, fragmentation and a lack of long-term strategy have been reported as governance challenges within the fire management system (Jameaba, 2024; Roengtam & Agustiyara, 2025). The new Desk was activated to combat these issues (RFMRC-SEA, 2025).

Across Borneo, Sumatra and Java several land and fuel management practices are being used to combat fire risk. Examples are zero-burning policies and peatland (re)conservation (Budinginsih et al., 2022; Nurhidayah et al., 2023; Rositta et al. 2023). According to research enforcing effective fuel management has been reported to be undermined by overlapping land tenure conflicts, socio-economic reliance on cheap slash-and-burn clearing among smallholders, as well as gaps in enforcing zero-burning policies by commercial actors (Harrison et al., 2020; Resosudarmo et al., 2023; Jameaba, 2024).

4.5 Fire detection, response and public health protection

Indonesia's forest and land fire early warning system, SPARTAN, operated by the Meteorology, Climatology and Geophysics Agency (BMKG), assesses fire danger and potential spread using meteorological conditions (BMKG, 2026). It is complemented by the Ministry of Forestry's SiPongi+ satellite-based hotspot monitoring platform and regional fire and transboundary haze monitoring by the ASEAN Specialised Meteorological Centre (ASMC) (MoF, 2026; ASMC, 2026). Publicly accessible hotspot maps, air quality information, and advisories support risk communication (MoE, 2026). Monitoring by Indonesia's Ombudsman, an independent state institution overseeing public service delivery, across nine affected regions found that procedures for communicating fire-related information and accessing public complaint mechanisms were not consistently clear or established, making it difficult for some residents to obtain information evolving conditions and recommended protective actions (Kompas, 2026).

The primary method for measuring exposure was the Air Pollution Standard Index (ISPU), which is an index that's comprised of seven pollutants. These pollutants were collected by the roughly seventy stations, which then reported that data back to a national portal (Katadata, 2026a). When the index reaches 300, the exposure is considered 'hazardous', but by late October, Central Kalimantan's number exceeded 3,000. Moreover, the monitoring stations were placed far apart from each other, given the rural landscape they were placed in, and the sparse nature of that placement meant that ground measurements were not consistent or comprehensive, necessitating relying at least in part on satellite and model estimates for Kalimantan and Sumatra exposure (Uda et al. 2019; Graham et al., 2024).

As of 25 October, fire suppression operations across six provinces in Sumatra and Kalimantan has involved over 57,000 ground personnel and 61 aircraft, including 37 water-bombing helicopters, along with weather modification operations such as cloud seeding to induce rainfall (TheJakartaPost, 2026;

Asia News Today, 2026). In some locations, fires have been extinguished, such as in Sungai Cemara, Simpang Datuk and Labuhan Pering (Jambi); Putak village (South Sumatra); and Kalampangan and Sabaru (Central Kalimantan), with residual smoke and smouldering peat persisting and requiring continued monitoring and suppression (MoF, 2026). As of 3 November, satellite monitoring detected 64 fire hotspots across Sumatra (ASMC, 2026).

In the second half of September, Japan's Self-Defense Forces flew their first overseas firefighting mission from West Kalimantan (Bernama, 2026c), and in the last week of October Indonesia and Singapore jointly agreed to establish a task force to investigate and hold accountable the companies linked to the fires that led to the haze. (ABC, 2026). In October, the Indonesian government also responded to the wildfires by taking enforcement actions against at least 32 companies found responsible for or failing to prevent fires on their concessions including revoking permits and mandatory forest ecosystem restoration orders (Business and Human Rights Centre, 2026; Antara News, 2026). At the same time, residents in West Kalimanta sued the government for gross negligence, asking for a national disaster declaration that could allow them to cover healthcare costs related to the fires (Kuwait Times, 2026).

5 Conclusions

The Indonesian environment has changed substantially over the past four decades – with rainforest and peatlands more burnable due to degradation and less abundant due to land use change. As a point of comparison, 1997 was an emblematic year where a strong El Niño made major deforestation fires, swamp drainage and logging possible. The 2026 fire season occurred with a similar August-October El Niño, and due to the combination of that and climate change, even dryer atmospheric conditions. Despite conditions conducive to fire being more severe, burned area and emissions are not comparable to 1997 due to the huge changes there have been in Indonesian land use and consequently to the spatial distribution of forests and peatlands, and how degraded and flammable they are.

This year's fire weather conditions were record-breakingly severe, and strongly contributed to by El Niño and climate change. The first necessary condition for this year's fire activity was the very low precipitation observed over western Indonesia. This was El Niño driven, with this year's RONI estimated to have halved the rainfall this fire season compared to a neutral year. Observations showed a decreasing trend in precipitation with warming, but this is not reproduced by climate models and so remains uncertain. Additionally to precipitation, record seasonal temperature conditions exacerbated the drought. This effect is primarily climate change driven – having been made near infinitely more likely and about 1.5°C hotter due to human-induced warming. El Niño compounded this, adding an approximate 0.3°C to seasonal temperatures. Finally, short-term hot-dry extremes exacerbated fire outbreaks, and were jointly driven by warming and ENSO, with GMST found to have contributed about 430 Pa to the weekly vapour pressure deficit extreme, and El Niño approximately 570 Pa.

These fires had a number of critical impacts. Hydrologically, the reduction in post-fire absorption results in further degradation of peatlands and rainforests, meaning an increase in likelihood of greater run-off in post-fire flooding events. Ecologically, these fires will likely be used to facilitate the establishment of further agroforestry – resulting in even greater vulnerability of peatlands to future fire. And from a health perspective, there has been exposure of millions to harmful smoke from fires – likely to result in thousands of excess deaths.

As a complex Earth system process, these fires were driven by weather conditions, changes in land-use and vegetation, and human intervention. However, even if these other drivers were in another state, the effect of climate change on the driving fire weather would still exacerbate the expected scale of the fires, and their major smoke impacts on the surrounding population.

Data availability

All time series used in the attribution analysis are available via the Climate Explorer.

Input data and analysis code can be found in the following Zenodo repository – DOI: 10.5281/zenodo.24163383

Acknowledgements

This work used data obtained from the KNMI Climate explorer web tool (https://climexp.knmi.nl/start.cgi).
This work used data obtained from JASMIN, the UK's collaborative data analysis environment (https://www.jasmin.ac.uk).
Analysis was carried out using Imperial College Research Computing Service, DOI: 10.14469/hpc/2232.
This work used resources of the Deutsches Klimarechenzentrum (DKRZ), granted by its Scientific Steering Committee (WLA) under project ID bk1088 and datasets provided by ESGF and Copernicus via the DKRZ data pool.
We acknowledge the use of the ERA5-Land, MSWX, CPC and JRA-3Q observational and reanalysis data products.

References

All references are given as hyperlinks in the text.

Appendices

A1 Data and methods

A1.1 Observational data

We first use observational and reanalysis data to estimate the return period of a similar event in the present day and to assess the historical trends with increasing GMST. The datasets used are as follows:

ERA5-Land - This product is a replay of the land component of the ERA5 climate reanalysis (Muñoz-Sabater et al., 2021) produced by the European Centre for Medium-Range Weather Forecasts, with a finer spatial resolution of 0.1° (~9km grid spacing), at hourly time steps from 1950 to 5 days before the current date. The land model used is the tiled ECMWF Scheme for Surface Exchanges over Land incorporating land surface hydrology (H-TESSEL). We use mean temperature maximum dewpoint temperature data and precipitation at daily timescales from this product at a resolution of 0.5°×0.5° / 0.25°×0.25°, from the years 1950 to present.

MSWX - The Multi-Source Weather dataset (Beck et al., 2022), which combines various observational and reanalysis-based data (including ERA5) for reliable bias-corrected weather variable estimates, at 3-hourly intervals from 1979 to near real-time, and at 0.1° spatial resolution globally. We use precipitation, temperature and mean relative humidity data at daily timescales from this product.

CPC - This is the gridded product from NOAA PSL, Boulder, Colorado, USA known as the CPC Global Unified Daily Gridded data, available at 0.5° x 0.5° resolution, for the period 1979-present. We use daily maximum and minimum temperature and precipitation. Data are available from NOAA.

JRA-3Q - JRA-3Q (Japanese Reanalysis for Three Quarters of a Century) is the 3rd-generation global atmospheric reanalysis dataset produced by the Japan Meteorological Agency (JMA; Kosaka et al., 2024). It reconstructs past global atmospheric conditions seamlessly across space and time by assimilating historical weather observations with modern numerical weather prediction models and data assimilation systems. We use precipitation, temperature and minimum relative humidity data at six-hourly timescales from this product.

Covariates

As a measure of anthropogenic climate change we use the (low-pass filtered) global mean surface temperature (GMST), where GMST is taken from the National Aeronautics and Space Administration (NASA) Goddard Institute for Space Science (GISS) surface temperature analysis (GISTEMP, Hansen et al., 2010 and Lenssen et al. 2019). To remove the effect of the El Niño - Southern Oscillation on global mean temperatures, we use a four-year running mean of the GMST, centred on the third year.

As a measure of the El Niño - Southern Oscillation cycle (ENSO) we use the detrended relative Niño3.4 index (RONI). This is computed from NOAA's ERSST v.5 sea surface temperatures, by

subtracting the mean tropical SST (20S-20N) from the mean SST over the Niño3.4 region (5S-5N, 170W-120W). This index is therefore adjusted to remove the linear trend associated with climate change as proposed in van Oldenborgh et al., 2021, but without rescaling each calendar month. We use the August-October mean of this index.

A1.2 Model and experiment descriptions

We use two ensembles of climate models from climate modelling experiments using very different framings (Philip et al., 2020): Sea Surface Temperature (SST) driven global circulation high resolution models, coupled global circulation models and regional climate models.

CORDEX

1. Coordinated Regional Climate Downscaling Experiment (CORDEX)- South East Asia Domain (SEA-CORDEX) with 0.22° resolution (SEA-22) (Tangang et al., 2020). The ensemble consists of 4 regional climate models each of which are driven by 7 GCMs. These simulations are composed of historical simulations up to 2005, and extended to the year 2100 using the RCP8.5 scenario.

2. CMIP6. This consists of simulations from 34 participating models with varying resolutions. For more details on CMIP6, see Eyring et al., (2016). For all simulations, the period 1850 to 2014 is based on historical simulations, while the SSP5-8.5 scenario is used for the remainder of the 21st century.

A1.3 Statistical methods

Methods for observational and model analysis and for model evaluation and synthesis are used according to the World Weather Attribution Protocol, described in Philip et al., (2020), with supporting details found in van Oldenborgh et al., (2021), Ciavarella et al., (2021), Otto et al., (2024) and here. The key steps are: trend estimation from observations; model validation; multi-model attribution; and synthesis of the attribution statement.

In this report we analyse time series of seasonal precipitation and temperature, and week-long vapour pressure deficit. A nonstationary normal distribution is used to model seasonal temperature and precipitation, and a nonstationary GEV for VPD extremes. For precipitation, the distribution is assumed to scale exponentially with the covariates, with the dispersion (the ratio between the standard deviation and the mean) remaining constant over time; for temperatures, the distribution is assumed to shift linearly with the covariates, while the variance remains constant; as VPD scales exponentially with temperature a shift relationship was applied in logspace. The parameters of the statistical model are estimated using maximum likelihood.

For each time series we calculate the return period and intensity of the event under study for the 2026 GMST and for 1.4°C cooler GMST: this allows us to compare the climate of now and of the preindustrial past without human-caused warming (based on Forster et al., 2026), by calculating the probability ratio (PR; the factor-change in the event's probability) and change in intensity of the event.

In order to examine the effect of the ENSO phase on the fire weather alongside that of increasing GMST, we extend the nonstationary model to accommodate an additional covariate. All results quoted are from a statistical model including both covariates.

The variable of interest, X, is assumed to follow a normal/GEV distribution in which the location and scale parameters vary with both GMST and ENSO:

$$X \sim N, GEV(\mu, \sigma, \xi \mid \mu_0, \sigma_0, \alpha, \beta, T, I),$$

where X denotes the variable of interest, rainy-season precipitation; T is the smoothed GMST; I is the RONI (ASO); μ_0, σ_0 and ξ are the location, scale and shape parameters of the nonstationary distribution; and α, β are the trends due to GMST and ENSO, respectively. As a result, the location and scale of the distribution have a different value in each year, determined by both the GMST and Niño3.4 states. Maximum likelihood estimation is used to estimate the model parameters, with

$$\mu = \mu_0 exp\left(\frac{\alpha T + \beta I}{\mu_o}\right) \qquad \text{and} \qquad \sigma = \sigma_0 exp\left(\frac{\alpha T + \beta I}{\mu_o}\right).$$

This formulation reflects the Clausius Clapeyron relation, which implies that precipitation scales exponentially with temperature (Trenberth et.al., 2003, O'Gorman and Schneider 2009), and so that precipitation will scale exponentially with the strength of the detrended RONI (ASO). Under this model, the effects of GMST and the detrended RONI (ASO) are assumed to be independent of one another, so that the change in intensity due to GMST is unaffected by the change in intensity due to the ENSO phase. We note that this may not be the case in the real world, as the intensity and frequency of El Niño events may have been influenced by climate change (Cai et al., 2021); however, by using a detrended RONI (ASO) (see Section 2.1) we aim to minimise the correlation between the two factors, and so do not expect the qualitative findings of this study to be affected by this simplifying assumption.

A1.3.2 Estimation of return periods with multiple covariates

Extra care must be taken when reporting and interpreting return periods that depend on more than one covariate. Typically, WWA reports estimated return periods for the event of interest under current climatic conditions: that is, with the GMST fixed at the 2026 level. In this study, there are two covariates to consider: the GMST and ENSO. By fixing both the ENSO and the GMST at their 2026 levels, we can estimate the return period of the 2026 event in the current climate and in the current ENSO state. Mathematically, this return period is written as

$$1 / P(X > x_{2026} \mid T = t_{2026}, D = d_{2026}),$$

where x_{2026} is the 2026 value of observed event; t_{2026} denotes the 2026 GMST; and d_{2026} denotes the 2026 ENSO. Altogether, the expression in brackets gives the probability that X will exceed x_{2026}, given that $T = t_{2026}$ and $D = d_{2026}$; inverting this probability gives us an expected return period, in years.

However, this return period only tells us the probability of experiencing a similar event under current ENSO conditions and current warming levels. In order to understand how frequently such an event is actually likely to occur, we must account for the fact that the ENSO is not often in the strongly positive phase observed in 2026. To do this, we evaluate the return period over all states of the ENSO that have been recorded since 1980 (the period covered by the available gridded data products). This is done by first averaging the probability of exceeding x_{2026} over all recorded values of d_{2026} during this period, then inverting to obtain the return period:

$$1 / (\sum_{y = 1980}^{2026} P(X > x_{2026} \mid T = t_{2026}, D = d_y)/(2026 - 1980)).$$

A1.3.3 Defining the ENSO state in climate models

The multi-method multi-model attribution step of the WWA protocol involves estimating, for each climate model, the effective return level of a 1-in-*n*-year event under the current climate state, and estimating the expected change in likelihood and intensity of such an event after a specified change in the covariates. Because the smoothed GMST is generally monotonically increasing, the standard WWA approach is simply to take the model's 2026 GMST as a covariate and to estimate the expected magnitude of an *n*-year event. However, the factual climate in this study is defined by the 2026 GMST and by the mean of the detrended RONI (ASO) during the August-October season. During the attribution step, the detrended RONI (ASO) derived from the climate model is standardised so that the subset from 1979-2026 has mean 0 and variance 1; the 'factual' climate is then defined as having the model's 2026 GMST and the 2026 observed value of the detrended RONI (ASO), standardised in the same way. This removes any potential biases in the results due to differences between the amplitude of the modelled RONI (ASO) and that observed.

A2 Model evaluation

A2.1 VPD

Hurs vs Hursmin

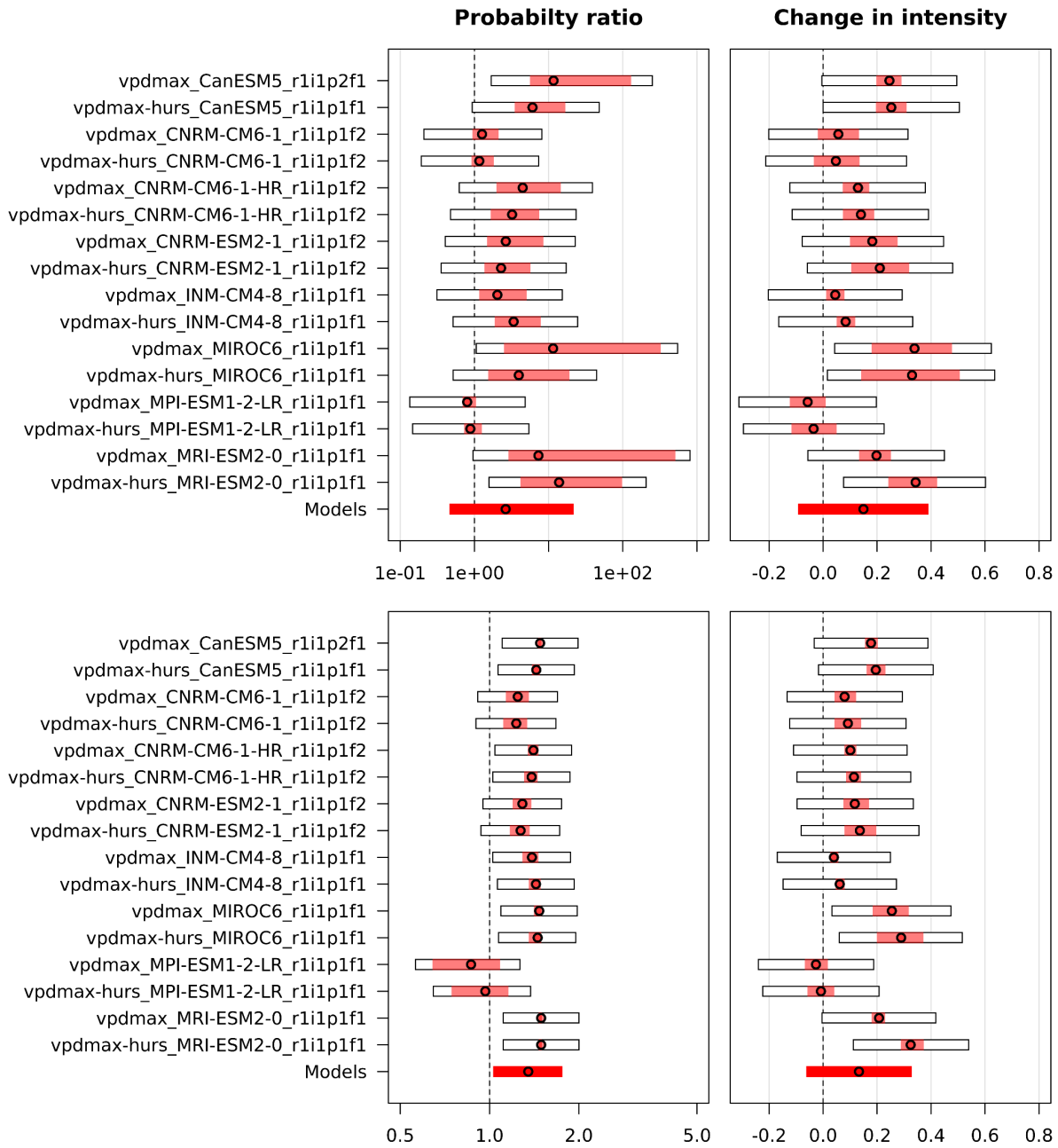


Figure A2.1.1: *Modelled trends in VPDX7x in the study region due to GMST for a range of climate models with both hurs and hursmin variables available. Probability ratio (left) and changes in intensity (right) are shown for a historical period comparing the past 1.4°C cooler climate with the present (top row) and for a future period, based on model projections only, comparing the present and a 2.8 °C warmed climate (bottom row).*

Effect of ENSO evaluation

Data	Influence of GMST increase of 1.4°C			Influence of El Niño	
	Time period	Probability ratio (95% CI)	Intensity change (kPa) (95% CI)	Probability ratio (95% CI)	Intensity change (kPa) (95% CI)
Observations	**Preindustrial - present**	**15.2 (1.70, 423)**	**0.508 (0.259, 0.745)**	**27.3 (6.53, 4830)**	**0.600 (0.357, 0.834)**
Models		2.22 (0.681, 17.9)	**0.422 (0.208, 0.594)**	**5.91 (1.37, 37.0)**	**0.591 (0.288, 0.903)**
Synthesis		3.67 (0.809, 43.4)	**0.455 (0.227, 0.655)**	**8.02 (1.87, 136)**	**0.597 (0.329, 0.862)**
Models	**Present - future**	**1.35 (1.11, 1.64)**	**0.385 (0.0797, 0.698)**		

Table A2.1.1: *Equivalent of Table 3.1 but including a model evaluation step for correlation between model time series of Log(VPDX7x) and RONI ASO based on the values shown in Table A2.1.2. This reduces the number of independent models from 8 to 4.*

Dataset	RONI ASO correlation (95% confidence interval)		
	Best estimate	Lower bound	Upper bound
Observations			
ERA5-Land	0.731	0.595	0.832
JRA-3Q	0.773	0.636	0.871
MSWX (Hurs)	0.714	0.536	0.842
Models			
CMIP6 - CNRM-CM6-1 r1i1p1f2	0.406543	0.283635	0.511594
CMIP6 - CNRM-CM6-1-HR r1i1p1f2	0.357035	0.239853	0.459337
CMIP6 - CNRM-ESM2-1 r1i1p1f2	0.542877	0.461435	0.61836
CMIP6 - MRI-ESM2-0 r1i1p1f1	0.53148	0.433194	0.619891
CMIP6 - EC-Earth3 r1i1p1f1 (hurs)	0.740607	0.677285	0.79129
CMIP6 - UKESM1-0-LL r2i1p1f2 (hurs)	0.405857	0.310026	0.502552
CORDEX - IPSL-CM5A-LR RURegCM4-3 (hurs)	0.17657	0.000629	0.330787
CORDEX - NorESM1-M RegCM4-7 (hurs)	0.729391	0.643798	0.799154

Table A2.1.2: *Correlation between Log(VPDX7x) in the western Indonesia study region and the RONI ASO for each observational dataset and climate model that passed the other model evaluation steps. The 95% confidence interval is obtained through bootstrapping. Models are ranked 'good' (green), 'reasonable' (yellow) or 'bad' (red) if the calculated best estimates of the correlations fall within the observed uncertainty range, if the uncertainty ranges overlap, or if there is no overlap, respectively.*

Evaluation tables

Model / Observations	Seasonal cycle	Spatial pattern	Sigma	Shape parameter	Conclusion
ERA5-Land			0.0869 (0.0676 ... 0.101)	-0.029 (-0.21 ... 0.22)	
JRA-3Q			0.0970 (0.0753 ... 0.113)	-0.13 (-0.40 ... 0.040)	
MSWX			0.0877 (0.0626 ... 0.133)	-0.0092 (-0.74 ... 0.37)	
CMIP6_vpdmax_CNRM-CM6-1_r1i1p1f2	reasonable	reasonable	0.163 (0.113 ... 0.246)	-0.82 (-1.2 ... -0.41)	reasonable
CMIP6_vpdmax_CNRM-CM6-1-HR_r1i1p1f2	reasonable	good	0.0680 (0.0521 ... 0.0801)	-0.16 (-0.63 ... 0.12)	reasonable
CMIP6_vpdmax_CNRM-ESM2-1_r1i1p1f2	reasonable	reasonable	0.138 (0.106 ... 0.239)	-0.51 (-1.1 ... -0.38)	reasonable
CMIP6_vpdmax_INM-CM4-8_r1i1p1f1	bad	bad	0.0518 (0.0352 ... 0.0855)	-0.22 (-1.1 ... 0.16)	bad
CMIP6_vpdmax_INM-CM5-0_r1i1p1f1	bad	reasonable	0.0503 (0.0342 ... 0.0622)	-0.11 (-0.41 ... 0.17)	bad
CMIP6_vpdmax_MIROC6_r1i1p1f1	bad	good	0.160 (0.124 ... 0.206)	-0.29 (-1.0 ... -0.13)	bad
CMIP6_vpdmax_MIROC6_r2i1p1f1	bad	good	0.159 (0.119 ... 0.242)	-0.32 (-1.1 ... -0.052)	bad
CMIP6_vpdmax_MRI-ESM2-0_r1i1p1f1	good	good	0.0944 (0.0685 ... 0.132)	-0.38 (-1.1 ... -0.039)	good
CMIP6_vpdmax-hurs_EC-Earth3_r1i1p1f1	reasonable	good	0.169 (0.102 ... 0.275)	-0.25 (-1.1 ... 0.16)	reasonable
CMIP6_vpdmax-hurs_GFDL-ESM4_r1i1p1f1	bad	reasonable	0.152 (0.0850 ... 0.209)	0.050 (-0.40 ... 0.71)	bad
CMIP6_vpdmax-hurs_HadGEM3-GC31-MM_r1i1p1f3	reasonable	good	0.191 (0.152 ... 0.278)	-0.43 (-1.1 ... -0.25)	bad

CMIP6_vpdmax-hurs_KACE-1-0-G_r1i1p1f1	reasonable	reasonable	0.199 (0.140 ... 0.320)	-0.40 (-1.1 ... -0.11)	bad
CMIP6_vpdmax-hurs_NorESM2-MM_r1i1p1f1	bad	reasonable	0.231 (0.0937 ... 0.272)	-1.0 (-1.2 ... 0.35)	bad
CMIP6_vpdmax-hurs_UKESM1-0-LL_r2i1p1f2	good	reasonable	0.130 (0.0923 ... 0.158)	-0.16 (-0.44 ... 0.19)	reasonable
CMIP6_vpdmax-hurs_UKESM1-0-LL_r3i1p1f2	good	reasonable	0.155 (0.116 ... 0.216)	-0.29 (-1.1 ... 0.029)	reasonable
CMIP6_vpdmax-hurs_UKESM1-0-LL_r4i1p1f2	good	reasonable	0.164 (0.116 ... 0.218)	-0.37 (-1.0 ... -0.031)	reasonable
CMIP6_vpdmax-hurs_UKESM1-0-LL_r8i1p1f2	good	reasonable	0.183 (0.132 ... 0.244)	-0.37 (-1.0 ... -0.087)	reasonable
CORDEX_vpdmax-hurs_EC-EARTH_RURegCM4-3	bad	bad	0.141 (0.0851 ... 0.188)	0.34 (-0.11 ... 1.0)	bad
CORDEX_vpdmax-hurs_HadGEM2-ES_RegCM4-7	reasonable	reasonable	0.232 (0.163 ... 0.352)	-0.49 (-1.1 ... -0.18)	bad
CORDEX_vpdmax-hurs_IPSL-CM5A-LR_RURegCM4-3	good	good	0.127 (0.0906 ... 0.199)	-0.47 (-1.1 ... -0.14)	good
CORDEX_vpdmax-hurs_MPI-ESM-MR_RegCM4-7	bad	bad	0.282 (0.191 ... 0.471)	-0.15 (-1.1 ... 0.22)	bad
CORDEX_vpdmax-hurs_MPI-ESM-MR_RURegCM4-3	bad	bad	0.253 (0.166 ... 0.348)	-0.40 (-1.1 ... 0.18)	bad
CORDEX_vpdmax-hurs_NorESM1-M_RegCM4-7	reasonable	reasonable	0.185 (0.122 ... 0.287)	-0.48 (-1.1 ... -0.18)	reasonable

Table A2.1.3: *Evaluation results of the climate models considered for attribution analysis of VPDX7x. For each model, the threshold for a 2-in-3-year event is shown, along with the best estimates of the Sigma and Shape parameters are shown, along with 95% confidence intervals. Furthermore evaluation of the seasonal cycle and spatial pattern are shown.*

A2.2 Precipitation

Model / Observations	Seasonal cycle	Spatial pattern	Dispersion	Correlation b/w RONI-ASO and prJASO	Conclusion

CPC			0.223 (0.164 ... 0.267)	-0.84 (-0.90 ... -0.76)	
ERA5-Land			0.195 (0.154 ... 0.229)	-0.81 (-0.88 ... -0.71)	
JRA-3Q			0.232 (0.195 ... 0.260)	-0.74 (-0.83 ... -0.64)	
MSWX			0.184 (0.141 ... 0.214)	-0.84 (-0.91 ... -0.73)	
CMIP6					
ACCESS-CM2_r1i1p1f1 ()	good	good	0.214 (0.153 ... 0.250)	-0.71 (-0.89 ... -0.67)	good
ACCESS-CM2_r2i1p1f1 ()	good	good	0.240 (0.155 ... 0.323)	-0.70 (-0.84 ... -0.62)	good
ACCESS-CM2_r3i1p1f1 ()	good	good	0.182 (0.138 ... 0.214)	-0.78 (-0.93 ... -0.73)	good
ACCESS-ESM1-5_r1i1p1f1 ()	reasonable	good	0.274 (0.208 ... 0.326)	-0.44 (-0.41 ... 0.15)	bad
BCC-CSM2-MR_r1i1p1f1 ()	good	good	0.179 (0.138 ... 0.206)	-0.45 (-0.51 ... -0.024)	bad
CAMS-CSM1-0_r2i1p1f1 ()	reasonable	good	0.243 (0.169 ... 0.302)	-0.67 (-0.90 ... -0.61)	reasonable (2 goods)
CESM2_r11i1p1f1 ()	reasonable	good	0.339 (0.262 ... 0.394)	-0.79 (-0.86 ... -0.67)	reasonable
CESM2-WACCM_r2i1p1f1 ()	reasonable	good	0.337 (0.269 ... 0.378)	-0.76 (-0.90 ... -0.76)	bad
CESM2-WACCM_r3i1p1f1 ()	reasonable	good	0.336 (0.240 ... 0.397)	-0.73 (-0.91 ... -0.74)	reasonable
CMCC-CM2-SR5_r1i1p1f1 ()	reasonable	reasonable	0.201 (0.139 ... 0.249)	-0.84 (-0.93 ... -0.74)	reasonable
CMCC-ESM2_r1i1p1f1 ()	good	reasonable	0.289 (0.221 ... 0.326)	-0.85 (-0.91 ... -0.74)	reasonable
CNRM-CM6-1_r1i1p1f2 ()	reasonable	good	0.301 (0.233 ... 0.350)	-0.63 (-0.77 ... -0.39)	reasonable
CNRM-CM6-1-HR_r1i1p1f2 ()	reasonable	good	0.202 (0.156 ... 0.235)	-0.67 (-0.66 ... -0.21)	reasonable (2 goods)
CNRM-ESM2-1_r1i1p1f2 ()	reasonable	good	0.335 (0.256 ... 0.391)	-0.70 (-0.81 ... -0.43)	reasonable
EC-Earth3_r1i1p1f1 ()	good	good	0.267 (0.196 ... 0.316)	-0.75 (-0.86 ... -0.44)	good
EC-Earth3-CC_r1i1p1f1 ()	reasonable	good	0.271 (0.212 ... 0.311)	-0.76 (-0.85 ... -0.68)	reasonable

EC-Earth3-Veg_r1i1p1f1 ()	reasonable	good	0.284 (0.228 ... 0.324)	-0.72 (-0.84 ... -0.55)	reasonable
EC-Earth3-Veg_r2i1p1f1 ()	reasonable	good	0.280 (0.210 ... 0.341)	-0.75 (-0.89 ... -0.70)	reasonable
EC-Earth3-Veg_r3i1p1f1 ()	reasonable	good	0.329 (0.264 ... 0.371)	-0.74 (-0.82 ... -0.53)	reasonable
EC-Earth3-Veg_r4i1p1f1 ()	reasonable	good	0.243 (0.184 ... 0.288)	-0.74 (-0.83 ... -0.52)	reasonable (2 goods)
EC-Earth3-Veg_r6i1p1f1 ()	reasonable	good	0.236 (0.184 ... 0.269)	-0.75 (-0.79 ... -0.56)	reasonable (2 goods)
EC-Earth3-Veg-LR_r1i1p1f1 ()	reasonable	good	0.263 (0.197 ... 0.309)	-0.77 (-0.91 ... -0.70)	reasonable (2 goods)
GFDL-ESM4_r1i1p1f1 ()	reasonable	reasonable	0.233 (0.176 ... 0.268)	-0.71 (-0.80 ... -0.34)	reasonable
HadGEM3-GC31-LL_r1i1p1f3 ()	good	reasonable	0.313 (0.238 ... 0.362)	-0.63 (-0.85 ... -0.47)	reasonable
HadGEM3-GC31-LL_r2i1p1f3 ()	good	good	0.298 (0.183 ... 0.365)	-0.64 (-0.76 ... -0.27)	reasonable
HadGEM3-GC31-LL_r3i1p1f3 ()	good	reasonable	0.392 (0.253 ... 0.467)	-0.58 (-0.73 ... -0.27)	reasonable
HadGEM3-GC31-LL_r4i1p1f3 ()	good	reasonable	0.349 (0.205 ... 0.448)	-0.69 (-0.83 ... -0.28)	reasonable
HadGEM3-GC31-MM_r1i1p1f3 ()	good	good	0.229 (0.162 ... 0.269)	-0.67 (-0.81 ... -0.47)	good
HadGEM3-GC31-MM_r2i1p1f3 ()	good	good	0.288 (0.219 ... 0.337)	-0.65 (-0.81 ... -0.55)	reasonable (2 goods)
HadGEM3-GC31-MM_r3i1p1f3 ()	good	good	0.286 (0.228 ... 0.323)	-0.66 (-0.86 ... -0.58)	reasonable (2 goods)
KACE-1-0-G_r1i1p1f1 ()	good	reasonable	0.298 (0.243 ... 0.337)	0.18 (-0.081 ... 0.60)	bad
KACE-1-0-G_r2i1p1f1 ()	good	reasonable	0.298 (0.227 ... 0.343)	0.049 (0.014 ... 0.71)	bad
KACE-1-0-G_r3i1p1f1 ()	good	reasonable	0.279 (0.209 ... 0.320)	0.086 (-0.44 ... 0.39)	bad
MIROC6_r2i1p1f1 ()	bad	bad	0.150 (0.108 ... 0.182)	-0.83 (-0.91 ... -0.72)	bad
MIROC6_r3i1p1f1 ()	bad	bad	0.154 (0.108 ... 0.185)	-0.82 (-0.90 ... -0.72)	bad
MRI-ESM2-0_r1i2p1f1 ()	good	good	0.280 (0.215 ... 0.329)	-0.72 (-0.83 ... -0.56)	reasonable
NorESM2-MM_r1i1p1f1 ()	bad	bad	0.235 (0.167 ... 0.281)	-0.61 (-0.75 ... -0.31)	bad

UKESM1-0-LL_r2i1p1f2 ()	good	reasonable	0.239 (0.170 ... 0.293)	-0.58 (-0.80 ... -0.45)	reasonable
UKESM1-0-LL_r3i1p1f2 ()	good	reasonable	0.363 (0.283 ... 0.421)	-0.62 (-0.81 ... -0.42)	bad
UKESM1-0-LL_r4i1p1f2 ()	good	reasonable	0.345 (0.271 ... 0.401)	-0.55 (-0.73 ... -0.34)	bad
UKESM1-0-LL_r8i1p1f2 ()	good	reasonable	0.371 (0.272 ... 0.422)	-0.55 (-0.71 ... -0.13)	bad
CORDEX					
CNRM-CM5_SMHI-RCA4_r1i1p1 ()	good	bad	0.351 (0.271 ... 0.571)	-0.73 (-0.87 ... -0.59)	bad
HadGEM2-ES_GERICS-REMO2015_r1i1p1 ()	good	bad	0.275 (0.183 ... 0.319)	-0.37 (-0.48 ... 0.0056)	bad
HadGEM2-ES_ICTP-RegCM4-7_r1i1p1 ()	good	reasonable	0.198 (0.152 ... 0.227)	-0.51 (-0.65 ... -0.21)	reasonable
MPI-ESM-LR_GERICS-REMO2015_r1i1p1 ()	bad	bad	0.252 (0.186 ... 0.295)	-0.53 (-0.82 ... -0.35)	bad
MPI-ESM-MR_ICTP-RegCM4-7_r1i1p1 ()	bad	reasonable	0.252 (0.189 ... 0.292)	-0.58 (-0.80 ... -0.47)	bad
MPI-ESM-MR_RU-CORE-RegCM4-3_r1i1p1 ()	reasonable	bad	0.143 (0.110 ... 0.166)	-0.55 (-0.74 ... -0.23)	bad
NorESM1-M_ICTP-RegCM4-7_r1i1p1 ()	reasonable	reasonable	0.205 (0.145 ... 0.414)	-0.79 (-0.94 ... -0.76)	reasonable
GFDL-ESM2M_RU-CORE-RegCM4-3_r1i1p1 ()	reasonable	reasonable	0.220 (0.161 ... 0.245)	-0.73 (-0.84 ... -0.59)	reasonable

Table A2.2: *Evaluation results of the climate models considered for attribution analysis of pr-JASO. For each model, the threshold for a 20-year event is shown, along with the best estimates of the dispersion parameter and RONI (ASO) correlation are shown, along with 95% confidence intervals. Furthermore evaluation of the seasonal cycle and spatial pattern are shown.*

A2.3 Temperatures

Model / Observations	Seasonal cycle	Spatial pattern	Sigma	Correlation b/w RONI-ASO and tasASO	Conclusion
CPC			0.19 (0.13, 0.22)	0.14 (-0.18 ...	

				0.44)	
ERA5-Land			0.24 (0.2, 0.28)	0.84 (0.72 ... 0.91)	
JRA			0.18 (0.15, 0.2)	0.67 (0.35 ... 0.85)	
MSWX			0.19 (0.15, 0.22)	0.65 (0.42 ... 0.81)	
cmip6					
ACCESS-CM2_r1i1p1f1 ()	good	reasonable	0.258 (0.216 ... 0.291)	0.020 (-0.54 ... 0.20)	good
BCC-CSM2-MR_r1i1p1f1 ()	good	reasonable	0.224 (0.186 ... 0.251)	0.14 (-0.43 ... 0.27)	good
CAMS-CSM1-0_r2i1p1f1 ()	good	good	0.259 (0.214 ... 0.293)	0.23 (0.13 ... 0.61)	good
CanESM5_r2i1p1f1 ()	good	bad	0.165 (0.137 ... 0.184)	0.27 (-0.40 ... 0.37)	bad
CESM2_r10i1p1f1 ()	good	good	0.153 (0.123 ... 0.178)	0.075 (-0.29 ... 0.36)	good
CESM2-WACCM_r1i1p1f1 ()	reasonable	good	0.161 (0.134 ... 0.178)	0.13 (-0.14 ... 0.54)	reasonable
CMCC-CM2-SR5_r1i1p1f1 ()	reasonable	reasonable	0.198 (0.159 ... 0.229)	0.27 (0.21 ... 0.78)	bad
CMCC-ESM2_r1i1p1f1 ()	good	reasonable	0.279 (0.230 ... 0.310)	0.24 (-0.049 ... 0.72)	reasonable
CNRM-CM6-1_r1i1p1f2 ()	good	good	0.275 (0.233 ... 0.303)	0.068 (-0.011 ... 0.59)	good
CNRM-CM6-1-HR_r1i1p1f2 ()	reasonable	good	0.202 (0.166 ... 0.231)	0.032 (-0.33 ... 0.38)	reasonable
CNRM-ESM2-1_r1i1p1f2 ()	good	reasonable	0.374 (0.314 ... 0.424)	0.17 (0.29 ... 0.73)	bad
EC-Earth3_r1i1p1f1 ()	good	reasonable	0.518 (0.431 ... 0.583)	0.47 (0.15 ... 0.77)	bad
EC-Earth3-CC_r1i1p1f1 ()	good	reasonable	0.533 (0.450 ... 0.599)	0.46 (0.55 ... 0.85)	bad
EC-Earth3-Veg_r1i1p1f1 ()	good	good	0.556 (0.471 ... 0.611)	0.50 (0.30 ... 0.79)	reasonable
EC-Earth3-Veg-LR_r1i1p1f1 ()	reasonable	good	0.467 (0.388 ... 0.526)	0.45 (0.47 ... 0.84)	bad
GFDL-ESM4_r1i1p1f1 ()	good	good	0.256 (0.209 ... 0.291)	0.27 (0.011 ... 0.72)	reasonable

HadGEM3-GC31-LL_r1i1p1f3 ()	good	reasonable	0.267 (0.211 ... 0.313)	0.16 (-0.22 ... 0.36)	reasonable
HadGEM3-GC31-MM_r1i1p1f3 ()	good	good	0.358 (0.266 ... 0.435)	0.078 (-0.18 ... 0.40)	reasonable
IITM-ESM_r1i1p1f1 ()	good	reasonable	0.254 (0.210 ... 0.286)	0.048 (0.35 ... 0.75)	reasonable
INM-CM4-8_r1i1p1f1 ()	good	reasonable	0.119 (0.0998 ... 0.132)	0.0098 (-0.33 ... 0.33)	bad
INM-CM5-0_r1i1p1f1 ()	good	reasonable	0.150 (0.119 ... 0.170)	-0.020 (-0.48 ... 0.25)	reasonable
KACE-1-0-G_r1i1p1f1 ()	good	reasonable	0.424 (0.330 ... 0.508)	0.38 (-0.39 ... 0.26)	bad
KIOST-ESM_r1i1p1f1 ()	good	reasonable	0.305 (0.261 ... 0.340)	0.29 (0.35 ... 0.78)	bad
MIROC-ES2L_r1i1p1f2 ()	good	bad	0.215 (0.167 ... 0.256)	0.29 (0.29 ... 0.70)	bad
MIROC6_r1i1p1f1 ()	reasonable	reasonable	0.334 (0.257 ... 0.385)	0.44 (0.60 ... 0.88)	bad
MPI-ESM1-2-LR_r10i1p1f1 ()	good	reasonable	0.251 (0.201 ... 0.289)	0.26 (0.36 ... 0.80)	reasonable
MRI-ESM2-0_r1i1p1f1 ()	good	reasonable	0.215 (0.169 ... 0.249)	0.22 (-0.13 ... 0.55)	reasonable
NESM3_r2i1p1f1 ()	good	reasonable	0.310 (0.263 ... 0.346)	-0.059 (-0.54 ... 0.049)	bad
NorESM2-LM_r1i1p1f1 ()	reasonable	reasonable	0.197 (0.166 ... 0.224)	0.00059 (-0.19 ... 0.52)	bad
NorESM2-MM_r1i1p1f1 ()	good	good	0.226 (0.178 ... 0.263)	-0.0038 (-0.078 ... 0.56)	good
cordex					
CNRM-CM5_SMHI-RCA4_r1i1p1 ()	good	good	0.408 (0.338 ... 0.455)	0.33 (0.10 ... 0.79)	reasonable
EC-EARTH_RU-CORE-RegCM4-3_r1i1p1 ()	bad	good	0.156 (0.110 ... 0.203)	0.36 (-0.37 ... 0.12)	bad
HadGEM2-ES_GERICS-REMO2015_r1i1p1 ()	good	good	0.542 (0.452 ... 0.605)	0.22 (-0.17 ... 0.53)	reasonable
HadGEM2-ES_ICTP-RegCM4-7_r1i1p1 ()	good	good	0.247 (0.190 ... 0.284)	0.19 (-0.13 ... 0.54)	good
HadGEM2-ES_SM	good	good	0.284 (0.229 ...	0.13 (-0.41 ...	good

HI-RCA4_r1i1p1 ()			0.320)	0.39)	
MPI-ESM-LR_GERICS-REMO2015_r1i1p1 ()	good	good	0.396 (0.309 ... 0.449)	0.18 (0.32 ... 0.80)	reasonable
MPI-ESM-MR_RU-CORE-RegCM4-3_r1i1p1 ()	reasonable	good	0.158 (0.127 ... 0.178)	0.12 (-0.30 ... 0.58)	reasonable

Table A2.3: *Evaluation results of the climate models considered for attribution analysis of tas-ASO. For each model, the threshold for a 20-year event is shown, along with the best estimates of the sigma parameter and RONI (ASO) correlation are shown, along with 95% confidence intervals. Furthermore evaluation of the seasonal cycle and spatial pattern are shown.*

A3 Estimated trends in climate models

This section shows Probability Ratios and change in intensity ΔI for models that passed model evaluation and also includes the values calculated from the fits with observations for each variable.

A3.1 VPD

Model / Observations	**Threshold for return period 1.5 yr (kPa)**	**Probability ratio PR [-]**	**Change in intensity ΔI (kPa)**	**Probability ratio PR [-]**	**Change in intensity ΔI (kPa)**
ERA5-Land	2.41	6.1 (2.9 ... 17)	0.42 (0.23 ... 0.57)		
JRA-3Q	2.92	13 (5.3 ... 1.8e+2)	0.59 (0.40 ... 0.77)		
MSWX	1.66	43 (9.4 ... ∞)	0.51 (0.34 ... 0.69)		
CMIP6_vpdmax_CNRM-CM6-1_r1i1p1f2	3.1	1.3 (0.94 ... 2.1)	0.17 (-0.062 ... 0.38)	1.2 (1.1 ... 1.4)	0.24 (0.13 ... 0.36)
CMIP6_vpdmax_CNRM-CM6-1-HR_r1i1p1f2	3.2	4.5 (2.0 ... 15)	0.39 (0.23 ... 0.51)	1.4 (1.3 ... 1.5)	0.31 (0.24 ... 0.37)
CMIP6_vpdmax_CNRM-ESM2-1_r1i1p1f2	3.4	2.7 (1.5 ... 8.5)	0.57 (0.32 ... 0.83)	1.3 (1.2 ... 1.4)	0.38 (0.25 ... 0.54)
CMIP6_vpdmax_MRI-ESM2-0_r1i1p1f1	2.5	7.3 (2.9 ... 5.1e+2)	0.44 (0.31 ... 0.55)	1.5 (1.5 ... 1.5)	0.46 (0.41 ... 0.51)
CMIP6_vpdmax-hurs_EC-Earth3_r1i1p1f1	2.3	1.8 (1.3 ... 3.1)	0.34 (0.19 ... 0.49)	1.2 (1.1 ... 1.3)	0.18 (0.085 ... 0.29)

CMIP6_vpdmax-hurs_UKESM1-0-LL_r2i1p1f2	1.7	3.5 (1.9 ... 8.3)	0.35 (0.22 ... 0.46)	1.5 (1.4 ... 1.5)	0.32 (0.27 ... 0.37)
CMIP6_vpdmax-hurs_UKESM1-0-LL_r3i1p1f2	1.8	2.9 (1.7 ... 6.0)	0.32 (0.19 ... 0.42)	1.4 (1.4 ... 1.5)	0.32 (0.26 ... 0.37)
CMIP6_vpdmax-hurs_UKESM1-0-LL_r4i1p1f2	1.7	2.4 (1.4 ... 5.1)	0.26 (0.12 ... 0.38)	1.5 (1.4 ... 1.5)	0.34 (0.29 ... 0.38)
CMIP6_vpdmax-hurs_UKESM1-0-LL_r8i1p1f2	1.7	2.3 (1.4 ... 4.4)	0.26 (0.14 ... 0.36)	1.4 (1.4 ... 1.5)	0.28 (0.23 ... 0.33)
CORDEX_vpdmax-hurs_IPSL-CM5A-LR_RURegCM4-3	1.5	1.4 (0.92 ... 6.0)	0.081 (-0.026 ... 0.22)	1.4 (1.3 ... 1.4)	0.13 (0.085 ... 0.19)
CORDEX_vpdmax-hurs_NorESM1-M_RegCM4-7	2.3	1.4 (0.73 ... 32)	0.22 (-0.87 ... 0.72)	1.4 (1.3 ... 1.5)	0.55 (0.36 ... 0.78)

Table A3.1.1: *Event magnitude, probability ratio and change in intensity for 2-in-3-year return period for VPDX7x for observational datasets and each model that passed the evaluation tests. (a) from pre-industrial climate to the present and (b) from the present to 2.8℃ above pre-industrial climate.*

Model / Observations	**Threshold for return period 2-in-3 yr (kPa)**	**Probability ratio PR [-]**	**Change in intensity ΔI [kPa]**
ERA5-Land	2.41	39 (15 ... 9.0e+2)	0.71 (0.60 ... 0.79)
JRA-3Q	2.92	15 (6.7 ... 8.3e+4)	0.60 (0.49 ... 0.72)
MSWX	1.66	36 (11 ... ∞)	0.49 (0.37 ... 0.56)
CMIP6_vpdmax_CNRM-CM6-1_r1i1p1f2	3.1	4.7 (2.2 ... 16)	0.60 (0.43 ... 0.74)
CMIP6_vpdmax_CNRM-CM6-1-HR_r1i1p1f2	3.2	2.1 (1.4 ... 4.5)	0.25 (0.16 ... 0.35)
CMIP6_vpdmax_CNRM-ESM2-1_r1i1p1f2	3.4	2.8 (1.9 ... 7.0)	0.58 (0.45 ... 0.78)
CMIP6_vpdmax_MRI-ESM2-0_r1i1p1f1	2.5	7.6 (3.4 ... 40)	0.45 (0.34 ... 0.53)
CMIP6_vpdmax-hurs_EC-Earth3_r1i1p1f1	2.3	13 (6.0 ... 49)	0.75 (0.63 ... 0.88)
CMIP6_vpdmax-hurs_UKESM1-0-LL_r2i1p1f2	1.7	4.1 (2.8 ... 7.0)	0.37 (0.31 ... 0.43)
CMIP6_vpdmax-hurs_UKESM1-0-LL_r3i1p1f2	1.8	19 (7.9 ... 3.5e+2)	0.55 (0.48 ... 0.63)
CMIP6_vpdmax-hurs_UKESM1-0-LL_r4i1p1f2	1.7	11 (5.4 ... 47)	0.48 (0.40 ... 0.56)

CMIP6_vpdmax-hurs_UKESM1-0-LL_r8i1p1f2	1.7	4.1 (2.5 ... 8.6)	0.36 (0.28 ... 0.44)
CORDEX_vpdmax-hurs_IPSL-CM5A-LR_RUReg CM4-3	1.5	1.4 (0.94 ... 2.4)	0.084 (-0.022 ... 0.16)
CORDEX_vpdmax-hurs_NorESM1-M_RegCM4-7	2.3	∞ (2.7e+3 ... ∞)	1.1 (0.89 ... 1.2)

Table A3.1.2: *Event magnitude, probability ratio and change in intensity for 2-in-3-year return period for VPDX7x for observational datasets and each model that passed the evaluation tests, from RONI ASO in 2026 vs neutral conditions in the present climate.*

A3.2 Precipitation

Model / Observations	**Threshold for return period 20 yr**	**(a) Pre-industrial vs. present**		**(b) Present vs. 2.8°C above pre-industrial**	
		Probability ratio PR [-]	**Change in intensity ΔI [%]**	**Probability ratio PR [-]**	**Change in intensity ΔI [%]**
CPC	163 mm	0.82 (0.13 ... 4.7)	3.6 (-24 ... 38)		
ERA5-Land	198 mm	4.6 (1.5 ... 19)	-19 (-32 ... -5.6)		
JRA-3Q	175 mm	3.0 (1.3 ... 9.4)	-18 (-32 ... -4.3)		
MSWX	174 mm	21 (2.4 ... 3.3e+2)	-31 (-47 ... -9.8)		
ACCESS-CM2_r1i1p1f1 ()	2.6e+2 mm	1.0 (0.99 ... 1.1)	-0.20 (-1.0 ... 0.12)	1.0 (1.0 ... 1.2)	-0.49 (-2.9 ... -0.089)
ACCESS-CM2_r2i1p1f1 ()	2.8e+2 mm	1.0 (0.99 ... 1.0)	-0.22 (-0.71 ... 0.11)	1.2 (1.0 ... 1.3)	-2.2 (-3.9 ... -0.65)
ACCESS-CM2_r3i1p1f1 ()	2.4e+2 mm	1.1 (1.0 ... 1.1)	-0.80 (-1.4 ... -0.44)	1.1 (1.1 ... 1.2)	-1.6 (-2.9 ... -0.80)
CAMS-CSM1-0_r2i1p1f1 ()	1.2e+2 mm	1.0 (1.0 ... 1.1)	-0.57 (-1.6 ... -0.22)	0.93 (0.87 ... 1.0)	1.7 (-0.73 ... 3.1)
CNRM-CM6-1-HR_r1i1p1f2 ()	1.4e+2 mm	1.1 (1.0 ... 1.3)	-1.8 (-4.5 ... -0.51)	1.0 (0.94 ... 1.2)	-0.71 (-3.1 ... 1.0)
EC-Earth3_r1i1p1f1 ()	1.5e+2 mm	2.0 (1.1 ... 4.6)	-12 (-24 ... -2.1)	1.1 (0.89 ... 1.3)	-1.1 (-5.6 ... 2.2)
EC-Earth3-Veg_r4i1p1f1 ()	1.3e+2 mm	1.0 (1.0 ... 1.1)	-0.99 (-1.6 ... -0.45)	1.1 (1.0 ... 1.2)	-1.4 (-3.4 ... -0.89)

EC-Earth3-Veg_r6i1p1f1 ()	1.5e+2 mm	1.0 (1.0 ... 1.1)	-0.82 (-2.2 ... -0.38)	1.1 (1.0 ... 1.2)	-1.6 (-3.8 ... -0.70)
EC-Earth3-Veg-LR_r1i1p1f1 ()	1.3e+2 mm	1.0 (1.0 ... 1.1)	-0.70 (-1.3 ... -0.19)	1.1 (1.0 ... 1.2)	-1.2 (-3.4 ... -0.66)
HadGEM3-GC31-MM_r1i1p1f3 ()	1.3e+2 mm	1.0 (1.0 ... 1.2)	-0.79 (-3.1 ... -0.098)	1.2 (1.1 ... 1.5)	-4.0 (-8.2 ... -1.6)
HadGEM3-GC31-MM_r2i1p1f3 ()	1.2e+2 mm	1.0 (0.98 ... 1.1)	-0.34 (-1.7 ... 0.30)	1.2 (1.1 ... 1.4)	-4.6 (-7.6 ... -1.7)
HadGEM3-GC31-MM_r3i1p1f3 ()	1.2e+2 mm	1.1 (1.0 ... 1.1)	-1.3 (-1.9 ... -0.0080)	1.1 (1.1 ... 1.4)	-2.7 (-6.8 ... -1.2)
HadGEM2-ES_ICTP-RegCM4-7_r1i1p1 ()	3.1e+2 mm	1.2 (0.47 ... 3.5)	-2.6 (-15 ... 11)	1.1 (0.86 ... 1.6)	-2.5 (-8.5 ... 2.8)
NorESM1-M_ICTP-RegCM4-7_r1i1p1 ()	1.7e+2 mm	1.7 (0.38 ... 12)	-8.7 (-28 ... 19)	1.4 (0.93 ... 2.3)	-7.6 (-18 ... 1.7)
GFDL-ESM2M_RU-CORE-RegCM4-3_r1i1p1 ()	4.0e+2 mm	2.1 (0.58 ... 8.2)	-12 (-28 ... 8.9)	1.8 (1.1 ... 2.9)	-11 (-21 ... -1.8)

Table A3.2.1: *Event magnitude, probability ratio and change in intensity for 1-in-20-year return period for pr-JASO for observational datasets and each model that passed the evaluation tests. (a) from pre-industrial climate to the present and (b) from the present to 2.8℃ above pre-industrial climate.*

Model / Observations	**Threshold for return period 20 yr**	**Probability ratio PR [-]**	**Change in intensity ΔI [mm]**
CPC	276.4424 mm	68 (18 ... 2.4e+3)	-54 (-60 ... -46)
ERA5-Land	125.7172 mm	1.2e+2 (31 ... 1.5e+3)	-48 (-54 ... -43)
JRA-3Q	240.1091 mm	39 (15 ... 2.1e+2)	-51 (-57 ... -45)
MSWX	161.2378 mm	3.2e+2 (71 ... 1.2e+4)	-51 (-57 ... -44)
ACCESS-CM2_r1i1p1f1 ()	2.6e+2 mm	36 (15 ... 1.4e+2)	-40 (-46 ... -33)
ACCESS-CM2_r2i1p1f1 ()	2.8e+2 mm	20 (11 ... 48)	-34 (-39 ... -29)

ACCESS-CM2_r3i1p1f1 ()	2.4e+2 mm	87 (36 ... 3.1e+2)	-44 (-49 ... -39)
CAMS-CSM1-0_r2i1p1f1 ()	1.2e+2 mm	6.2 (4.0 ... 11)	-37 (-42 ... -31)
CNRM-CM6-1-HR_r1i1p1f2 ()	1.4e+2 mm	8.3 (4.6 ... 18)	-31 (-36 ... -25)
EC-Earth3_r1i1p1f1 ()	1.5e+2 mm	13 (7.3 ... 31)	-40 (-45 ... -35)
EC-Earth3-Veg_r4i1p1f1 ()	1.3e+2 mm	19 (10 ... 49)	-49 (-54 ... -44)
EC-Earth3-Veg_r6i1p1f1 ()	1.5e+2 mm	20 (12 ... 39)	-47 (-51 ... -42)
EC-Earth3-Veg-LR_r1i1p1f1 ()	1.3e+2 mm	38 (18 ... 1.1e+2)	-57 (-63 ... -52)
HadGEM3-GC31-MM_r1i1p1f3 ()	1.3e+2 mm	12 (6.8 ... 24)	-37 (-42 ... -31)
HadGEM3-GC31-MM_r2i1p1f3 ()	1.2e+2 mm	13 (7.7 ... 24)	-41 (-46 ... -36)
HadGEM3-GC31-MM_r3i1p1f3 ()	1.2e+2 mm	21 (11 ... 50)	-42 (-47 ... -37)
HadGEM2-ES_ICTP-RegCM4-7_r1i1p1 ()	3.1e+2 mm	5.6 (2.8 ... 20)	-22 (-32 ... -13)
NorESM1-M_ICTP-RegCM4-7_r1i1p1 ()	1.7e+2 mm	88 (8.8 ... 1.5e+3)	-57 (-65 ... -51)
GFDL-ESM2M_RU-CORE-RegCM4-3_r1i1p1 ()	4.0e+2 mm	20 (11 ... 1.2e+2)	-42 (-51 ... -35)

Table A3.2.2: *Event magnitude, probability ratio and change in intensity for 1-in-20-year return period for pr-JASO for observational datasets and each model that passed the evaluation tests, from RONI ASO in 2026 vs neutral conditions in the present climate.*

A3.3 Temperature

Model / Observations	**Threshold for return period 20 yr**	**(c) Pre-industrial vs. present**		**(b) Present vs. 2.8°C above pre-industrial**	
		Probability ratio PR [-]	**Change in intensity ΔI [˚C]**	**Probability ratio PR [-]**	**Change in intensity ΔI [˚C]**
CPC	28.43 ˚C	1.3e+29 (2.7e+19..1.	1.99 (1,68.. 2.30		

		9e+65)			
ERA5-Land	27.75 ˚C	7.1e11 (1.9e9....4.01e+19)	1.41 (1.15..1.63)		
JRA	27.53 ˚C	2.3e+20 (1.5e+16…1.1e+30)	1.67 (1.51…1.82		
MSWX	28.67 ˚C	5.0e+19 (1.4e13, 2.5e+36)	1.65 (1.33,1.97)		
ACCESS-CM2_r1i1p1f1 ()	28 ˚C	4.0e+10 (5.7e+8 ... 1.9e+13)	1.4 (1.3 ... 1.5)	20 (20 ... 20)	1.4 (1.3 ... 1.5)
BCC-CSM2-MR_r1i1p1f1 ()	28 ˚C	2.8e+14 (7.7e+11 ... 2.0e+18)	1.5 (1.4 ... 1.7)	20 (20 ... 20)	1.4 (1.4 ... 1.5)
CAMS-CSM1-0_r2i1p1f1 ()	27 ˚C	3.4e+10 (1.8e+8 ... 6.8e+13)	1.4 (1.2 ... 1.6)	20 (20 ... 20)	1.3 (1.2 ... 1.5)
CESM2_r10i1p1f1 ()	28 ˚C	2.4e+29 (7.7e+24 ... 1.8e+36)	1.7 (1.6 ... 1.8)	20 (20 ... 20)	1.5 (1.4 ... 1.6)
CESM2-WACCM_r1i1p1f1 ()	29 ˚C	1.8e+34 (1.7e+28 ... 5.7e+43)	1.7 (1.6 ... 1.7)	20 (20 ... 20)	1.5 (1.4 ... 1.6)
CMCC-ESM2_r1i1p1f1 ()	28 ˚C	4.6e+8 (6.3e+6 ... 1.8e+11)	1.1 (0.98 ... 1.3)	20 (20 ... 20)	1.2 (1.2 ... 1.3)
CNRM-CM6-1_r1i1p1f2 ()	26 ˚C	2.8e+5 (1.5e+4 ... 2.1e+7)	1.1 (0.89 ... 1.2)	20 (20 ... 20)	1.3 (1.2 ... 1.4)
CNRM-CM6-1-HR_r1i1p1f2 ()	26 ˚C	4.4e+13 (4.0e+11 ... 3.3e+16)	1.3 (1.2 ... 1.3)	20 (20 ... 20)	1.4 (1.3 ... 1.4)
EC-Earth3-Veg_r1i1p1f1 ()	29 ˚C	6.5e+3 (9.6e+2 ... 9.0e+4)	1.4 (1.2 ... 1.6)	16 (15 ... 18)	1.4 (1.2 ... 1.5)
GFDL-ESM4_r1i1p1f1 ()	27 ˚C	1.2e+22 (3.4e+17 ... 1.2e+29)	2.2 (2.0 ... 2.4)	20 (20 ... 20)	1.9 (1.7 ... 2.0)
HadGEM3-GC31-LL_r1i1p1f3 ()	28 ˚C	1.4e+11 (7.3e+8 ... 2.9e+14)	1.4 (1.3 ... 1.5)	20 (20 ... 20)	1.4 (1.4 ... 1.5)
HadGEM3-GC31-MM_r1i1p1f3 ()	28 ˚C	1.5e+9 (5.8e+6 ... 4.0e+12)	1.5 (1.3 ... 1.6)	20 (20 ... 20)	1.5 (1.4 ... 1.5)

IITM-ESM_r1i1p1f1 ()	28 ˚C	3.4e+9 (1.8e+7 ... 1.3e+13)	1.3 (1.1 ... 1.5)	20 (20 ... 20)	1.5 (1.3 ... 1.6)
INM-CM5-0_r1i1p1f1 ()	27 ˚C	1.4e+20 (3.7e+16 ... 1.1e+26)	1.2 (1.1 ... 1.3)	20 (20 ... 20)	1.1 (1.1 ... 1.2)
MPI-ESM1-2-LR_r10i1p1f1 ()	26 ˚C	1.3e+8 (3.9e+6 ... 2.5e+10)	1.1 (1.0 ... 1.3)	20 (20 ... 20)	1.2 (1.1 ... 1.3)
MRI-ESM2-0_r1i1p1f1 ()	28 ˚C	8.3e+21 (1.8e+18 ... 2.2e+28)	1.7 (1.5 ... 1.8)	20 (20 ... 20)	1.5 (1.5 ... 1.6)
NorESM2-MM_r1i1p1f1 ()	28 ˚C	1.4e+21 (4.6e+17 ... 1.4e+27)	1.8 (1.7 ... 2.0)	20 (20 ... 20)	1.7 (1.6 ... 1.8)
CNRM-CM5_SMHI-RCA4_r1i1p1 ()	27 ˚C	1.6e+5 (3.0e+3 ... 3.9e+8)	1.4 (1.0 ... 1.7)	19 (18 ... 20)	1.3 (1.2 ... 1.5)
HadGEM2-ES_GERICS-REMO2015_r1i1p1 ()	30 ˚C	1.3e+3 (1.1e+2 ... 9.9e+4)	1.3 (0.90 ... 1.6)	16 (13 ... 19)	1.3 (1.1 ... 1.6)
HadGEM2-ES_ICTP-RegCM4-7_r1i1p1 ()	27 ˚C	7.9e+8 (2.7e+6 ... 9.8e+13)	1.2 (0.99 ... 1.4)	20 (20 ... 20)	1.2 (1.1 ... 1.3)
HadGEM2-ES_SMHI-RCA4_r1i1p1 ()	28 ˚C	2.9e+7 (4.3e+5 ... 5.1e+10)	1.2 (1.0 ... 1.4)	20 (20 ... 20)	1.2 (1.1 ... 1.3)
MPI-ESM-LR_GERICS-REMO2015_r1i1p1 ()	29 ˚C	2.2e+9 (2.5e+6 ... 5989120522706578)	2.0 (1.6 ... 2.3)	20 (19 ... 20)	1.7 (1.4 ... 1.9)
MPI-ESM-MR_RU-CORE-RegCM4-3_r1i1p1 ()	27 ˚C	1.9e+24 (5.5e+18 ... 7.1e+35)	1.4 (1.2 ... 1.6)	20 (20 ... 20)	1.4 (1.3 ... 1.5)

Table A3.3.1: *Event magnitude, probability ratio and change in intensity for 1-in-20-year return period for mean Aug-Oct temperature for observational datasets and each model that passed the evaluation tests. (a) from pre-industrial climate to the present and (b) from the present to 2.8℃ above pre-industrial climate.*

Model / Observations	**Threshold for return period 20 yr**	**Probability ratio PR [-]**	**Change in intensity ΔI [˚C]**
CPC	28.43 ˚C	2.59 (0.90, 2.81)	0.12 (-0.01, 0.25)

ERA5-Land	27.75 ˚C	96661.44 (6107.76,32605801.09)	0.74 (0.59,0.88)
JRA	27.53 ˚C	59.11 (15.97,588.30)	0.41 (0.32,0.51)
MSWX	28.67 ˚C	122.11 (28.34,3637.17)	0.41 (0.29,0.54)
ACCESS-CM2_r1i1p1f1 ()	28 ˚C	0.18 (0.11 ... 0.29)	-0.28 (-0.37 ... -0.18)
BCC-CSM2-MR_r1i1p1f1 ()	28 ˚C	0.81 (0.44 ... 1.6)	-0.024 (-0.098 ... 0.054)
CAMS-CSM1-0_r2i1p1f1 ()	27 ˚C	7.7 (3.7 ... 20)	0.23 (0.15 ... 0.31)
CESM2_r10i1p1f1 ()	28 ˚C	0.28 (0.16 ... 0.55)	-0.12 (-0.20 ... -0.050)
CESM2-WACCM_r1i1p1f1 ()	29 ˚C	0.45 (0.24 ... 0.91)	-0.065 (-0.12 ... -0.0077)
CMCC-ESM2_r1i1p1f1 ()	28 ˚C	60 (10 ... 6.3e+2)	0.36 (0.23 ... 0.48)
CNRM-CM6-1_r1i1p1f2 ()	26 ˚C	11 (4.1 ... 42)	0.30 (0.18 ... 0.42)
CNRM-CM6-1-HR_r1i1p1f2 ()	26 ˚C	4.4 (1.9 ... 12)	0.13 (0.057 ... 0.19)
EC-Earth3-Veg_r1i1p1f1 ()	29 ˚C	7.0e+2 (1.4e+2 ... 7.8e+3)	1.1 (0.93 ... 1.4)
GFDL-ESM4_r1i1p1f1 ()	27 ˚C	40 (16 ... 1.4e+2)	0.35 (0.27 ... 0.45)
HadGEM3-GC31-LL_r1i1p1f3 ()	28 ˚C	1.8 (0.74 ... 5.6)	0.069 (-0.039 ... 0.18)
HadGEM3-GC31-MM_r1i1p1f3 ()	28 ˚C	8.8 (4.1 ... 25)	0.27 (0.19 ... 0.36)
IITM-ESM_r1i1p1f1 ()	28 ˚C	24 (7.4 ... 1.1e+2)	0.32 (0.21 ... 0.44)
INM-CM5-0_r1i1p1f1 ()	27 ˚C	0.62 (0.31 ... 1.4)	-0.037 (-0.098 ... 0.021)
MPI-ESM1-2-LR_r10i1p1f1 ()	26 ˚C	1.3e+2 (38 ... 7.3e+2)	0.43 (0.34 ... 0.54)
MRI-ESM2-0_r1i1p1f1 ()	28 ˚C	0.80 (0.40 ... 1.9)	-0.022 (-0.093 ... 0.054)
NorESM2-MM_r1i1p1f1 ()	28 ˚C	3.2 (1.2 ... 10)	0.11 (0.020 ... 0.21)

CNRM-CM5_SMHI-RCA4_r1i1p1 ()	27 ˚C	6.6 (1.5 ... 54)	0.32 (0.077 ... 0.54)
HadGEM2-ES_GERICS-REMO2015_r1i1p1 ()	30 ˚C	14 (2.5 ... 1.6e+2)	0.57 (0.22 ... 0.89)
HadGEM2-ES_ICTP-RegCM4-7_r1i1p1 ()	27 ˚C	19 (4.4 ... 2.5e+2)	0.28 (0.15 ... 0.43)
HadGEM2-ES_SMHI-RCA4_r1i1p1 ()	28 ˚C	3.9 (1.0 ... 31)	0.17 (0.0040 ... 0.33)
MPI-ESM-LR_GERICS-REMO2015_r1i1p1 ()	29 ˚C	2.5e+2 (21 ... 4.2e+4)	0.75 (0.45 ... 1.1)
MPI-ESM-MR_RU-CORE-RegCM4-3_r1i1p1 ()	27 ˚C	1.4 (0.33 ... 6.2)	0.023 (-0.087 ... 0.12)

Table A3.3.2: *Event magnitude, probability ratio and change in intensity for 1-in-20-year return period for mean Aug-Oct temperature for observational datasets and each model that passed the evaluation tests, from RONI ASO in 2026 vs neutral conditions in the present climate.*

A4 Supplementary figures

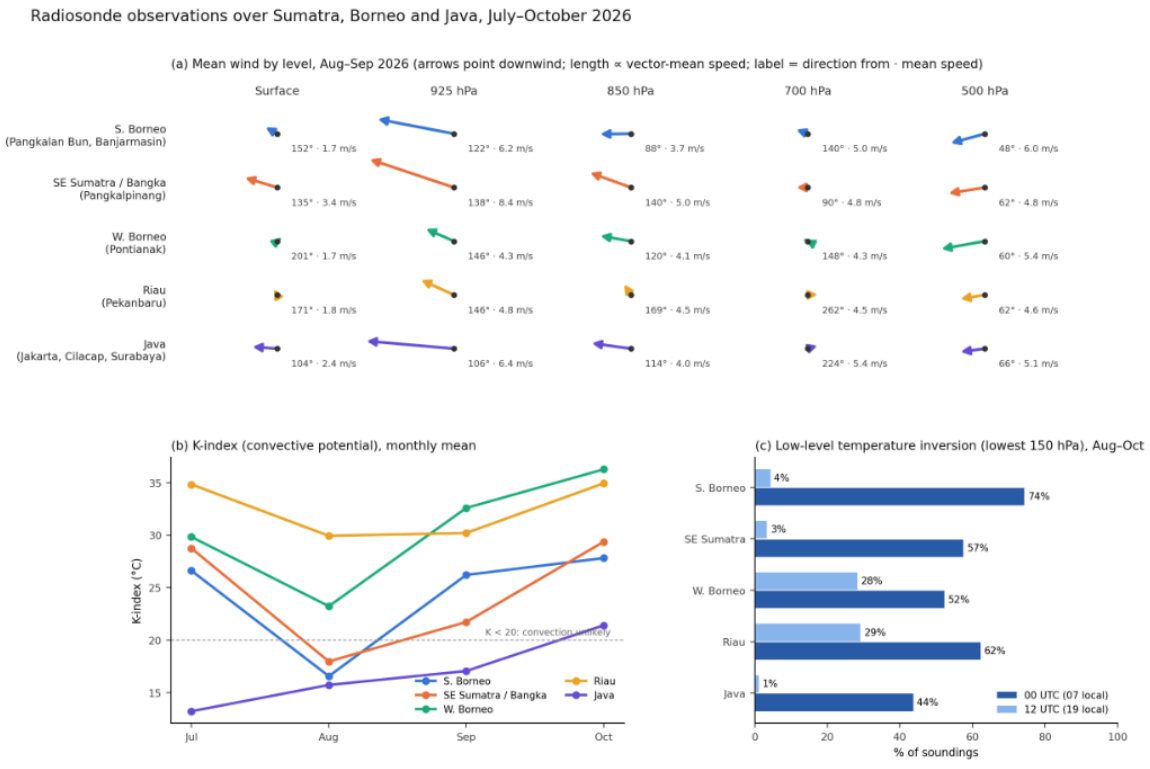


Figure A4.1: Supporting radiosonde summary for meteorological analysis: winds by level, K-index and inversion frequency information over the study region

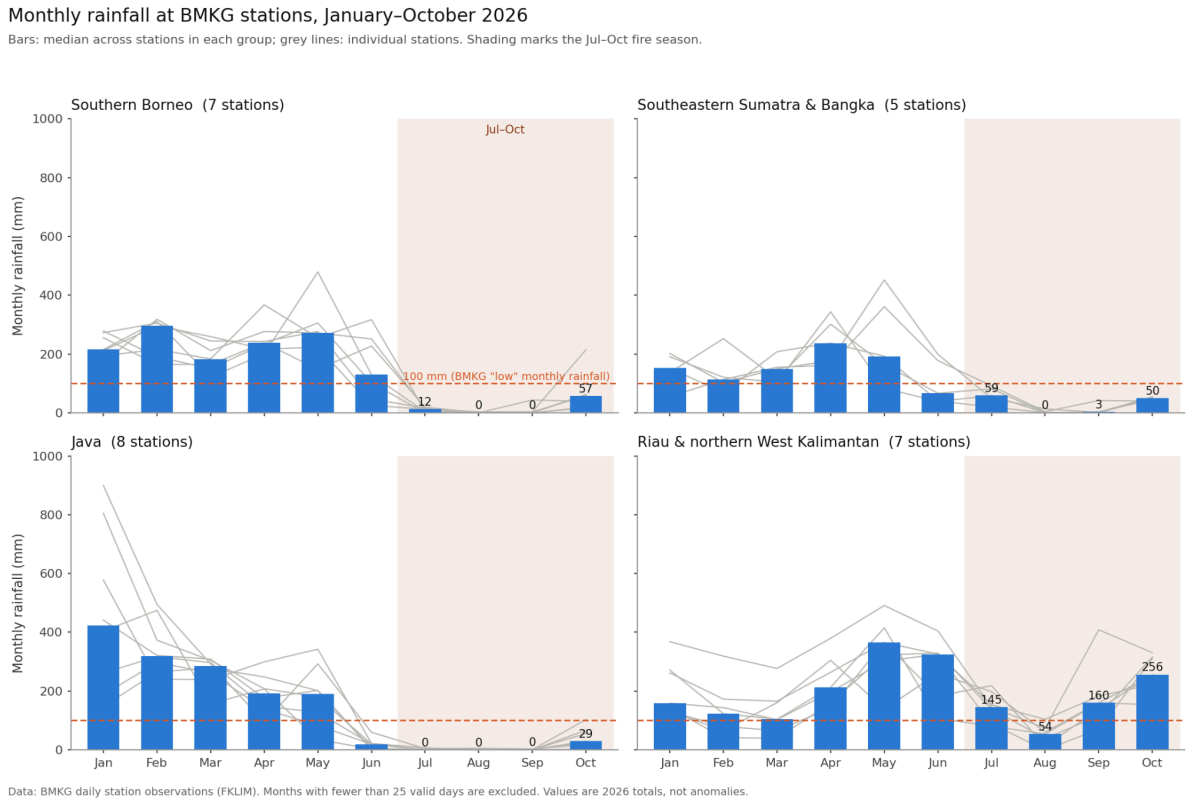


Figure A4.2: Monthly rainfall data at weather stations aggregated across BMKG regions of western Indonesia.

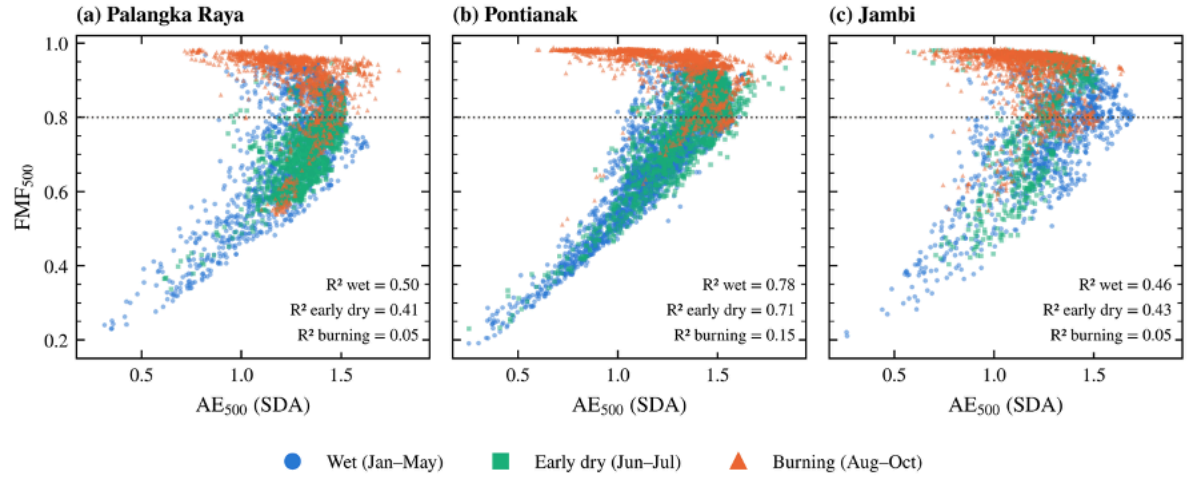


Figure A4.3. Relationship between the fine-mode fraction (FMF_{500}) and the Ångström exponent at 500 nm from the Spectral Deconvolution Algorithm during the wet, early dry and burning periods at (a) Palangka Raya, (b) Pontianak and (c) Jambi, 2026. Each point is an individual retrieval. The coefficient of determination (R^2) for each period is shown, and the dotted line marks FMF = 0.8.

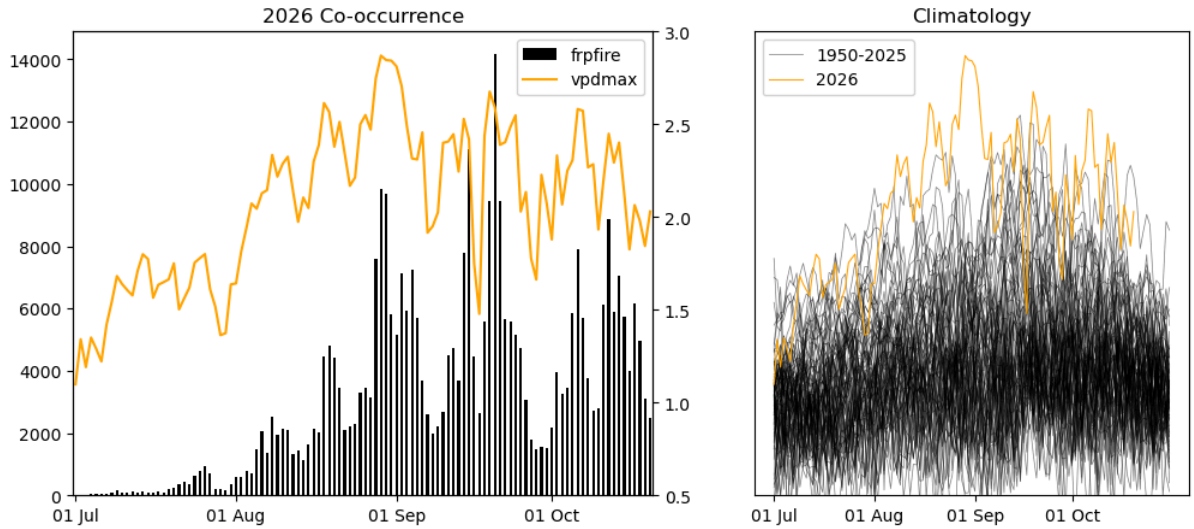


Figure A4.4: Borneo region – plot illustrating the co-occurrence of relative peaks in VPD (ERA5-Land) with peaks in fire radiative power (black) (GFAS1.4). The right panel shows how extreme daily VPD values were this year compared to historic values.

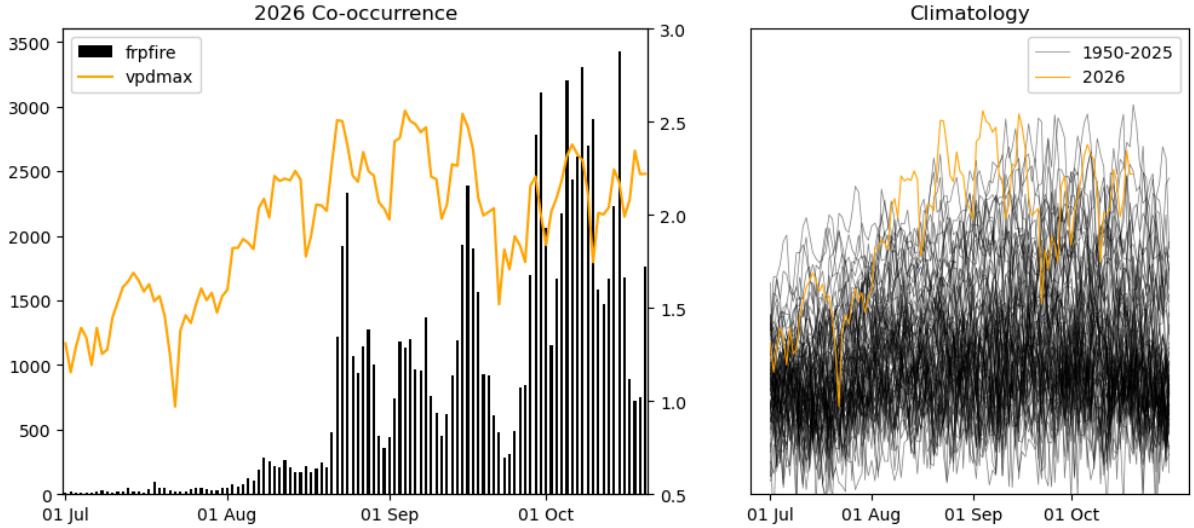


Figure A4.5: Sumatra region – plot illustrating the co-occurrence of relative peaks in VPD (ERA5-Land) with peaks in fire radiative power (black) (GFAS1.4). The right panel shows how extreme daily VPD values were this year compared to historic values.

A5 Model evaluation figures

A5.1 VPD

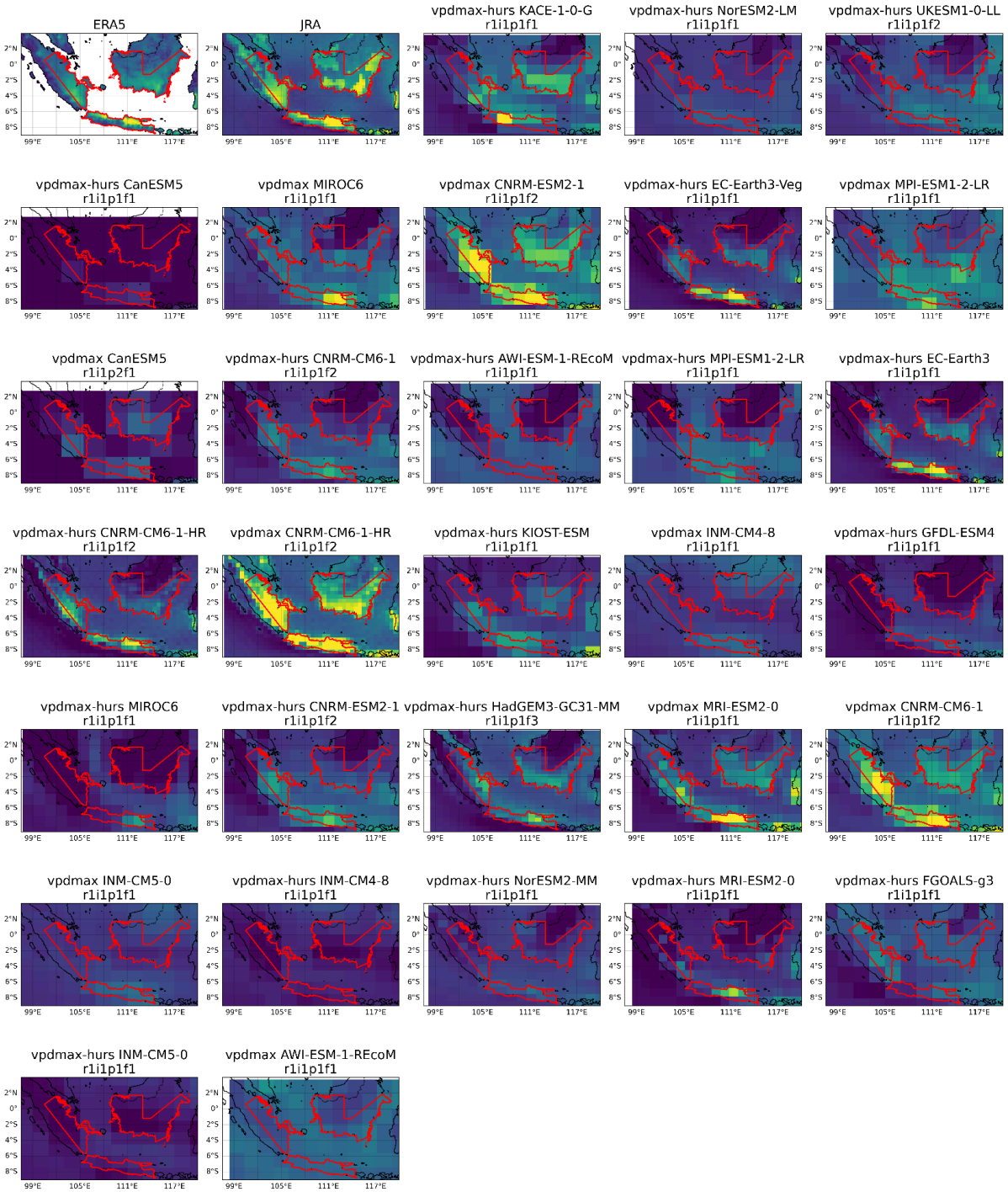


Figure A5.1.1: *Climatological (1991-2020) spatial patterns of VPD in August-October in observations and CMIP6 models. The study region is highlighted in red. Note: models use VPD calculated from either hurs or hursmin as denoted in the panel title.*

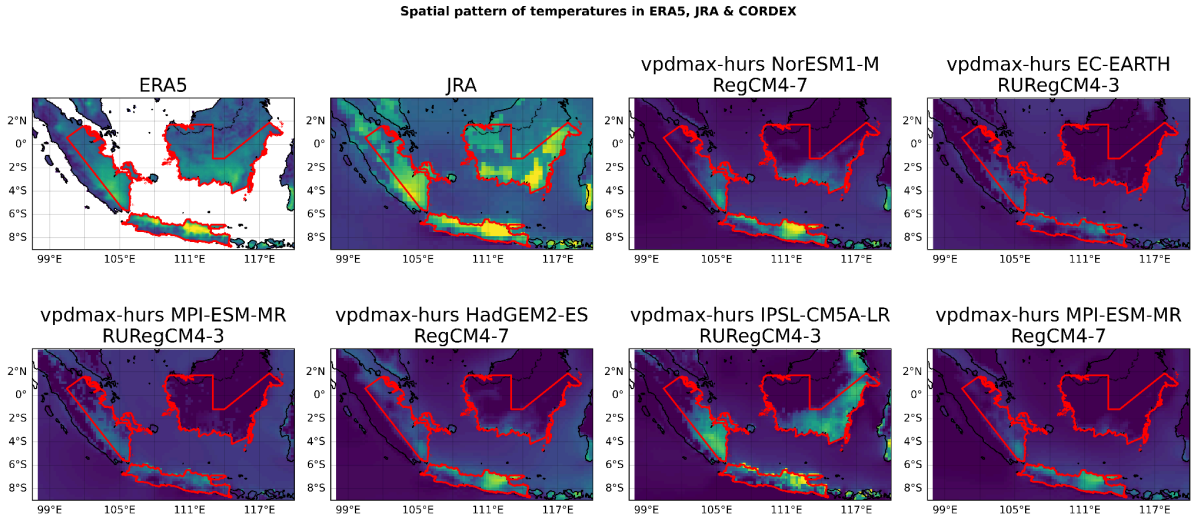


Figure A5.1.2: *Climatological (1991-2020) spatial patterns of VPD in August-October in observations and CORDEX models. The study region is highlighted in red. Note: models use VPD calculated from hurs as denoted in the panel title.*

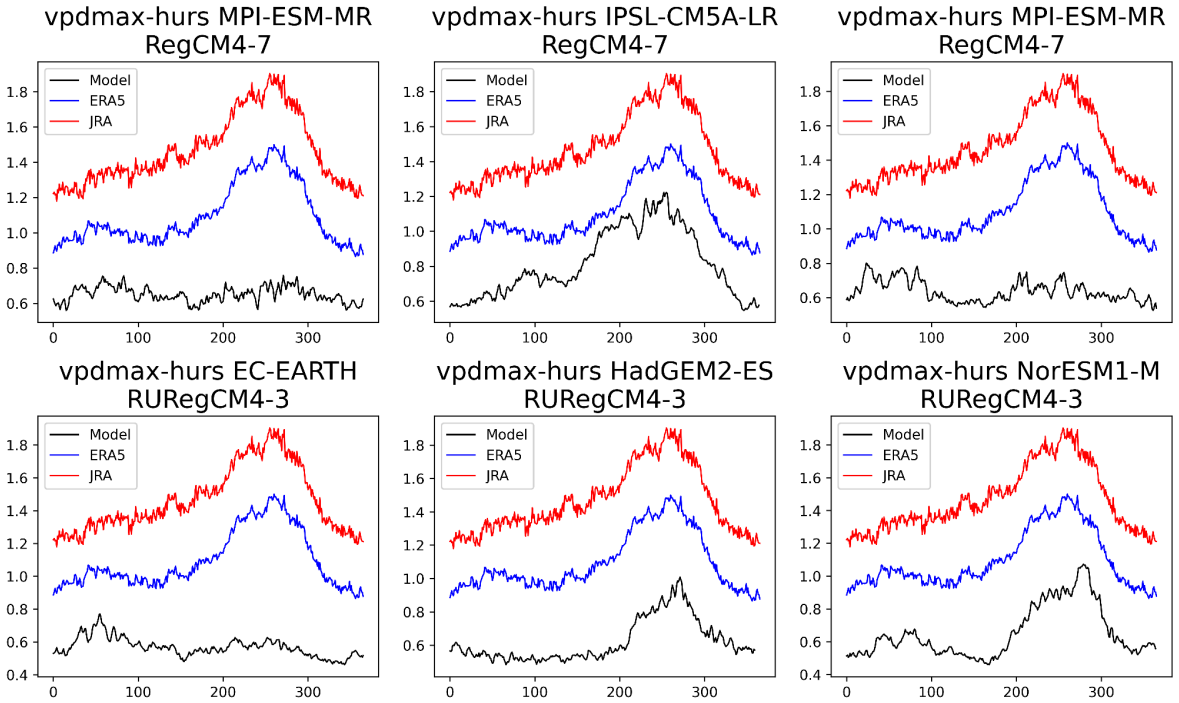


Figure A5.1.3: *Climatological (1991-2020) seasonal cycles of VPD in August-October in observations and CORDEX models. Note: models use VPD calculated from either hurs or hursmin as denoted in the panel title.*

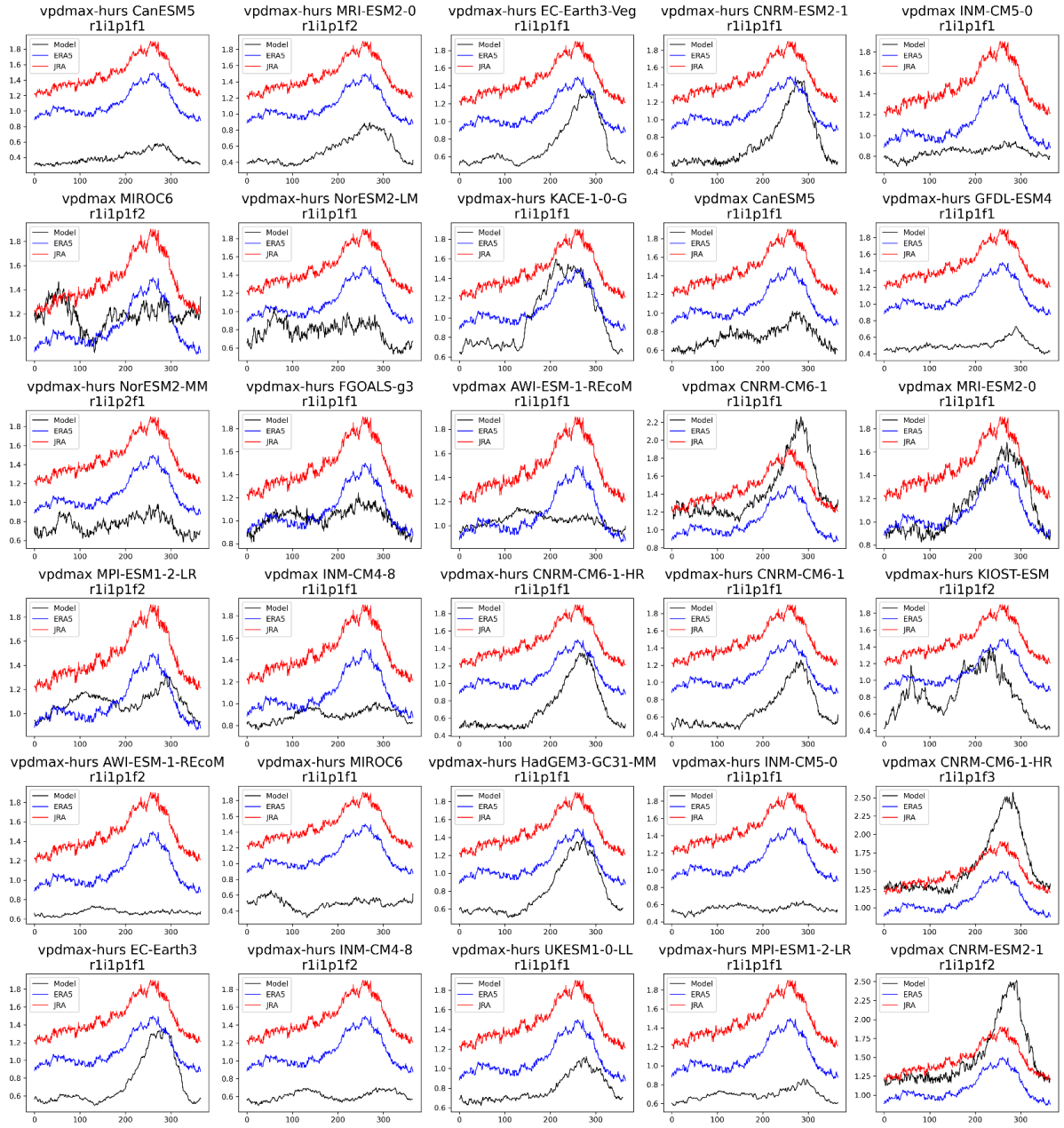


Figure A5.1.4: *Climatological (1991-2020) seasonal cycles of VPD in August-October in observations and CMIP6 models. Note: models use VPD calculated from either hurs or hursmin as denoted in the panel title.*

A5.2 Precipitation

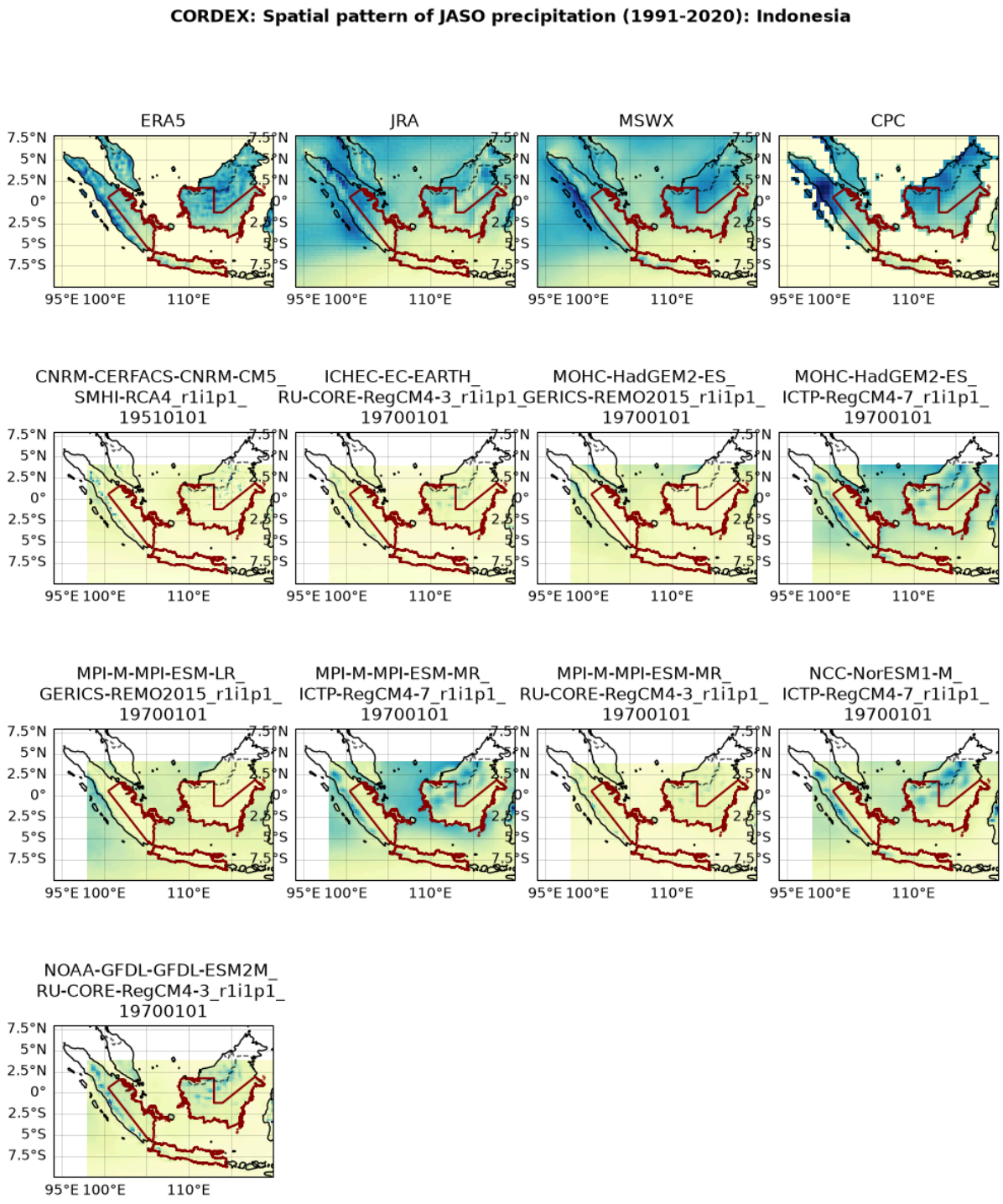


Figure A5.2.1: *Climatological (1991-2020) spatial patterns of precipitation during July to October in observations and CORDEX models. The study region is highlighted in red.*

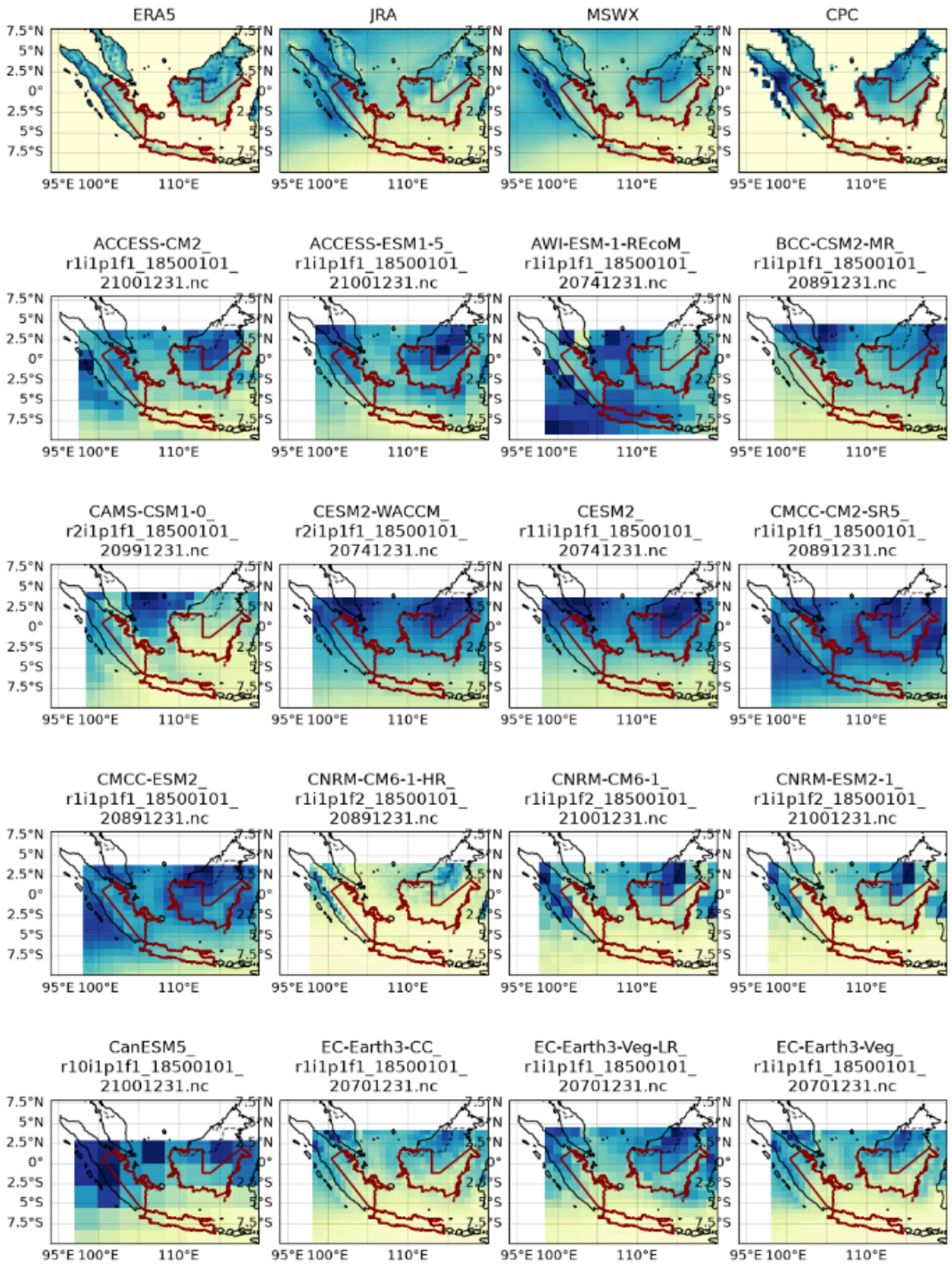


Figure A5.2.2: *Climatological (1991-2020) spatial patterns of precipitation during July to October in observations and CMIP6 models. The study region is highlighted in red (contd to next page).*

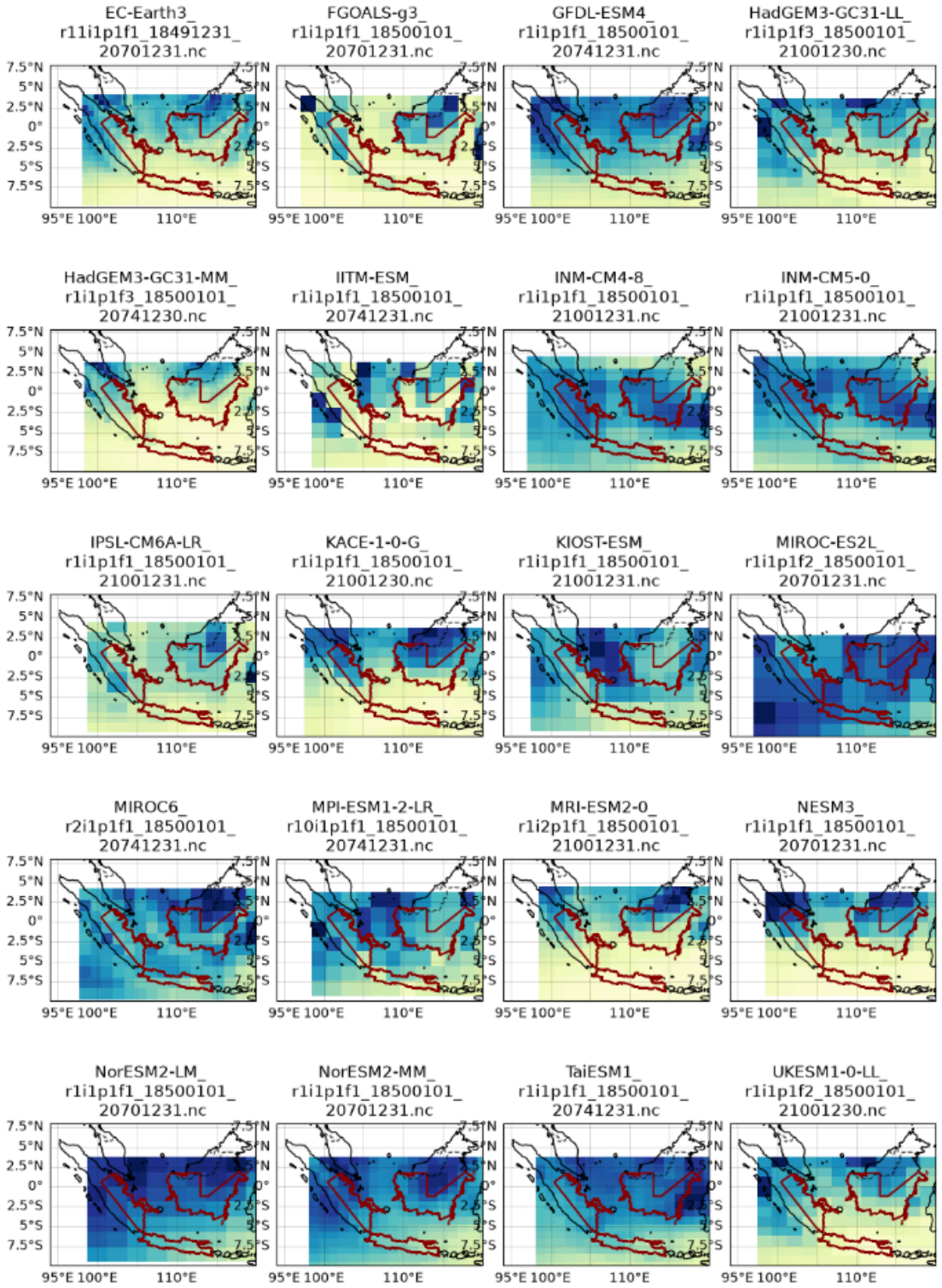


Figure A5.2.2: *(contd from last page) Climatological (1991-2020) spatial patterns of precipitation during July to October in observations and CMIP6 models. The study region is highlighted in red.*

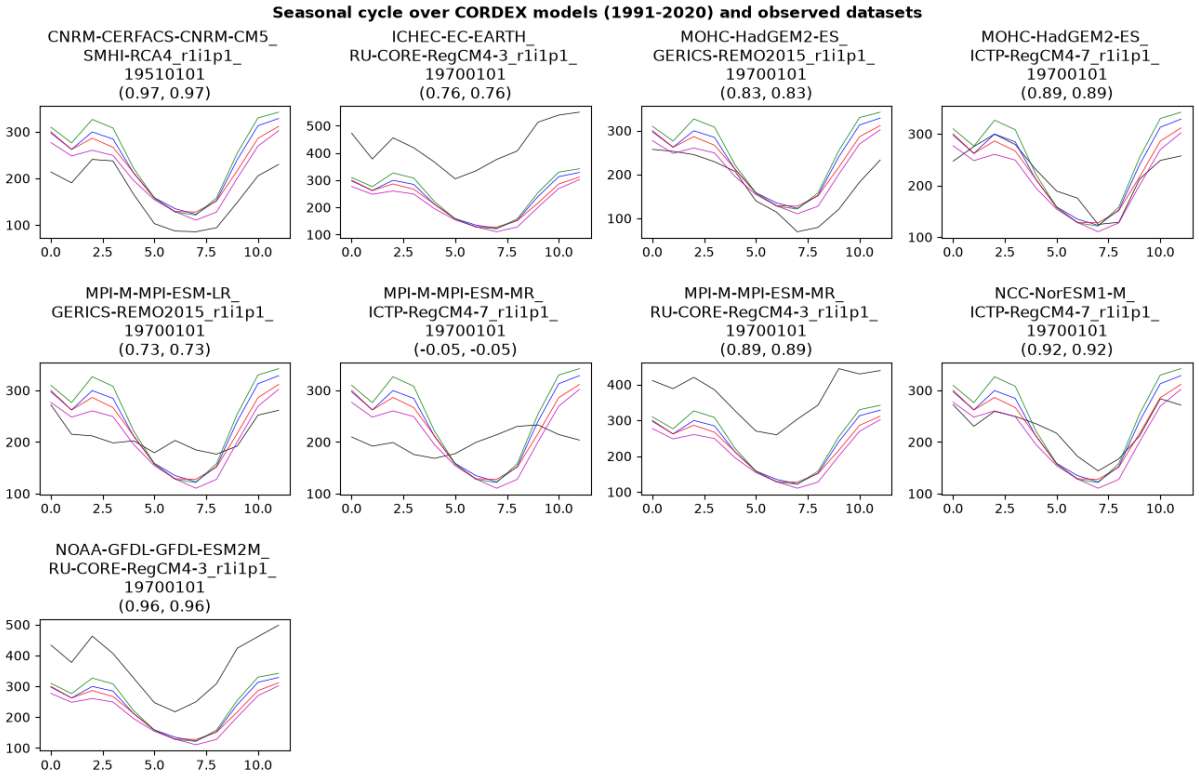


Figure A5.2.3: *Climatological (1991-2020) seasonal cycles of precipitation in observations and CORDEX models.*

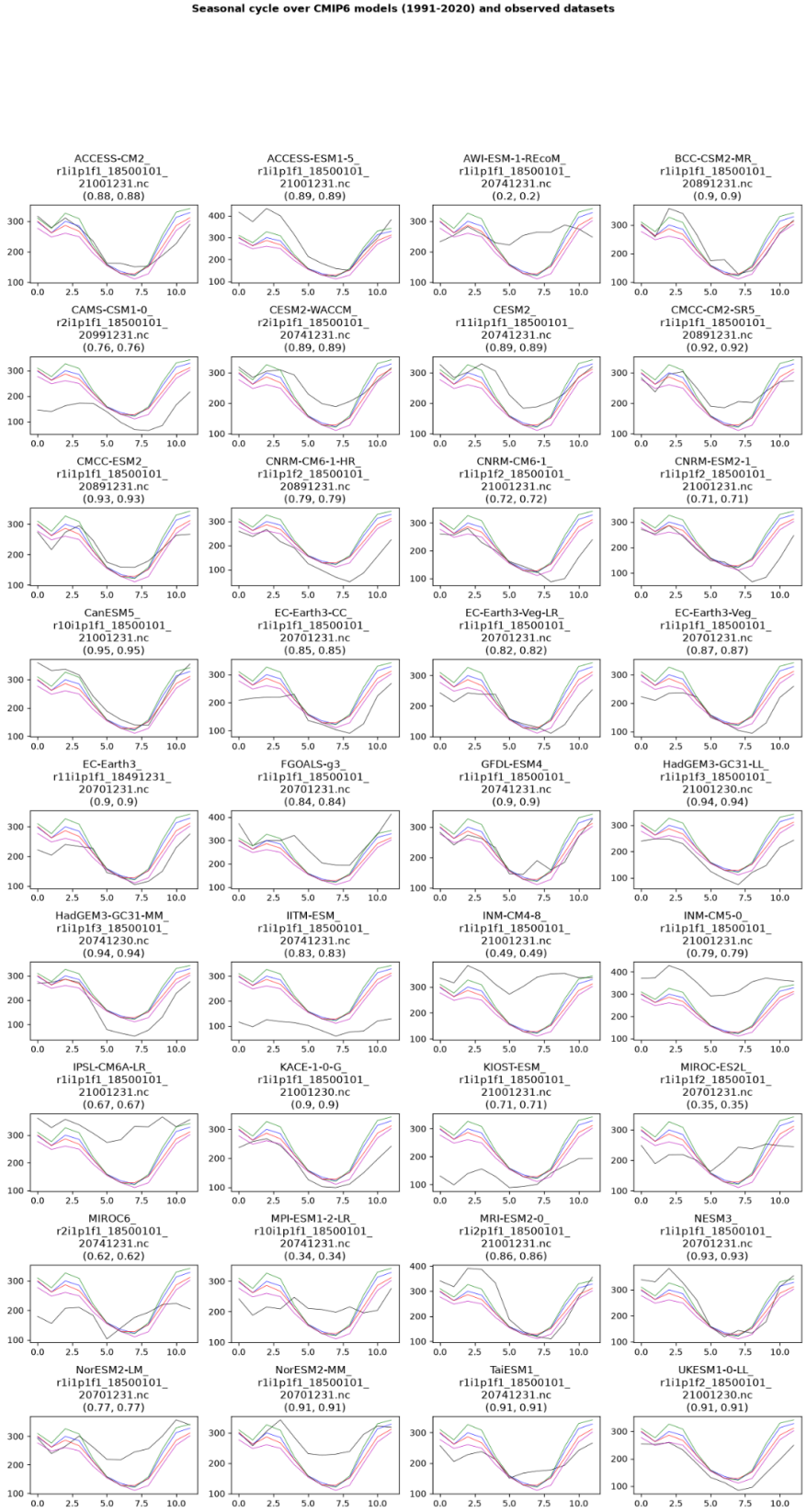


Figure A5.2.4: *Climatological (1991-2020) seasonal cycles of precipitation in observations and CMIP6 models.*

A5.3 Temperature

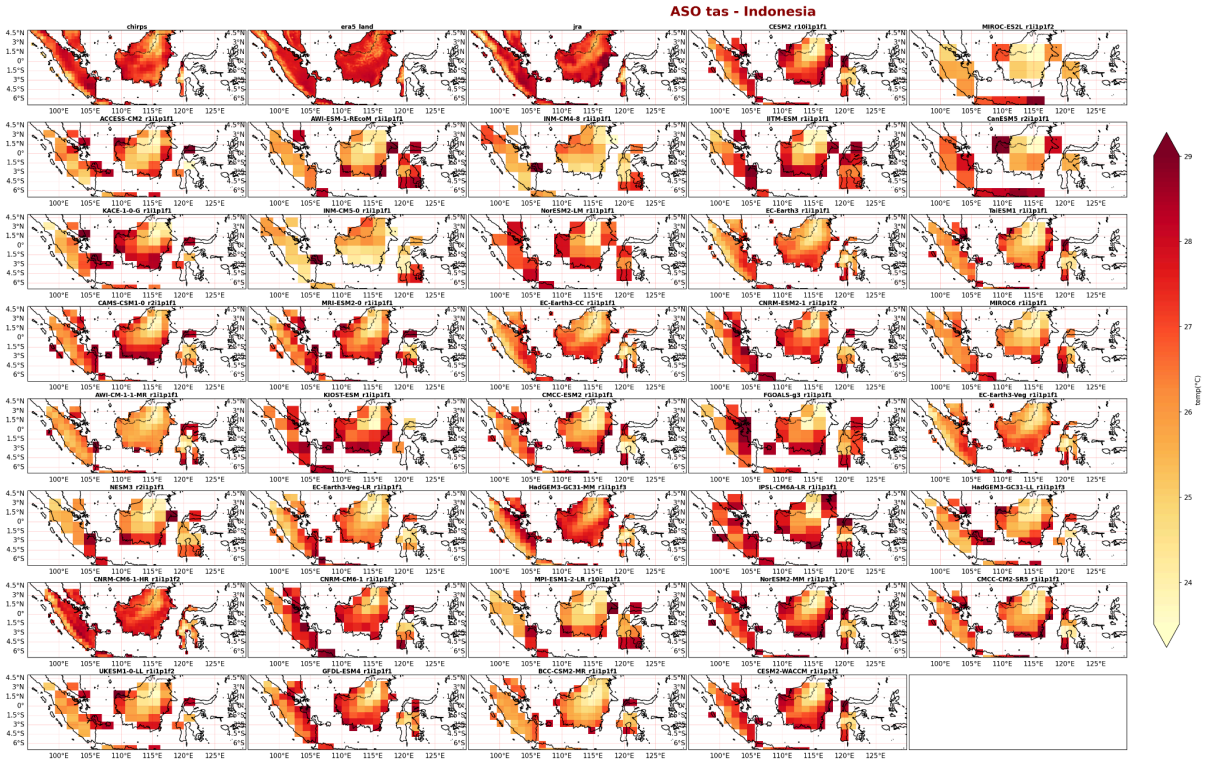


Figure A5.3.1: *Climatological (1991-2020) spatial patterns of August to October mean temperature in observations and CMIP6 models over the western Indonesia region*

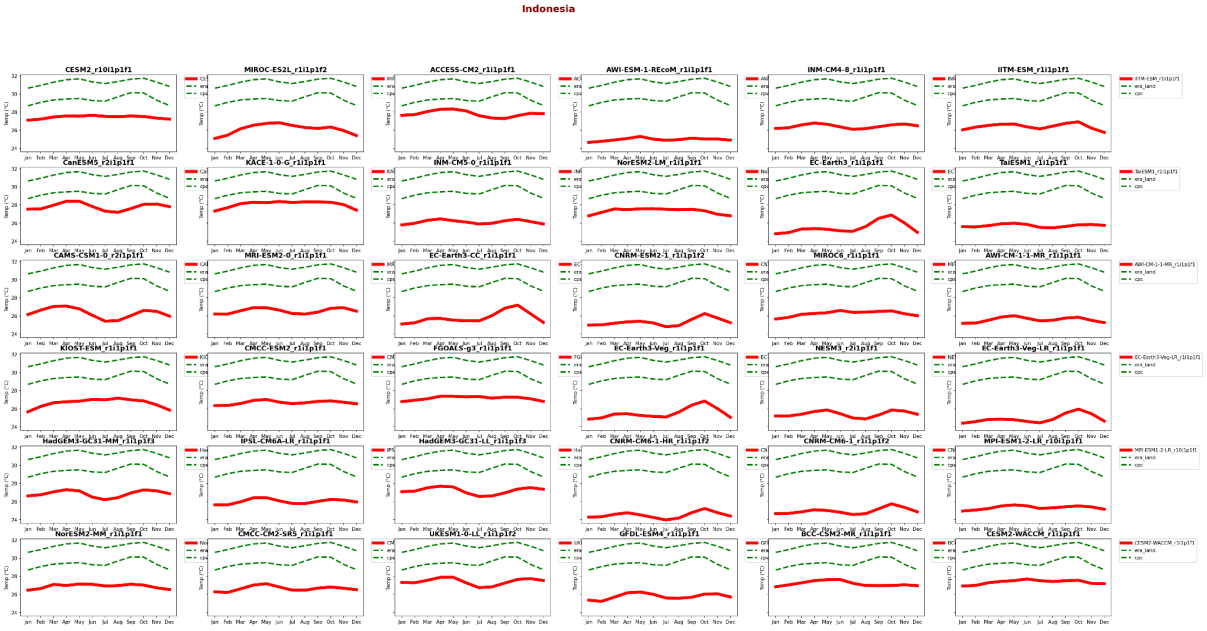


Figure A5.3.2: *Climatological (1991-2020) seasonal cycle patterns of August to October mean temperature in observations and CMIP6 models over the western Indonesia region*

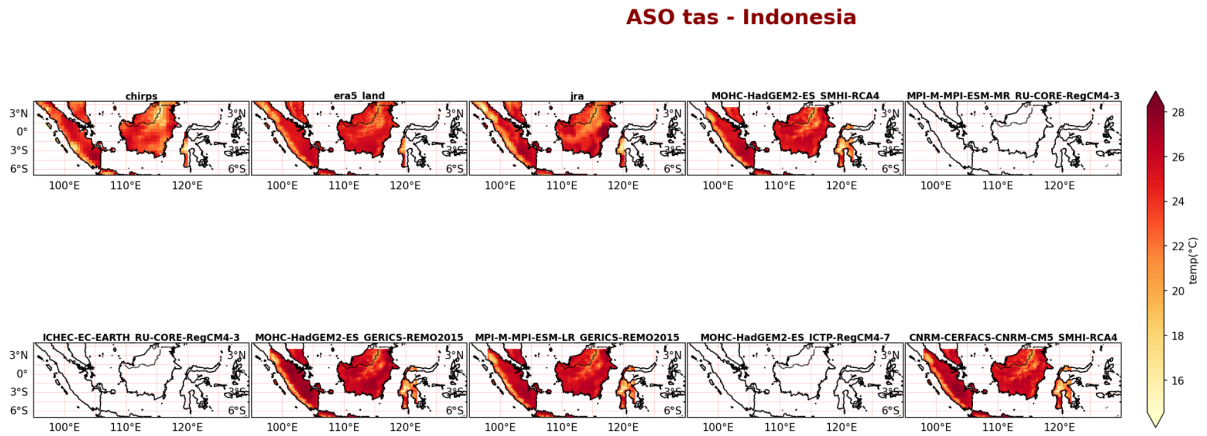


Figure A5.3.3: *Climatological (1991-2020) spatial patterns of August to October mean temperature in observations and CORDEX models over the western Indonesia region*

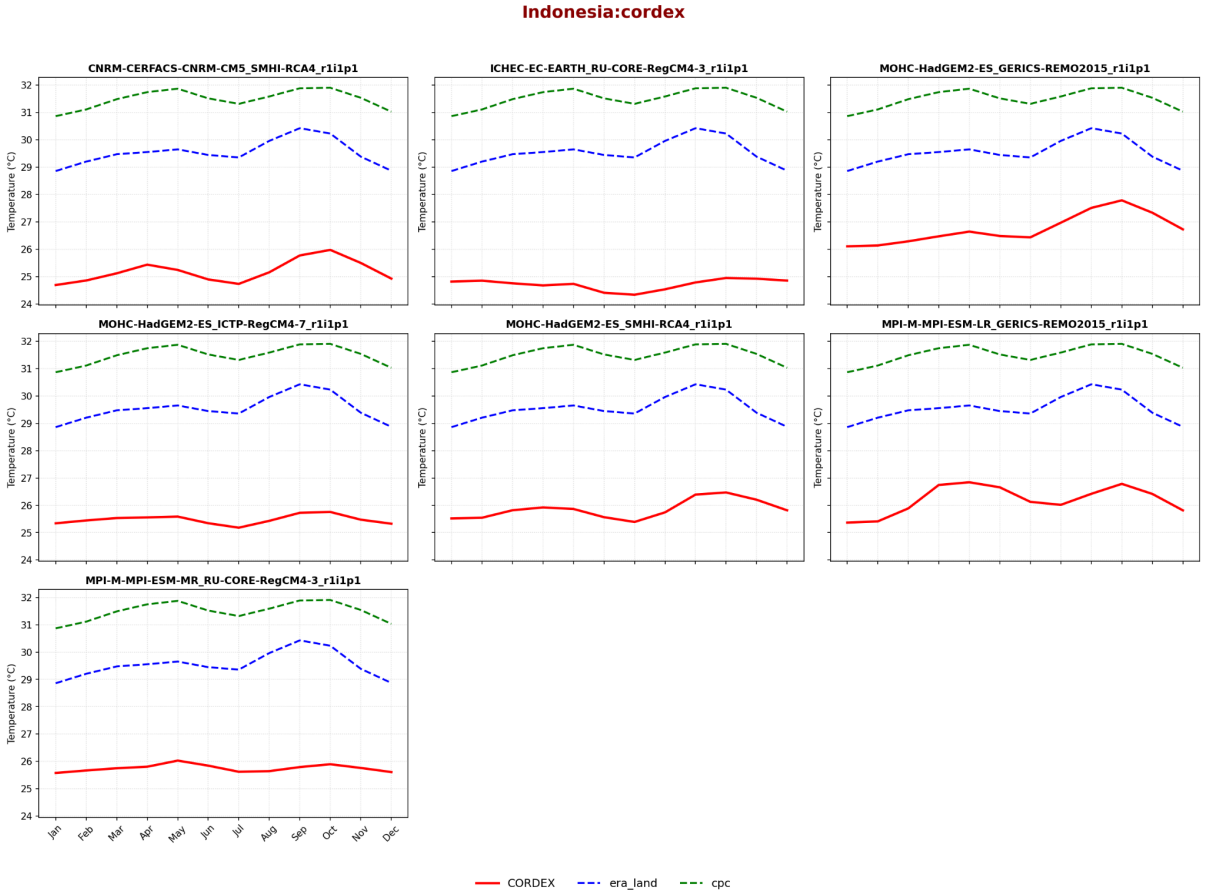


Figure A5.3.4: *Climatological (1991-2020) seasonal cycle patterns of August to October mean temperature in observations and CORDEX models over the western Indonesia region*